ISSN 2720-3581

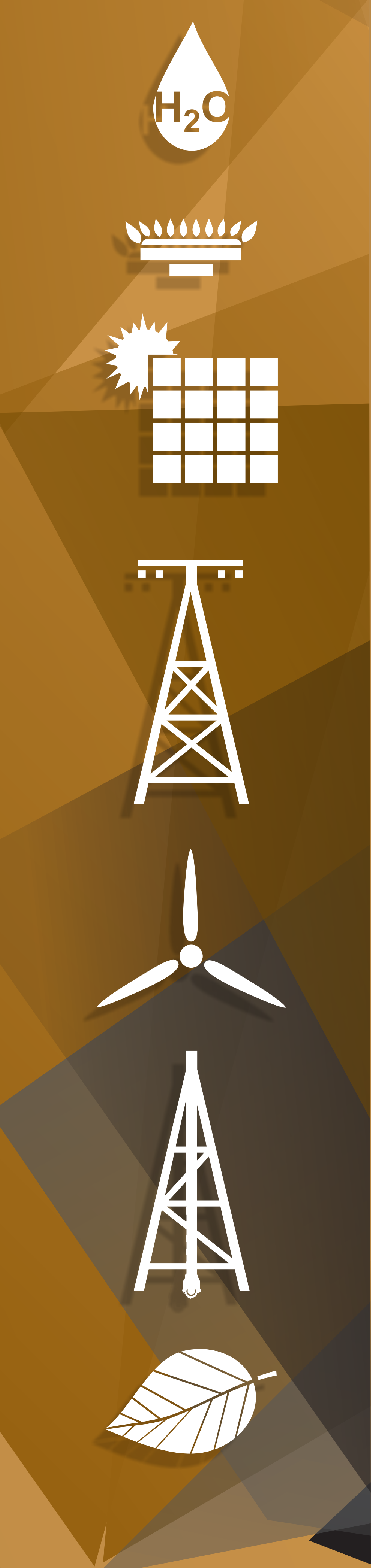

JOURNAL
OF GEOTECHNOLOGY AND ENERGY

FORMERLY AGH DRILLING, OIL, GAS

2024, vol. 41, no. 4

WYDAWNICTWA AGH

KRAKOW 2024

ISSN 2720-3581

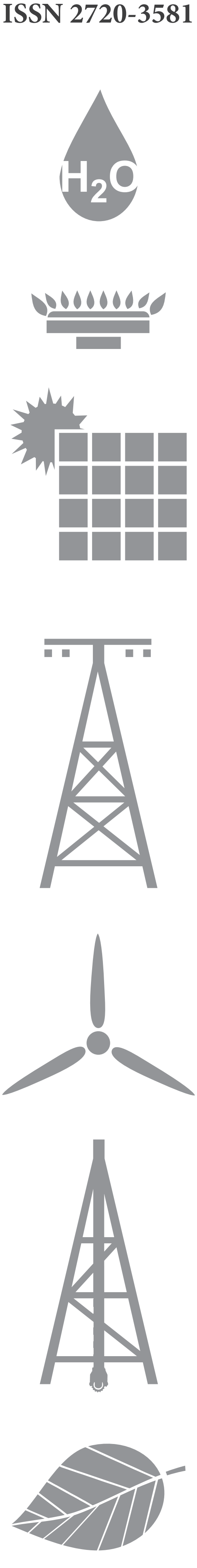

JOURNAL OF GEOTECHNOLOGY AND ENERGY

FORMERLY AGH DRILLING, OIL, GAS

2024, vol. 41, no. 4

WYDAWNICTWA AGH

KRAKOW 2024

The “Journal of Geotechnology and Energy” (formerly “AGH Drilling, Oil, Gas”) is a quarterly published by the Faculty of Drilling, Oil and Gas at the AGH University of Krakow, Poland. Journal is an interdisciplinary, international, peer-reviewed, and open access. The articles published in JGE have been given a favorable opinion by the reviewers designated by the editorial board.

Editorial Team

Editor-in-chief

Co-editors

Editorial Board

Publisher

AGH University Press

Linguistic corrector: *Aeddan Shaw*
Technical editor: *Kamila Zimnicka*
Desktop publishing: *Munda*
Cover design: *Paweł Sepielak*

ISSN: 2720-3581
DOI: https://doi.org/10.7494/jge

Journal website: https://journals.agh.edu.pl/jge

Wydawnictwa AGH (AGH University Press)
al. A. Mickiewicza 30, 30-059 Kraków
tel. 12 617 32 28, 12 636 40 38
e-mail: redakcja@wydawnictwoagh.pl
www.wydawnictwo.agh.edu.pl

CONTENTS

Journal of Geotechnology and Energy | vol. 41 | no. 4 | 2024 | pp. 5–9

https://doi.org/10.7494/jge.2024.41.4.6755

ARTICLE

ACTIVATION OF A DEWATERING WELL WITH THE SKINAUT CLAY MINERAL DISINTEGRATION AGENT

Jan Macuda

AGH University of Krakow, Faculty of Drilling, Oil and Gas, Poland
ORCID: 0000-0002-8180-8014
e-mail: macuda@agh.edu.pl

Date of submission:
22.11.2024

Date of acceptance:
23.11.2024

Date of publication:
30.12.2024

https://journals.agh.edu.pl/jge

Abstract: The drilling of hydrogeological boreholes by rotary methods and with the use of drilling mud impairs the permeability of water-bearing rocks in the near-hole zone. This is mainly caused by the penetration of solids and mud filtrate into the pores or fractures of the drilled rocks. Consequently, the depression increases, and the hydraulic efficiency of the borehole drops, leading to the reduction of well productivity.

As a means of improving the damaged permeability of rocks in the near-hole zone, a clay mineral disintegration agent called SKINAUT was developed and patented. To evaluate its effectiveness in industrial conditions, a test was carried out to activate a dewatering borehole for intaking water from loose formations at the Szczerców open cast. The applied chemical helped to decolmatate the pore medium and lower the hydraulic resistance of the borehole, resulting in a reduction in depression and a significant improvement of its hydraulic efficiency.

Keywords: rock permeability, colmatation, disintegration of clayey minerals, dewatering borehole, borehole activation, hydraulic efficiency of borehole, groundwater exploitation, life of hydrogeological borehole

1. Introduction

When aquifers are drilled with a rotary drilling mud method, rocks in the near-hole zone undergo colmatation. This leads to physical changes in the porous medium due to the deposition of solid phase particles and penetration of the drilling mud filtrate. Then the filtration rate of water in the colmatated parts of the aquifer is lowered, resulting in a growing depression and a drop in the hydraulic efficiency of the borehole. Consequently, the total capacity of the borehole is reduced [1].

The drilling mud circulating in the borehole is also responsible for the formation of clayey deposits on the borehole wall, which also increases the hydraulic resistance to water entering the borehole [1, 2]. When drilling hydrogeological boreholes, the colmatation of rocks in the near-hole zone is also accompanied by clogging of the active surface of the filter when it is installed in a borehole [1, 3].

Currently, the industry practice does not offer any effective way to significantly reduce the colmatation in the near-hole zone during borehole drilling with bentonite muds. One of the best ways to reduce the near-hole zone colmatation is to drill in aquifer formations at the "pressure limit" level. In all countries where strict acceptance criteria for intake and dewatering boreholes are the case, prior to putting the boreholes in operation, activation treatments are mandatory to minimize the degree of damage to rock permeability in the filter zone. Cleaning of the filter zone from filtrate and solids improves the hydraulic efficiency of the borehole, and before all, has a significant impact on increasing borehole productivity and extending its life [2–4]. To improve the damaged permeability of rocks in the near-hole zone, especially with clayey particles, an effective clay mineral disintegration agent called SKINAUT was developed and patented [4]. To evaluate its effectiveness under industrial conditions, a dewatering borehole, drilled with the rotary drilling mud method, was subjected to an activation treatment. The dewatering borehole subjected to the treatment was located within the Szczerców open cast of PGE KWB Bełchatów (a lignite mine).

2. Characteristics of geological and hydrogeological conditions of drilling works within the Szczerców open cast area

The Szczerców open cast rests in the western part of the "Bełchatów" lignite deposit, and is situated within the latitudinal Kleszczów trench, 40 km long and 1.5–2.0 km wide, formed in the Jurassic and Cretaceous strata. Three elements of different structure are distinguished in it – the western one with a length of 8 km within the "Szczerców" deposit, the middle one with a length of 12 km within the "Bełchatów" deposit, and the eastern one within the "Kamieńsk" deposit [5]. The "Szczerców" and "Bełchatów" deposits are separated by a salt diapir, while the "Kamieńsk" and "Bełchatów" deposits are separated by a fault zone – the Widawka fault. Such a tectonic structure causes that within the "Kamieńsk" deposit the depth of occurrence, formation and its thickness differ from the remaining two outcrops [6]. The oldest documented formations, i.e. the Lower Carboniferous Culmic facies, developed as claystone, siltstone, black clay shale and greywacke, and the Permian formations represented by the Rotliegendes and Zechstein sediments developed as salts and associated gypsum and anhydrite, are related to the existing salt diapir with an average thickness of 775 m and a width of about 550 m [5]. This structure pierces the Upper Jurassic and Cretaceous and the eroded Tertiary strata. The subcoal complex of the Lower Miocene is sandy and silty-silty, with layers of lignite coals. The thickness of these sediments varies from 10 m to 130 m, with a maximum of 270 m [5, 6]. The coal complex dated to the Middle Miocene is the most important part of the whole system. The bottom is formed by a layer of tuffites, 3–5 cm thick, above which is a thin seam of lignite with quartzite sands overburdened. Higher up is the main lignite seam with a thickness of 40–60 m, and the depth of the bedrock is 170–300 m [6]. The "Bełchatów" deposit, with resources of 1.2 billion t, contains lignite, defined as proper, detrital, and weakly layered. The seam thickness is 30–70 m, in places 100 m, and even 230.5 m [4]. Within the "Szczerców" deposit, 750 million t resources, and a seam thickness of 12–140 m, proper and proper-xylitic lignite occurs. The top part of the complex is formed by clay-carbonaceous and clay-sandy sediments of the supracoal series [6]. The Tertiary sediments are strongly reduced outside the trench area and their thickness does not exceed 50 m. The depth of freshwater ranges from 400–600 m b.s.

Three aquifers can be distinguished in the lignite area, i.e. Quaternary, Tertiary and Cretaceous-Jurassic [5]. The Quaternary horizon mainly consists of sands and gravels with a thickness of 20–40 m, locally decreasing to zero. In the Kleszczów trough, the thickness reaches 150 m. On the northern side, parallel to the axis of the ditch, there is an erosion trough, where sands and gravels overlie Mesozoic sediments reaching an average thickness of 155 m (locally 300 m). In natural conditions, the water of this complex was supplied by precipitation. The depth of occurrence of the first aquifer was 0–2 m b.s. in river valleys, and 5–10 m b.s. in morphologically elevated areas. This complex was characterized by a free water table. The Tertiary floor is built up by fine- and medium-grained sands above the lignite seam, within the seam and in the subcoal complex. The thickness of the latter is 0–200 m (average 35 m). The Cretaceous-Jurassic strata, composed of limestone, marl, sandstone and sand, are characterized by the occurrence of fractured and fissure-karst waters, which distinguishes them from the others. The Tertiary and Cretaceous-Jurassic horizons are characterized by a pressure head and, in places, free water table. They are located at similar depths as the Quaternary horizon and are supplied by infiltration and/or hydrogeological windows. As in the case of the Quaternary complex, the watershed areas of the Widawka River basin were the recharge zones for both of these horizons.

3. Design and technology of performing a dewatering borehole

The dewatering borehole, which was subjected to the activation treatment with the new SKINOUT clay particle disintegration agent, was drilled by the rotary method with reverse mud circulation to a depth of 170.0 m. The borehole was drilled using a Wirth L4 drilling rig.

The borehole was drilled with a 1.16-m-diameter pipe bit to a depth of 8.0 m, where the surface casing ϕ 0.92 m was installed. After this column was cemented to the top and the cement slurry set, further drilling was carried out to the planned depth with a ϕ 0.76 m cutter bit. Afterwards, a steel pipe filtering column with a nominal diameter of 0.356 m was installed, followed by a resin-bonded gravel-packed filter, of the following design:

- overfilter pipe 55.0 m long, outer ϕ 0.356 m,
- I filter section 9.0 m long, outer ϕ 0.45 m,
- interfilter pipe 6.0 m long, outer ϕ 0.356 m,
- II filter section 13.0 m long, outer ϕ 0.45 m,
- interfilter pipe 270 m long, outer ϕ 0.356 m,
- III filter section 10.0 m long, outer ϕ 0.45 m,
- subfilter pipe 40.0 m long, outer ϕ 0.356 m.

The annular space between the borehole wall and the filtering column was filled with gravel pack of granulation 3–5 mm.

4. Types of drilling mud

The dewatering borehole was drilled with the bentonite-polymeric mud, ensuring smooth and uncomplicated drilling process. However, in the course of drilling through loose formations, this mud is responsible for the formation of a compacted sediment on the borehole wall and the mechanical colmatation of the pore space in the near-borehole zone of the aquifer. As a consequence, the permeability of the near-borehole zone is decreased in the aquifer and the resistance to water flow into the well grows [1, 3, 6]. The recipe of the mud used for drilling a dewatering well was the following:

- bentonite – 3%,
- polymer – 0.3%,
- Na_2CO_3 – 0.5%,
- Na_2HCO_3 – 0.2%,
- NaOH – 0.2%.

To improve the conditions of water filtration in the near-filter zone, the activation procedure was performed with agents disintegrating clayey minerals and removing them during treatment pumping operations.

5. Methodology for assessing hydraulic efficiency of a dewatering borehole

For the purpose of evaluating the quality of dewatering borehole construction and the effectiveness of activation treatments to improve water flow conditions in the filter zone, Jacob and Hantush methodics was used [1, 3]. Here the magnitude of total depression in the hydrogeological borehole, coming from laminar flow resistances in the aquifer as well as turbulent flow resistances in the near-filter zone, and the borehole itself, can be described with the formula below:

$$s = BQ + CQ^2 = s_w + \Delta \tag{1}$$

where:

s – total depression in a hydrogeological borehole with water pumping capacity of Q [m],
Q – pumping capacity (output) of the hydrogeological borehole [m^3/h],
B – resistance coefficient of laminar flow in the aquifer [h/m^2],
C – coefficient of turbulent flow resistance around the hydrogeological well, in the filter and in the filtering column; [h^2/m^5]; the C-factor is called the well resistance coefficient,
BQ – actual depression, resulting from the laminar flow of water in the aquifer,
CQ^2 – hydraulic drop.

It can be assumed for this model that the zone of turbulent motion, in which the nature of the flow changes from turbulent to laminar, is constant and independent of the pumping rate.

This theory was put into industrial practice after it was greatly simplified by Bruin and Hudson [1]. According to this methodology, Jacob's initial formula (1) was written in the form:

$$\frac{s}{Q} = B + CQ \tag{2}$$

and after its transformation the equation assumes the following form:

$$C = \frac{s - BQ}{Q^2} = \frac{\frac{s}{Q} - B}{Q} \tag{3}$$

Equation (3) can be solved graphically, as visualized in Figure 1. The graphical representation of unit depression s/Q in the function of Q rate helps determine coefficients B and C [1, 3, 4].

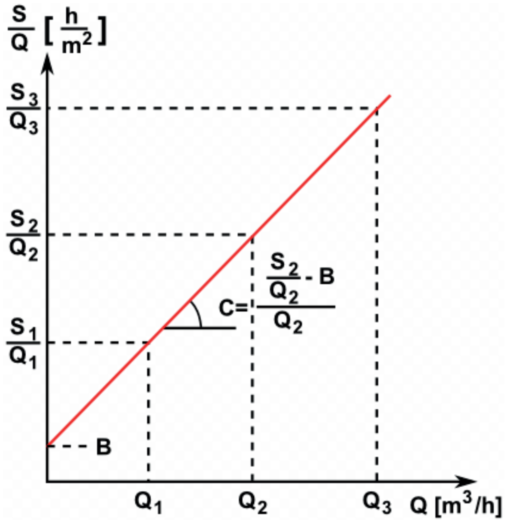

Fig. 1. Graphical method for assessing hydraulic efficiency of a hydrogeological borehole, after Bruin and Hudson procedure (2)

Having the results of multistage pumping, the values of s_1/Q_1; s_2/Q_2; s_3/Q_3, etc. for successive stages of pumping are plotted on the axis of ordinates of the aforementioned diagram, and corresponding values of well discharge Q_1; Q_2; Q_3, etc. on the axis of abscissa. The plotted points should form a straight line, whereas its extension to the intersection of the axis of ordinates determines the numerical value of the hydraulic resistance coefficient of the aquifer B. The value of the tangent of the angle of inclination of the determined straight line defines the numerical value of the hydraulic resistance coefficient of well C, in compliance with the formula:

$$C = \frac{\frac{s_2}{Q_2} - B}{Q_2} \tag{4}$$

The value of the C indicates the amount of hydraulic resistance in the infiltration zone and in the borehole itself, so it can be considered a measure of the hydraulic condition of the borehole. Below are given values of C[h²/m⁵] corresponding to various degrees of hydraulic efficiency of hydrogeological boreholes [2, 6]:

- properly designed and constructed – $C < 0.00015$,
- moderately contaminated or colmatated – 0.00015–0.00030,
- advanced contamination or colmatation – 0.00030–0.00120,
- considerably contaminated or colmatated – >0.00120.

6. Treatment pumping

After the filtering column was installed in the borehole and gravel pack introduced, drilling mud was removed from the borehole with an air lift. Then a 72-hour treatment pumping was followed with a pumping unit at three degrees of depression. This pumping was aimed at cleaning the porous space, prefilter zone of the aquifer, gravel pack and the filter, from the deposited material from mud in the form of fine cuttings and clayey minerals. The results of the treatment pumping of the intake well are shown in Table 1.

Table 1. Results of treatment pumping

Pumping degree	Rate Q [m³/h]	Depression s [m]	Unit depression s/Q [h/m²]
I	50.0	4.72	0.0940
II	100.0	10.61	0.1060
III	150.0	17.97	0.1193

The calculation of the efficiency factor $C = 0.00034$ h²/m⁵ with Walton method reveals that the completed dewatering borehole belongs to Class III, i.e. a borehole with advanced contamination. Thus, prior to being put into operation, the borehole absolutely requires an activation treatment to improve its efficiency.

7. Activation of a dewatering borehole using SKINAUT agent

In order to decolmatize the filter zone of the aquifer and improve the conditions of water inflow to the watering borehole, an activation procedure was performed using a new clay mineral particle disintegrating agent called SKINAUT. For this purpose, a solution of above-mentioned agent was gravity-injected into the filtering column through the string at a distance of up to 0.5 m. After the solution of the SKINAUT clay mineral disintegrating agent was injected into the filter zone, a 24-hour shutdown followed. Then, after the pumping unit was installed in the well, the treatment pumping was repeated at three degrees of depression. The obtained results of this operation are shown in Table 2.

Table 2. List of results of treatment pumping followed by clayey mineral disintegration treatments

Pumping degree	Rate *Q* [m^3/h]	Depression *s* [m]	Unit depression *s*/*Q* [h/m^2]
I	70.0	3.12	0.0445
II	140.0	6.93	0.0495
III	210.0	13.15	0.0626

The analysis of the obtained results of treatment pumping, following the dewatering borehole activation procedure and the performed calculations of the well efficiency factor $C = 0.00023\ h^2/m^5$ indicate that the borehole should be classified as Class II, i.e. moderately contaminated or colmatated. The results of treatment re-pumping demonstrate the high efficiency of the agent for disintegration of clayey mineral particles and its applicability aspects in hydrogeological drilling.

8. Concluding remarks

When dewatering boreholes are drilled by the rotary method with the use of drilling mud, the permeability of the rock in the near-borehole zone is damaged as a result of the colmatation of the pore space of the drilled aquifer with the solid phase of the drilling mud.

In Poland, the most common method used for this purpose is purge pumping carried out for 24 or 72 hours at three degrees of depression. Though this procedure is simple to perform, it remains relatively ineffective, and in most cases does not allow for effective unclogging of rocks in the near-well zone, especially of the clayey material.

For the purpose of increasing the effectiveness of treatments to activate hydrogeological boreholes drilled with rotary drilling mud, a new agent for the disintegration of clay minerals called SKINAUT has been developed. The procedure carried out to activate the Szczerców open cast dewatering borehole reveals that a method relying on a new clay mineral disintegration agent called SKINAUT is one of the most efficient ways to decolmatize the near-filter zone. This treatment has significantly improved its hydraulic efficiency and reclassified the borehole from Class III (a borehole with advanced colmatization) to Class II (a borehole with moderate colmatization).

Funding: This paper was written within the framework of own research program carried out at the Faculty of Drilling, Oil and Gas of AGH University of Krakow.

Conflicts of Interest: The author of this paper declares no conflicts of interest.

References

[1] Siwek Z., Mańkowski M.: *Wyznaczanie parametrów hydraulicznych ujęcia wód podziemnych na podstawie pompowań*. Kombinat Geologiczny Północ, Warszawa 1981.

[2] Macuda J., Łaciak S.: 2009: *Metody uaktywnienia i renowacji studni i piezometrów, praktyczne przesłanki ich stosowania w KWB Bełchatów*. WWNiG AGH, Kraków [unpublished].

[3] Gonet A., Macuda J.: *Wiertnictwo hydrogeologiczne*. Uczelniane Wydawnictwa Naukowo-Dydaktyczne AGH, Kraków 2004.

[4] Macuda J., Wysocki S.: *Środek do dezintegracji minerałów ilastych*. Patent PL230930B1.Udziel. 2018.09.10, 2019.

[5] Baraniecka M.: *Budowa geologiczna rejonu bełchatowskiego*. Przegląd Geologiczny, 7, 1980, pp. 381–390.

[6] Macuda J.: *Technika i technologia wiercenia studni odwadniających na złożu Szczerców*. WWNiG AGH, Kraków 2020 [unpublished].

Journal of Geotechnology and Energy | vol. 41 | no. 4 | 2024 | pp. 11–20

https://doi.org/10.7494/jge.2024.41.4.6740

ARTICLE

SIMULATIONS OF THE BEHAVIOR OF A PIPELINE MADE FROM THREE DIFFERENT TYPES OF MATERIALS ON A LANDSLIDE

Iwona Kowalska-Kubsik

AGH University of Krakow, Faculty of Drilling, Oil and Gas, Poland
ORCID: 0000-0003-0708-2937
e-mail: ikk@agh.edu.pl

Date of submission:
19.11.2024

Date of acceptance:
26.11.2024

Date of publication:
30.12.2024

https://journals.agh.edu.pl/jge

Abstract: The study presents numerical analyses of the behavior of pipelines made from various materials (steel, polypropylene, composite) under landslide conditions. Landslides are phenomena most commonly occurring in foothill and mountainous areas, and pipelines located on slopes can sustain damage during the landslide process. To determine the nature and extent of potential damage, numerical simulations were conducted based on advanced computational methods. The analysis employed the Drucker-Prager constitutive soil model.

Numerical analyses make it possible to determine the deformation and stress states in pipelines without the need for costly experimental studies. By comparing simulation results for different materials, it is possible to assess the suitability of various pipes for placement on slopes.

Keywords: numerical simulation, landslide, gas pipe, materials

1. Introduction

The problem of constructing pipelines in mountainous areas in relation to landslides is challenging to solve due to the typically complex geology. When laying pipelines on slopes, which is unavoidable in mountainous regions, one must consider the potential adverse phenomena that may occur, such as landslides. During the landslide process – characterized by the movement of soil masses – a pipeline situated in this zone is subjected to forces caused by the movement of these soil masses. This leads to deformations that can result in significant distortions (e.g., pipeline constrictions) or even ruptures. Pipes used in pipeline construction are, in most cases of minor mass movements, strong enough that there is no need for costly geotechnical solutions like retaining walls or pipeline anchoring. Often, it is sufficient to identify the most suitable position on the slope where the forces acting on the pipeline do not exceed its strength.

Pipelines in landslide areas require regular maintenance and monitoring to ensure their continuous safety and functionality. This may include regular inspections, geotechnical slope monitoring, and early warning systems to detect any signs of instability or potential landslide activity.

Constructing pipelines in landslide areas involves adherence to specific regulations and standards. Regulatory organizations may require comprehensive geotechnical studies, risk assessments, and compliance with safety guidelines to protect people, property, and the environment.

Addressing these issues requires a multidisciplinary approach involving geotechnical engineers, pipeline designers, and environmental experts. Careful investment planning, thorough field studies, and the implementation of appropriate engineering solutions are crucial to reducing the risks associated with pipeline construction in landslide-prone areas

Gas pipelines are critical strategic infrastructure and avoiding damage to them caused by natural phenomena or human activities is of great practical importance. However, as long, linear engineering structures, such pipelines are often vulnerable to landslide-induced damage [1–3]. Such damage can lead to significant deformation or pipeline rupture, resulting in natural gas leaks, interruptions in pipeline transport, and even potential threats to human lives.

Preventing losses caused by adverse phenomena in landslide-prone areas and controlling these hazards is an issue requiring further research. The number of studies on landslides impacting gas and oil pipelines is steadily increasing [4–11]. Most of these studies focus on examining mechanical behavior, analyzing weak points in these structures, and identifying factors affecting pipeline behavior during landslide activity. These works primarily provide theoretical results, while practical indicators for predicting and preventing pipeline damage due to landslide activity are lacking.

Practice shows that before the ground collapses, characteristic features such as cracks, fissures, or soil sliding can be observed on the surface. These signals allow for an approximate estimation of when the advanced landslide process will begin and what its range might be. However, it is still necessary to monitor and even assess the potential pipeline damage caused by landslides. For example, if the landslide's range, such as its width, were known, it would be possible to more accurately estimate whether the pipeline would be damaged. Furthermore, a developed indicator would provide a reliable basis for emergency response actions, allowing rescue services to take appropriate measures to minimize damage.

Landslides are difficult-to-control and unpredictable phenomena in terms of their range and nature. The most common factors contributing to landslides include main points:

- Layered soil structure parallel to the slope incline: This alignment promotes slippage and slope destabilization.
- Water buoyancy and seepage pressure in the slope: Water accumulation in the slope can increase pressure and reduce shear resistance, leading to landslides.
- Upward water pressure on the upper soil layers: Water accumulating at the base of a slope often contributes to the initiation of landslides.
- Soil saturation from rainfall: Rainfall causes soil to become saturated with water, resulting in swelling and a reduction in shear strength.
- Presence of natural potential slip surfaces: Such surfaces, especially in clay soils, facilitate the formation of landslides.
- Erosion or undercutting of the slope: Erosive actions, such as surface water flow or undercutting by groundwater, can destabilize the slope.

Landslides are usually triggered by a combination of several factors, often exacerbated by human activities. In urbanized areas, human influence is frequently decisive, with adverse actions including slope undercutting, changes in landform, loading or unloading of slopes, dynamic actions on the ground (e.g., vibrations), changes in land use (deforestation, plowing), and the manipulation of water flow direction towards slopes.

Given the complexity of situating pipelines on slopes, conducting experimental studies is challenging and highly costly. Therefore, the use of numerical tools to analyze pipeline behavior on landslides, particularly in the context of using different pipeline materials, enables the creation of multiple landslide movement scenarios using only computational resources.

The conclusions drawn from these numerical analyses can provide essential engineering insights for pipeline designers, operators, and regulatory institutions. This approach facilitates more informed decision-making in design, construction, and management, ensuring safe and reliable pipeline operation in landslide-prone areas.

The study conducted simulations of the behavior of pipelines made from various materials under the conditions of progressive landslides. The analysis aimed to compare the performance of three materials: standard steel typically used in the construction of high-pressure gas pipelines, polyethylene used in the construction of low-, medium-, and elevated-medium-pressure gas pipelines, and a composite material based on an epoxy resin matrix reinforced with fiberglass, suitable for high-pressure gas pipelines.

To simulate the phenomena causing pipeline damage, initial-boundary conditions closely resembling real-life scenarios were applied in the models, utilizing records and failure reports from gas distribution networks. In the selected cases, the key factors influencing failures were the strength parameters and quality of the materials used for pipeline construction, as well as the pipeline's foundation – specifically, its placement on potential landslides or subsidence areas, which significantly affect the extent of the resulting damage.

2. Fundamentals of simulation

Numerical analyses were conducted using the Finite Element Method in the ANSYS system [12]. The FEM method is a numerical approximation technique used to solve partial differential equations, which serve as the mathematical model for solving the given engineering problem. FEM is one of the discretization methods for continuous geometric systems, dividing the body into a finite number of subdomains. The main idea of FEM is to model even highly complex structures by representing them with geometrically simple components, including accounting for discontinuities.

The method involves dividing the continuous geometric model into finite elements interconnected at nodes, resulting in a discrete geometric model. This discretization transforms a system with an infinite number of degrees of freedom into one with a finite number of degrees of freedom. FEM's most significant advantage is its ability to replace an analytical problem, expressed through differential equations, with an algebraic one. The method approximates displacement fields, stress fields, or both within each finite element.

FEM can be used for both static and dynamic analyses. It allows for the evaluation of actual geometries of slopes or subsidence areas and supports advanced constitutive models for granular materials. One of the most commonly used soil constitutive models is the elastic-plastic model.

In addition to FEM, other numerical approaches are used for phenomena such as flows or large deformations, including methods such as Finite Volume Method – based on volume elements, Discrete Element Method and Meshless Methods e.g. Material Point Methods.

The numerical methods allow for tracking the phenomenon over time, monitoring the elements (their deformations, displacements and stresses) in successive time steps under changing boundary conditions or loads. As a result, it is possible to trace the entire process of pipeline damage development.

3. Numerical analysis overview

Simulations were performed for pipelines made of three different materials: polyethylene, composite, and steel. Each pipeline was modeled operating on a landslide. For simulation purposes, geometric models of the landslide were created, with the pipeline positioned at a depth of 0.8 m in soil in the middle part of slope. For each material, three separate pipeline models were created to account for differences in pipe geometry, including variations in diameter and wall thickness. Consequently, numerical simulations were conducted for three cases.

Landslide geometric model

The slope model had a height of 15 m and an angle of inclination of 31°, as shown in Figure 1.

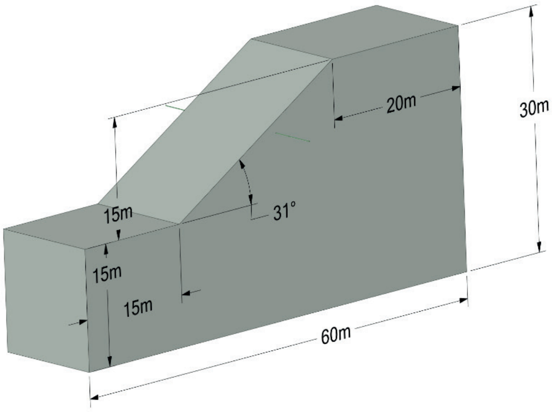

Fig. 1. Geometric model of the slope with a pipeline placed on it

The geometric models were discretized using hexahedral and tetrahedral meshes of varying sizes, depending on the analyzed model. The soil models required a coarser mesh due to their larger scale, while the pipeline was discretized with a dense hexahedral mesh for accuracy. Figure 2 presents the mesh of elements used for the analysis.

The material properties and dimensions of the pipes were based on actual operating pipeline segments. The dimensions and material properties of the composite pipe were obtained from a manufacturer's specifications, which promoted the pipe as safe for transporting 100% hydrogen. The material properties are presented in Table 1.

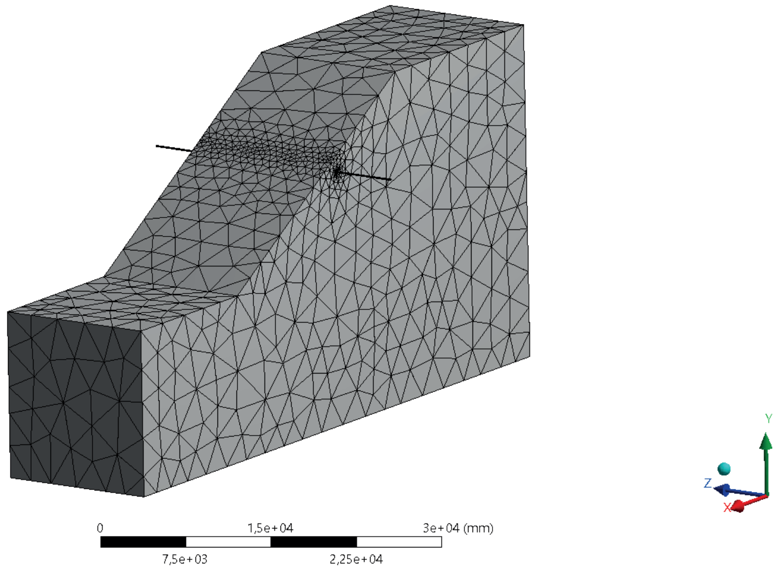

Fig. 2. Mesh of elements of landslide

Table 1. Summary of material parameters used in simulations

Property	Material		
	Composite	Polyethylene	Steel
Density [kg/m^3]	1 450	950	7 850
Thermal expansion coefficient [1/°C 0 · 10^6]	X: 2.2	230	–
	Y: 2.2		
	Z: 10		
Young's modulus [GPa]	X: 61.3	1.1	200
	Y: 61.3		
	Z: 6.9		
Poisson's ratio [–]	XY: 0.04	0.42	0.3
	YZ: 0.3		
	XZ: 0.3		
Shear modulus [GPa]	X: 3.3	0.39	76.9
	Y: 2.7		
	Z: 2.7		
Bulk modulus [GPa]	–	2.29	167
Specific heat [J/kg · °C]	–	2 300	434
Yield strength [MPa]	–	25	390
Tensile strength [MPa]	900	33	550
Isotropic thermal conductivity [W/m · °C]	–	0.28	–

Pipe parameters of materials and dimensions:

1. Polyethylene Pipe (PE100HD):
   - internal gas pressure: 3 bar,
   - external dimension of pipe: 110 mm,
   - internal dimension of pipe: 90 mm,
   - wall thickness: 10 mm;
2. Steel Pipe (L360):
   - internal gas pressure: 30 bar,
   - external dimension of pipe: 108 mm,
   - internal dimension of pipe: 100.4 mm,
   - wall thickness: 3.8 mm;
3. Composite Pipe (Fiberglass-Epoxy Matrix):
   - internal gas pressure: 30 bar,
   - external dimension of pipe: 115 mm,
   - internal dimension of pipe: 100 mm,
   - wall thickness: 7.5 mm.

The presented internal pressures of pipelines result from the operating pressures for these types of pipes. For polyethylene, internal pressures up to 3 bar are applied, while for other materials, significantly higher pressures, up to 30 bar, are used.

Numerical analysis of soil using constitutive models

Two primary soil constitutive models are commonly used for numerical analyses: the Coulomb–Mohr model and the Drucker–Prager model. For example, the yield condition for the Drucker–Prager model can be expressed as follows [13]:

$$f(\sigma_{ij}) = q - mp - k \tag{1}$$

The parameter m is defined as:

$$m = \frac{18\sin\phi}{9 - \sin 2\phi} \tag{2}$$

The parameter $\boldsymbol{k}$ is expressed as:

$$k = \frac{18c\cos\phi}{9 - \sin 2\phi} \tag{3}$$

where:
ϕ – internal friction angle,
c – cohesion,
p and q – stress tensors invariants, defined as:

$$p = -\frac{1}{3}\sigma_{ii},\ q = \sqrt{\frac{3}{2}(s_{ij}s_{ij})} \tag{4}$$

where:

$$s_{ij} = \sigma_{ij} + \delta_{ij} \tag{5}$$

represents the deviatoric part of the stress tensor σ_{ij}.

In most works related to plasticity theory in equation (1), coefficients m and k are defined as follows in (6) and (7) when the Drucker–Prager cone is inscribed around the external edges of the Coulomb–Mohr pyramid:

$$m = \frac{6\sin\phi}{3 - \sin\phi} \tag{6}$$

$$k = \frac{6c\cos\phi}{3 - \sin\phi} \tag{7}$$

Figure 3 provides a geometric interpretation of the principal stress space σ_1, σ_2, σ_3 on the plasticity surfaces in showing the Coulomb–Mohr pyramid and the Drucker–Prager cone.

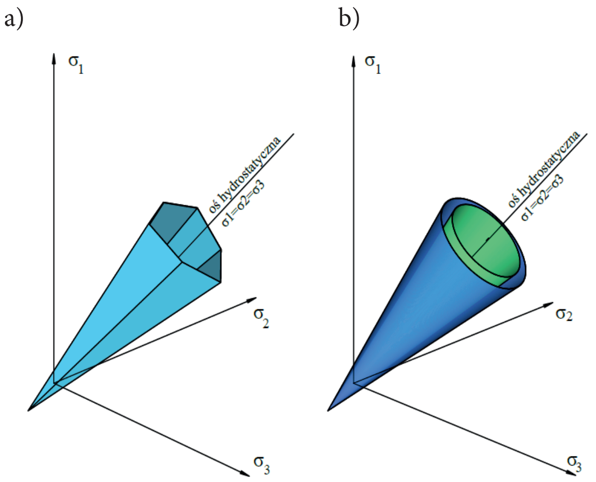

Fig. 3. Drucker–Prager Cone vs. Coulomb–Mohr Pyramid: a) Coulomb–Mohr pyramid; b) Drucker–Prager cones: blue (inscribed around external edges of the pyramid), green (circumscribed around internal edges of the pyramid)

The Drucker–Prager model was applied to the soil of the slope in this analysis, with the parameters outlined in Table 2.

Table 2. Soil parameters for simulation

Parameter	Value
Density ρ [kg/m³]	1 750
Young's modulus E [MPa]	50
Poisson's ratio ν [–]	0.29
Uniaxial compressive strength σ_c [MPa]	15
Uniaxial tensile strength σ_t [MPa]	$5 \cdot 10^{-5}$
Biaxial compressive strength σ_b [MPa]	20

Landslide-induced forces and pipeline-soil interaction

Based on the distribution of forces acting on the pipeline caused by landslide activity [14] and studies on pipe-soil interaction [15–19], the following assumptions were made:

- Forces modeled: Only gravitational forces causing landslide movement.
- Pipeline-soil interaction: Modeled as frictional contact, with a coefficient of friction of 0.6, consistent with design guidelines for pipelines embedded in soil.

This setup enabled a realistic simulation of landslide-induced stress and the resulting interaction between the soil and pipeline.

Boundary conditions and simulation setup

The analysis of prior research [20–21] significantly influenced the selection of the computational model. A slope model with an embedded pipeline was adopted, allowing for a realistic representation of pipeline-soil interaction. Additionally, various boundary conditions for the slope and pipeline end fixations were examined to assess their impact on pipeline behavior.

For simulation of free soil movement along a slope incline, the slope's boundaries were permitted to move freely in the direction of the incline, simulating natural landslide conditions, while the ends of the pipeline were fixed.

It is essential to note that the boundary conditions applied in the analysis, including contact surface size, load magnitudes, and directions, and contact configuration between the pipeline and soil, represent one example out of an infinite number of possible scenarios. These were modeled to approximate real-world conditions while allowing for predictable and interpretable results.

This detailed dataset formed the basis for simulating and analyzing the performance of the pipelines under landslide conditions.

4. Results

Figure 4 illustrates the deformation of the landslide along with the pipeline situated on it, highlighting the direction of soil mass movement during the landslide process. As the soil masses shift during the landslide, forces act on the pipeline located on the slope. These forces, determined by the nature of the soil movement, directly influence the deformation characteristics of the pipeline.

Due to the material properties (such as anisotropy), the figures below reveal varying deformation and stress patterns across the different types of materials used for the pipelines.

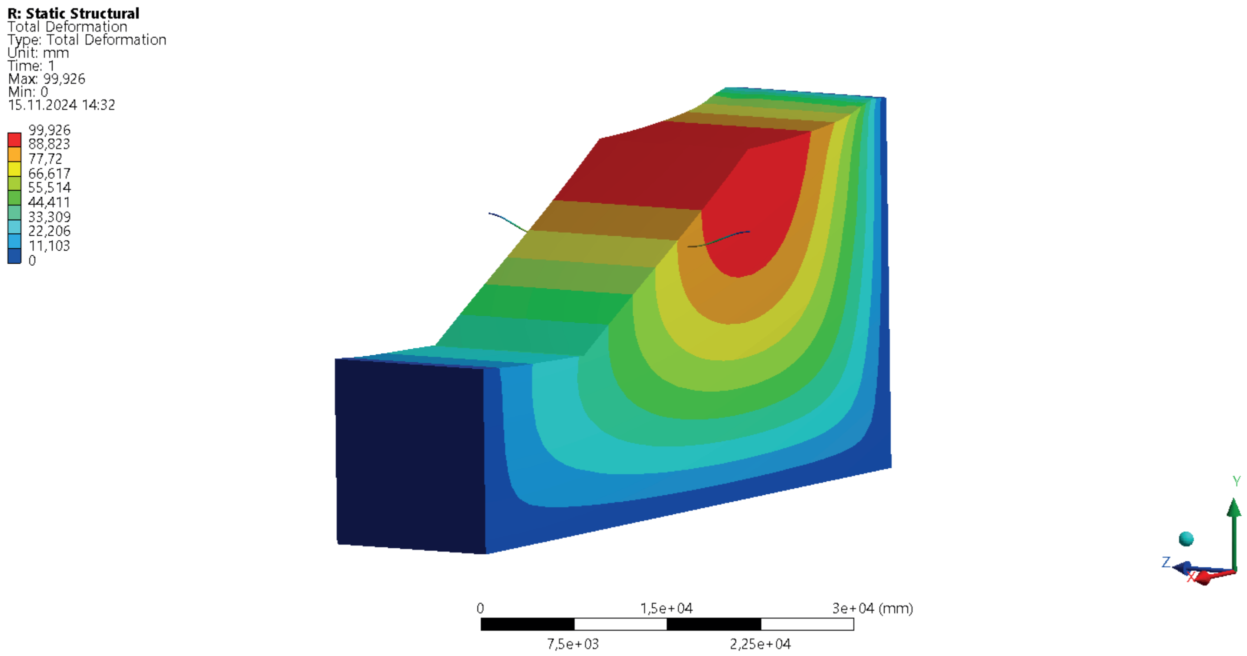

Fig. 4. The deformation profile of the landslide along with the embedded pipeline

Steel pipeline

Figure 5 presents the deformation profile of the steel gas pipeline at the maximum deformation recorded (at a specific time step), with a displacement of 111 mm. Figure 6 presents the stress distribution in the steel gas pipeline at the same moment in the simulation. The deformation visuals have been exaggerated to emphasize their characteristics.

Composite pipeline

Figure 7 presents the deformation profile of the composite gas pipeline at the maximum deformation recorded (at a specific time step), with a displacement of 99 mm. Figure 8 presents the stress distribution in the composite gas pipeline at the same moment in the simulation.

A uniform stress distribution is visible along the entire length of the pipe, with no distinct areas of higher intensity.

Polyethylene pipeline

Figure 9 presents the deformation profile of the polyethylene gas pipeline at the maximum deformation recorded (at a specific time step), with a displacement of 84 mm. Figure 10 presents the stress distribution in a polyethylene pipeline at the same moment in the simulation.

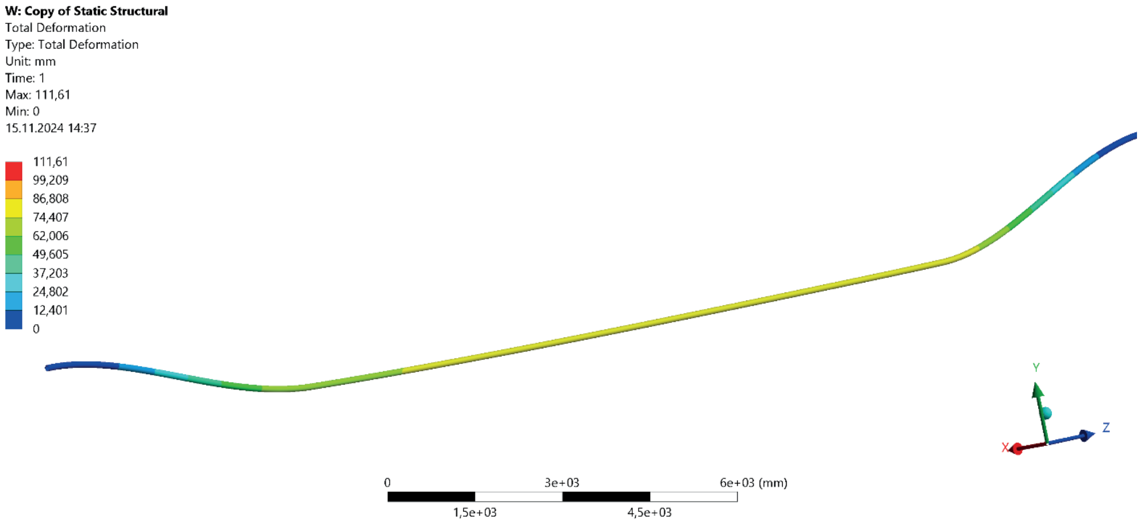

Fig. 5. The deformation profile of the steel pipeline

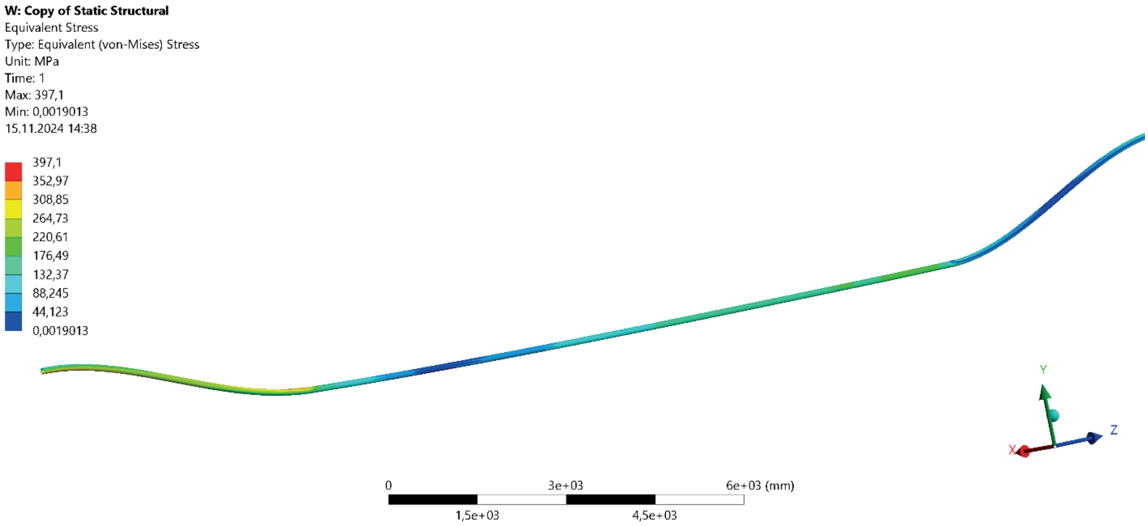

Fig. 6. Stress map of the steel pipeline

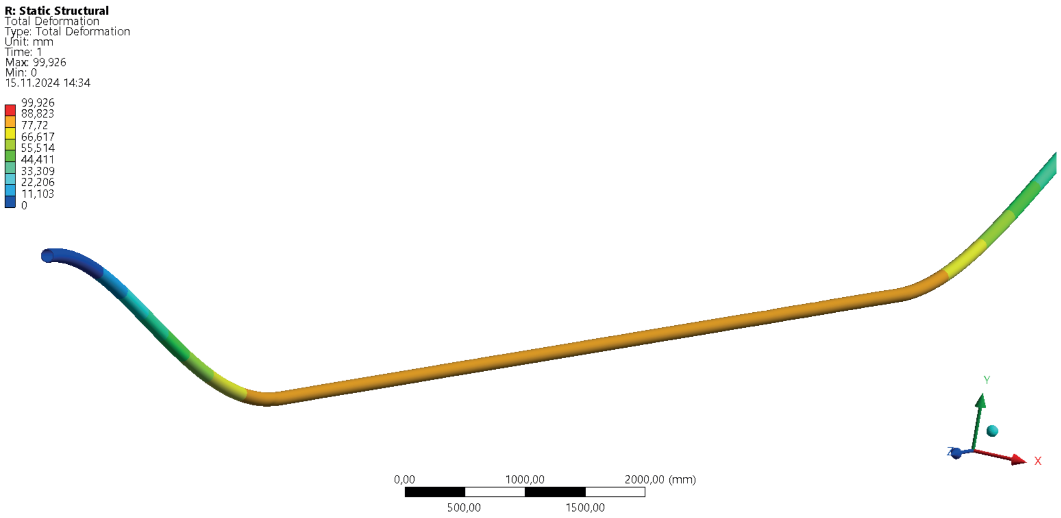

Fig. 7. The deformation profile of composite pipeline

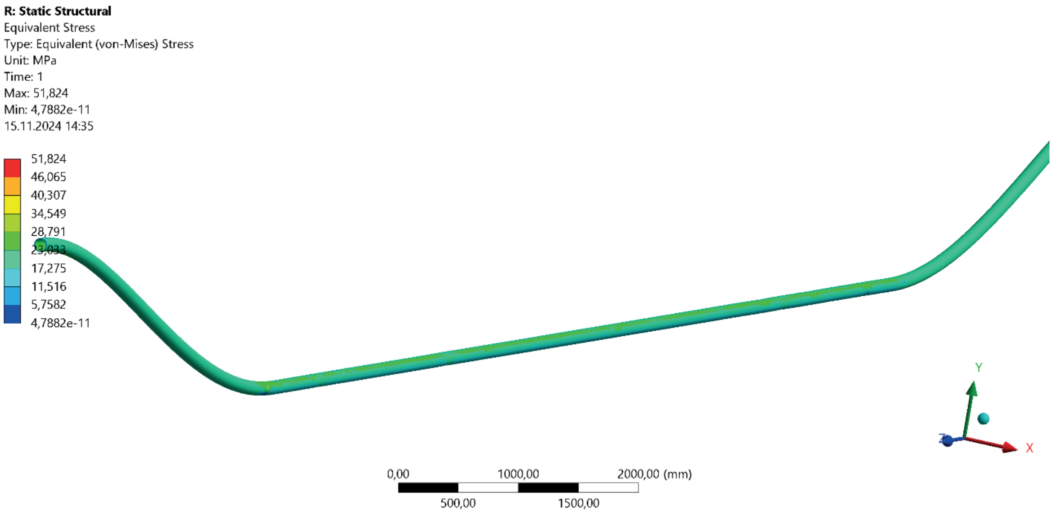

Fig. 8. Stress map of composite pipeline

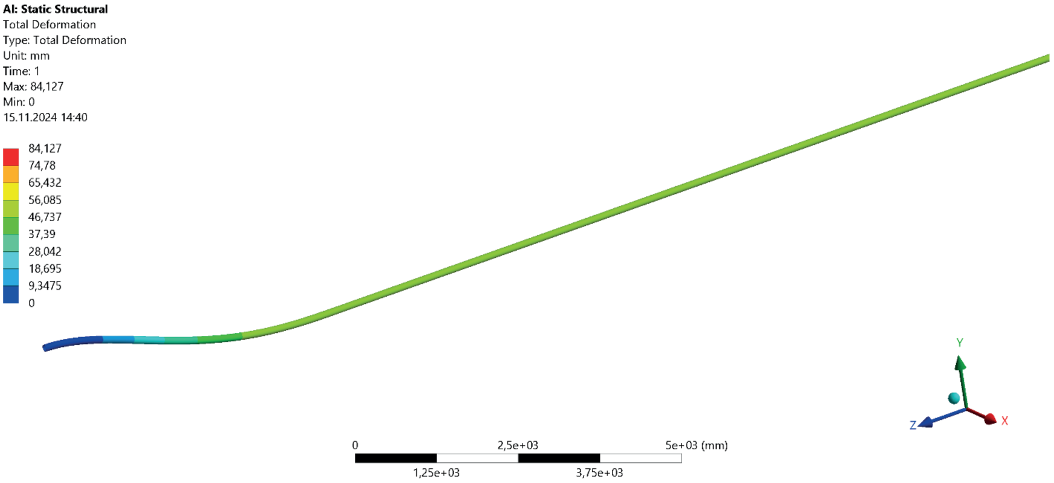

Fig. 9. The deformation profile of polyethylene pipeline

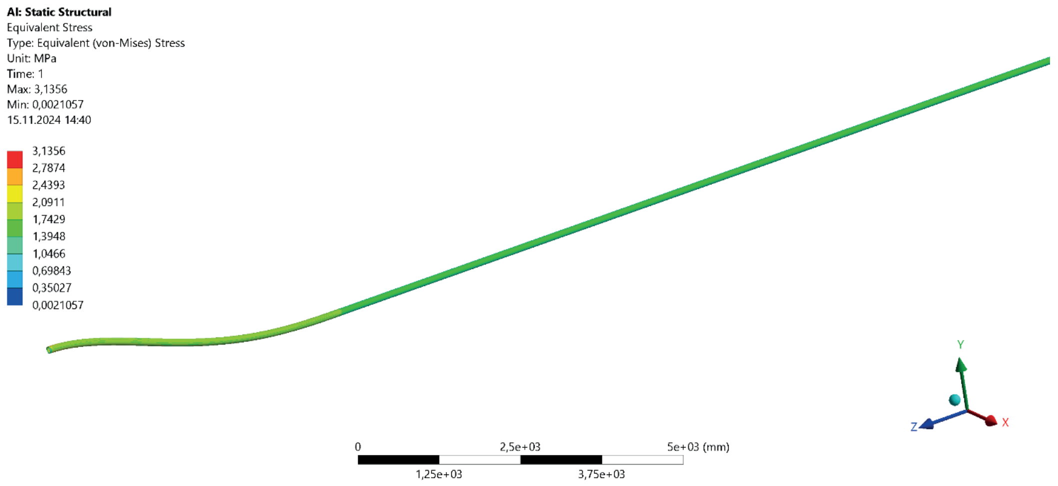

Fig. 10. Stress map of polyethylene pipeline

5. Conclusions

Analyzing the results obtained from the simulations of both deformations and stresses in the pipeline within the context of the research assumptions – namely, determining the behavior of different pipeline materials on landslides – it can be concluded that the most versatile material is the composite. This is evidenced by its relatively low stress values on the pipe at the edge of the landslide compared to steel pipes, although higher than polyethylene pipes. Polyethylene also exhibits greater susceptibility to deformation compared to steel, with maximum stress values of approximately 6 MPa, reflecting its flexibility. In steel pipes, the stress reaches around 300 MPa, while in composites, it is about 50 MPa. Comparing analyses of various pipeline materials under similar landslide conditions allows for a more accurate selection of pipeline materials in the design processes of gas transmission systems.

The comparative analysis of different pipeline materials under similar landslide conditions enables a more informed selection of materials during the design process of gas pipelines.

Funding: The project was supported by the AGH University of Krakow, subsidy 16.16.190.779.

Conflicts of Interest: The author of this paper declares no conflicts of interest.

References

[1] Zhou X.Y., Guo Y.H., Lv X.H., Yang Y.: *Study on Effects of Different Factors on Pipelines Risk under Landslide.* Industrial Safety and Environmental Protection, 38, 2012, pp. 42–44.

[2] Xue H., Yang X.Q.: *Design and Construction of Sino-Burma Oil-Gas Pipeline in Typical Geological Hazard Areas.* Oil & Gas Storage and Transportation, 32, 2013, pp. 1320–1324.

[3] Ho D., Wilbourn N., Vega A., Tache J.: *Safeguarding a Buried Pipeline in a Landslide Region.* Pipelines 2014, Portland Oregon, 3–6 August 2014, pp. 1162–1174. https://doi.org/10.1061/9780784413692.105.

[4] Lin D., Lei Y., Xu K.F. et al.: *An Experiment on the Effect of a Transverse Landslide on Pipelines.* Acta Petrolei Sinica, 32, 2011, pp. 728–732.

[5] Lin D., Xu K.F., Huang R.Q. et al.: *Landslides Classification of Pipeline for Transporting Oil and Gas.* Welded Pipe and Tube, 32, 2009, pp. 66–68.

[6] Wang L., Deng Q.L.: *Mechanical Analysis on the Safety of Gas-Transporting Pipeline Caused by Landslide for Deformation.* Journal of Engineering Geology, 18, 2010, pp. 340–345.

[7] Kinash O., Najafi M.: *Large-Diameter Pipe Subjected to Landslide Loads.* Journal of Pipeline Systems Engineering and Practice, 3, 2012: 1–7. https://doi.org/10.1061/(ASCE)PS.1949-1204.0000091.

[8] Magura M., Brodniansky J.: *Experimental Research of Buried Pipelines.* Procedia Engineering, 40, 2012, pp. 50–55. https://doi.org/10.1016/j.proeng.2012.07.054.

[9] Zhao X.Y., Zhao Y.: *Strain Response Analysis of Oil and Gas Pipelines Subject to Lateral Landslide.* Journal of Natural Disasters, 23, 2014, pp. 250–256.

[10] Huang K., Lu H.F., Wu S.J. et al.: *The Stress Analysis of Buried Gas Pipeline Crossing the Landslide.* Chinese Journal of Applied Mechanics, 32, 2015, pp. 689–693.

[11] Liu W.Q., Zheng J., Wu H.G. et al.: *Experimental Study on Effect of Orthogonal Landslide on Pipe by Model Simulation.* Railway Engineering, 6, 2015, pp. 117–120.

[12] ANSYS Inc.: *ANSYS Documentation.* 2024.

[13] Więckowski Z.: *The Material Point Method in Large Strain Engineering Problems.* Computer Methods in Applied Mechanics and Engineering, 193(39–41), 2004, pp. 4417–4438. https://doi.org/10.1016/j.cma.2004.01.035.

[14] Hao J.B., Liu J.P., Jing H.Y., Zhang H., Shen F., Tong H., Liu L.: *A Calculation of Landslide Thrust Force to Transverse Pipeline.* Acta Petrolei Sinica, 33(6), 2012, pp. 1093–1097. https://doi.org/10.7623/syxb201206025.

[15] Calvetti F., di Prisco C., Nova R.: *Experimental and Numerical Analysis of Soil-Pipe Interaction.* Journal of Geotechnical and Geoenvironmental Engineering, 130, 2004, pp. 1292–1299. https://doi.org/10.1061/(ASCE)1090-0241(2004)130:12(1292).

[16] Li H., Xu Z., Yang Y.H., et al.: *Strength Failure Analysis of Buried Piping Loaded with Landslide.* Process Equipment & Piping, 49, 2012, pp. 54–57.

[17] Alam S., Allouche E., Bartlett C. et al.: *Experimental Evaluation of Soil-Pipe Friction Coefficients for Coated Steel Pipes.* Pipelines 2013 Conference, Fort Worth, 22–26 June 2013, pp. 360–371. https://doi.org/10.1061/9780784413012.034.

[18] Dezfooli M., Abolmaali A., Razavi M.: *Coupled Nonlinear Finite-Element Analysis of Soil-Steel Pipe Structure Interaction.* International Journal of Geomechanics, 15, 2015, art. 04014032. https://doi.org/10.1061/(ASCE)GM.1943-5622.0000387.

[19] Vazouras P., Dakoulas P., Karamanos S.A.: *Pipe-Soil Interaction and Pipeline Performance under Strike-Slip Fault Movements.* Soil Dynamics and Earthquake Engineering, 72, 2015, pp. 48–65. https://doi.org/10.1016/j.soildyn.2015.01.014.

[20] Deng D.M., Zhou X.H., Shen Y.P.: *Calculation of Pipeline Inner Force and Distortion during Transverse Landslide Body.* Oil & Gas Storage and Transportation, 17, 1998, pp. 18–22.

[21] Griffiths D.V., Lane P.A.: *Slope Stability Analysis by Finite Elements.* Géotechnique, 49, 1999, pp. 387–403. https://doi.org/10.1680/geot.1999.49.3.387.

Journal of Geotechnology and Energy | vol. 41 | no. 4 | 2024 | pp. 21–26

https://doi.org/10.7494/jge.2024.41.4.6733

ARTICLE

USE OF INCLINED BOREHOLES AS INJECTION HOLES FOR FILLING BACKFILL CHAMBERS

Przemysław Toczek

AGH University of Krakow, Faculty of Drilling, Oil and Gas, Poland
ORCID: 0000-0002-4028-5907
e-mail: toczek@agh.edu.pl

Tomasz Kowalski

AGH University of Krakow, Faculty of Drilling, Oil and Gas, Poland
ORCID: 0000-0002-6767-6342
e-mail: tkowal@agh.edu.pl

Rafał Artym

Firma Usługowa AR-WIERT Rafał Artym,
ul. C.K. Norwida 8/30, 37-600 Lubaczów, Poland

Date of submission:
17.11.2024

Date of acceptance:
21.11.2024

Date of publication:
30.12.2024

https://journals.agh.edu.pl/jge

Abstract: The latest environmental trends involve the use of renewable energy sources, reducing carbon footprints and minimizing the effects of past human activity. It is therefore very important to minimize the effects of the exploitation of useful minerals by eliminating mining landslides and rock voids. One of the ways to protect them is through drilling works by drilling backfill holes. The authors of the present study show the possibility of adapting diagonal drillings to drill backfill boreholes. It helps to connect voids, caverns or cavities by backfill boreholes through the injection of backfill material into them. The time of pumping the backfill material in the case of vertical and diagonal holes are analyzed.

Keywords: inclined borehole, oblique borehole, borehole injection, restorative material, backfill material

1. Introduction

The need to use land for construction often makes it necessary to pay attention to eliminating the effects of the underground exploitation of useful minerals. One method of preventing mining landslides was the so-called protective pillars, i.e. leaving unmined coal or other material under settlements, roads, industrial plants, etc. However, it should be remembered that such protective pillars should be wider the deeper they are. This is because the rocks above the selected space break at a certain slope, depending on the type of rock. With soft rocks, the slope is less, while with hard rocks it is greater. Through this, the use of protective pillars results in the loss of a large amount of material which is easy to exploit. Increasing the intensity of the exploitation of geological raw materials leads to the activation of collapse processes [1]. An effective protective measure is filling the space left by the selected raw material with another material, such as rock or sand [2]. According to the mining dictionary, backfilling is the filling of an excavation with a non-mined material (rock), obtained either on site during mining or supplied from outside [3]. Backfilling should be understood as the material with which voids are filled after the selection of usable mineral [4, 5], and therefore also in the liquidation of workings and entire mines. Drilling methods are therefore increasingly being used to backfill post-mining workings and rock voids. Backfilling, or in other words restorative boreholes, can be used to easily and quickly inject material from the surface into a specific cavern or chamber. The most common design of such boreholes is based on the lithology of the rocks to be drilled and drilling guidelines. According to the literature, the most commonly used casings for backfilling boreholes have an outside diameter ranging from 18‘ to 12’, but there are boreholes with initial pipe diameters of more than 20‘ (e.g. borehole TP-25 in the Wieliczka Salt Mine) or final diameters which are much smaller (6 5/8’ pipe column used for backfilling transport) [6, 7].

The increase in activities has meant that the direction of accessing voids by drilling methods has become dominant. Drilling techniques and technologies allow voids to be accessed which are located, among others, under existing residential or public utility buildings, flooded voids or in crisis situations – e.g. voids in a fire condition [8]. Borehole injection is increasingly widely used in the process of strengthening rock masses or filling voids. It can be used in both geotechnics and hydrotechnics. It is used to strengthen and seal the ground medium or rock mass. There are many ways of performing injections, with the basic ones being the division into classic, pressure, and high-pressure injection [9, 10].

There are two main types of borehole injection for backfilling. The first is borehole injection using the “top” backfilling technology. It is used in the case of identified voids and loosening zones, without the need to perform reconnaissance work around the borehole. Boreholes for this technology are usually drilled using the coreless technique. In terms of principles, it was developed by Geocarbon LLC. Injection work should be carried out in a control borehole in the direction from the ground surface to the bottom of the borehole [11] and it is carried out in several stages as mentioned below:

- determination of the point of drilling the control hole using the geodetic method,
- drilling the hole and carrying out the injection works,
- control of the quality of the grout,
- control of the effectiveness of filling the voids and loosening zones.

In case of limited knowledge about the location of voids and loosening zones injection using the “bottom-up” technology is used. It is characterized by coring and performing reconnaissance work around the borehole. It is also carried out in several stages [11]:

- geodetic marking of the point of drilling the control hole,
- drilling the control hole,
- control measurements,
- backfilling of voids and loose zones,
- quality control of the grout,
- control of the effectiveness of backfilling of voids and loose zones.

Currently, the following methods are used for the treatment and backfilling of mining excavations [8]:

- hydraulic backfills,
- backfills made of dry and sprayed fly ash,
- ash pulps (suspensions),
- binding slurries.

The term conditioning or conditioning works should be understood as a set of activities aimed at sealing and strengthening the building substrate by filling all voids and loosening zones as tightly as possible [11].

Among the binding slurries, we can distinguish single-component and multi-component cement dusts, cement-sand mortars, cement-dust mortars, cement-ash mortars, cement-clay mortars, cement-ash-lime mortars and slag-cement mortars [8]. Additionally, chemicals based on polyurethane organic compounds, resins, or mineral aggregates can be used as backfill material [11]. The decision on the selection of individual media to be introduced into the rock mass to achieve the intended goal must take into account a whole range of conditions: from natural, through technical, to economic [8]. Backfill holes should be effectively closed immediately after fulfilling their function [7].

2. Results

Drilling boreholes, including backfill or restorative boreholes, are primarily intended to be made as straight holes but in some cases this cannot be done. One of the main limitations of drilling the backfill borehole is the frequent case when the drilling rig cannot be positioned above the void to be filled, e.g. due to the buildings, surface infrastructure or other factors. Moreover, there is a need to perform diagonal boreholes for chambers or voids intended for backfilling which are located under highly urbanized areas. It is also recommended to drill inclined backfill holes to provide a greater visible thickness of the chamber or void compared to the vertical hole. This increases the length of the perforated section of injection pipe used to inject the backfill material and also allows for a shorter injection time of the backfill material. In backfill boreholes, making an inclined backfill hole will have a direct effect on the time required to pump the backfill material. Assuming the same volume of the chambers to be backfilled in the case of the vertical hole and the inclined hole, and taking into account that the holes made will have the same internal diameters of the submerged casing pipes, the relationship for the flow rate of pumping the backfill material in the vertical hole can be written as:

$$Q_{\max(vertical)} = \pi D H v_{kr} \tag{1}$$

and for the oblique borehole as follows:

$$Q_{\max(oblique)} = \pi D L v_{kr} \tag{2}$$

where:

D – internal diameter of the last column of casing pipes [m],
H – length of the perforated section of the vertical hole [m],
L – length of the perforated section of the diagonal hole, $L = H/(\cos\alpha)$ [m],
v_{kr} – injection velocity [m/s],
α – angle of deviation from the vertical of the diagonal hole [°].

Table 1 shows the increase in oblique borehole length depending on the drilling angle.

Taking into account the values given in Table 1 and substituting them into the equations for the maximum pumping capacity in a vertical and oblique borehole, it can be stated that the pumping flow increases in the oblique borehole. To ensure laminar flow, the critical pumping speed v_{kr} should not be exceeded during injection. Using trigonometric relations, it can be stated that the increase in the length of the perforated hole section causes a proportional increase in the pumping flow.

Assuming the same volume of the chamber V intended for injection, when using a vertical or oblique hole, the chamber injection time is equalized. It can be written:

$$T_{vertical} = \frac{V}{Q_{\max(vertical)}} \tag{3}$$

and for the oblique borehole as follows ($Q_{max(Toblique)}$):

$$T_{oblique} = \frac{V}{Q_{\max(oblique)}} \tag{4}$$

where:

$T_{vertical}$ – injection time of vertical borehole [s],
$T_{oblique}$ – injection time of an oblique borehole [s],
V – voids or chamber volume [m^3].

Taking into account the above, at a constant volume of the chamber V, the increase in the flow for the oblique borehole due to increasing of perforation length results in a shortening of the time of injection the backfilling material into the chamber. Comparing the above mentioned equations at a constant volume of the chamber, the following relationship between the injection time in an oblique well and the injection time in a vertical well is obtained:

$$T_{oblique} = T_{vertical} \cdot \cos\alpha \tag{5}$$

The relationship can be presented in a tabular form (Tab. 2) for given values of the angle of drilling an oblique hole.

Table 1. Increase in the length of the oblique borehole depending on the drilling angle

Thickness for vertical borehole [m]	Apparent thickness for an oblique borehole due to angle of drilling [m]								
	10°	20°	30°	40°	45°	50°	60°	70°	80°
H	$\frac{H}{0.985}$	$\frac{H}{0.940}$	$\frac{H}{0.866}$	$\frac{H}{0.766}$	$\frac{H}{0.707}$	$\frac{H}{0.643}$	$\frac{H}{0.500}$	$\frac{H}{0.342}$	$\frac{H}{0.174}$

Table 2. Decrease of injection time through inclined borehole in comparison to vertical borehole

Injection time for vertical borehole [s]	Injection time for an oblique borehole due to angle of drilling [m]								
	10°	20°	30°	40°	45°	50°	60°	70°	80°
$T_{vertical}$	$0.985 \cdot T_v$	$0.940 \cdot T_v$	$0.866 \cdot T_v$	$0.766 \cdot T_v$	$0.707 \cdot T_v$	$0.643 \cdot T_v$	$0.500 \cdot T_v$	$0.342 \cdot T_v$	$0.174 \cdot T_v$

$^*T_v$ means $T_{vertical}$

The chamber was analyzed at different depths calculated from the ground surface. The lowest point of the chamber floor is at a depth of $H = 10$ m, the highest point of the chamber floor is at a depth of $H = 1.5$ m and the maximum vertical length of the perforated section is $H = 8$ m. The length of the perforated section making the chamber accessible for injection can be adjusted by changing the angle of the hole (Tab. 3).

Taking into account the increase in the length of the perforated section according to Table 3, it is possible to determine the injection time of the chamber through the diagonal hole made. The chamber to be backfilled has a defined volume. Assuming a constant value of the injection flow of the backfilling material, the pumping time through the vertical hole is determined.

Assuming an equal pumping rate of the backfill material through the vertical hole and the diagonal hole, the time for pumping the backfill material through the diagonal hole will be determined according to the time equation. It is found that the pumping of the material through the completed diagonal hole is carried out in a shorter time compared to the vertical hole, as shown in Figure 1.

Table 3. Dependence of the length of the perforated section of the hole on the angle of its execution

Thickness for vertical borehole [m]	Apparent thickness for an oblique borehole due to angle of drilling [m]								
8	10°	20°	30°	40°	45°	50°	60°	70°	80°
	8.12	8.51	9.23	10.44	11.31	12.44	16	23.39	46.07

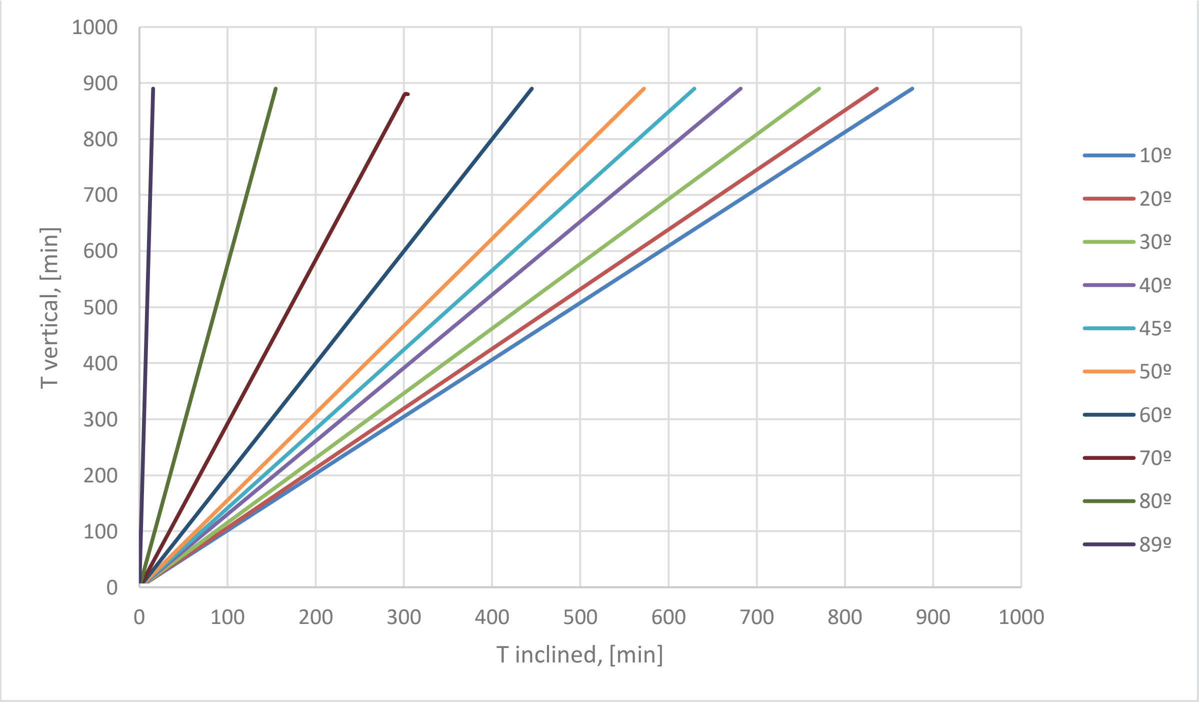

Fig. 1. Influence of the angle of the inclined borehole on the injection time of the backfill material compared to the injection time through a vertical borehole

The relationship between the pumping times of the backfill material through the oblique borehole and the pumping time through the vertical borehole of the same chamber is shown in the range of angles 10–89° at which an oblique borehole can be made. The situation where a diagonal hole is made at an angle of 89° will be rare, but cannot be excluded. At present, a number of scientific papers show that solutions for drilling small-diameter holes using hydraulic nozzles from base holes [12–14] are being used more and more frequently. Despite the small inside diameter of such holes, in the range of 50–70 mm, they can be easily adapted to make small-diameter injection channels when space is limited for drilling with standard equipment for shallow drilling up to 200 m vertical depth. The decrease in pumping time of the backfill material through an 89° inclined hole is significant. Since cos 60° = 0.5 and taking into account the above equations to facilitate quick calculations in the field, the pumping time through a diagonal hole made at an angle of $\alpha = 60°$, will always be about half of the pumping time through a vertical hole.

3. Conclusions

- Diagonal or inclined boreholes have a drilling angle other than vertical and a direction other than standard vertical boreholes from top to bottom. They can be drilled from the ground surface, from the interior of buildings/infrastructure and from the excavations of underground and opencast mines.
- The drilling of a diagonal hole is usually more difficult and exposed to drilling failures and complications compared to vertical drilling. This is strictly connected with an angle of internal friction each drilled lithological layer.
- The use of inclined boreholes will lead to an economic gain by reducing the time it takes to inject the backfill material into the infilled chamber or mine workings void.
- The pumping time through a diagonal hole drilled at an angle of $\alpha = 60°$ will always be about half that of a vertical hole.

Author contributions: Conceptualization PT and AR, formal analysis TK, methodology TK, writing – review and editing, writing – original draft preparation, and investigation, PT and AR and TK, supervision, validation, project administration, PT. All authors have read and agreed to the published version of the manuscript.

Funding: This research received no external funding.

Conflicts of Interest: The authors of this paper declare no conflicts of interest.

References

[1] Kubański A., Zych J., Zawada S.: *Technologie likwidacji płytkich wyrobisk górniczych.* In: Kubański A., Zych J., Zawada S. (red.), *Technologie likwidacji pustek w górotworze. Międzynarodowa Konferencja: V Szkoła Geomechaniki. Katedra Geomechaniki, Budownictwa Podziemnego i Ochrony Powierzchni Wydziału Górnictwa i Geologii Politechniki Śląskiej. Ustroń – 16–19 października 2001*, pp. 323–334 [conference materials].

[2] Kubiczek T.: *Podsadzanie wyrobisk w kopalniach*. „Postęp Techniczny w Górnictwie", z. II, Spółdzielnia Wydawniczo-Oświatowa „Czytelnik", Wrocław 1950, pp. 1–55.

[3] Gisman S.: *Słownik górniczy*. Instytut Węglowy, Katowice 1949.

[4] Jopek F.: *Podsadzanie wyrobisk. Cz. 1: Podsadzka płynna*. Państwowe Wydawnictwa Techniczne, Katowice 1950.

[5] Krupiński B.: *Zasady projektowania kopalń, część I.* 2nd ed., Wydawnictwo „Śląsk", Katowice 1963.

[6] Gonet A., Stryczek S., Winid B.: *Projekt techniczny likwidacji otworów podsadzkowych odwierconych z powierzchni do wyrobisk Kopalni Soli „Wieliczka"*. Fundacja Wiertnictwo – Nafta – Gaz – Nauka i Tradycje, Kraków 2007 [unpublished].

[7] Gonet A., Stryczek S., Brudnik K.: *Technologia likwidacji otworów podsadzkowych w kopalniach soli.* Wiertnictwo, Nafta, Gaz, 25, 2, 2008, pp. 293–298.

[8] Kubański A.: *Technologie uzdatniania terenów dla budownictwa.* Nowoczesne Budownictwo Inżynieryjne, Lipiec–Sierpień, 4, 2008, pp. 68–71.

[9] Gonet A., Stryczek S.: *Iniekcja rurociągowa i otworowa nowoczesnym sposobem zabezpieczania kopalń*. In: *Warsztaty 2001: Zagrożenia naturalne w górnictwie*. Wydawnictwo Instytutu Gospodarki Surowcami Mineralnymi i Energią PAN, Kraków 2001, pp. 319–325 [conference materials].

[10] Gonet A., Stryczek S.: *Podstawy geoinżynierii*. Wydawnictwa AGH, Kraków 2020.

[11] Pilecki Z.: *Uzdatnienie podłoża autostrady A-1 na terenach pogórniczych* płytkiej eksploatacji rud metali. „Studia, Rozprawy, Monografie" nr 184, Wydawnictwo Instytutu Gospodarki Surowcami Mineralnymi i Energią PAN, Kraków 2014.

[12] Toczek P., Wiśniowski R., Złotkowski A., Teper W.: *Hydraulic radial drilling using a rotary hydraulic nozzle aimed at increasing the exploitation of deposits*. Energies, 16, 23, art. 7868, 2023.

[13] Toczek P., Wiśniowski R.: *Enhancing deposit exploitation efficiency utilizing small-diameter radial boreholes via hydraulic drilling nozzles for optimal resource recovery.* Applied Sciences, 14, 9, art. 3552, 2024.

[14] Toczek P., Wiśniowski R., Złotkowski A., Teper W.: *Hydraulic drilling nozzle design and research*. Inventions, 9, 3, art. 51, 2024. http://doi.org/10.3390/inventions9030051.

Journal of Geotechnology and Energy | vol. 41 | no. 4 | 2024 | pp. 27–34

https://doi.org/10.7494/jge.2024.41.4.6764

ARTICLE

MATHEMATICAL MODEL TO ANALYZE THE GEOMETRIC LIMITATIONS OF MECHATRONIC DEVICES MOVING IN CURVED PIPE SECTIONS

Adam Jan Zwierzyński

AGH University of Krakow, Faculty of Drilling, Oil and Gas, Poland
ORCID: 0000-0002-2568-6446
e-mail: zwierzyn@agh.edu.pl

Date of submission:
25.11.2024

Date of acceptance:
26.11.2024

Date of publication:
30.12.2024

https://journals.agh.edu.pl/jge

Abstract: This article presents a method enabling the determination of the minimum radius of pipe bending in which it is possible to move freely a cylinder with defined dimensions. A respective mathematical model has been presented. The below-described method can be useful in the future, while designing mechatronic tools for working in lateral bores starting from a vertical bore, and also while designing inspection robots moving in pipes and pipelines.

Keywords: drilling, radial drilling, pipeline inspection robots, mechatronic downhole assemblies, robotics, mobile robots

1. Introduction

Over the last twenty years, we have observed [1–5] the dynamic development of technologies in the drilling industry enabling the construction of small-profile lateral bores starting from vertical bores. This technology enables low-cost reaming and testing of production layers. It also enables the increased productivity of existing deposits. Methods developed all over the world use the phenomenon of rock hydro-quarrying, where a tool with a specially constructed nozzle is introduced through a deflector, by means of which a lateral borehole is made with the use of a stream of liquid under high pressure.

We have also seen the development of mechatronic subsurface systems in the drilling industry, which enable different kinds of operations when run to the borehole. An example of such devices may be drilling rigs for drilling in a space environment [6]. We can imagine that similar devices will also be available for lateral bores in the future and they could be used for conducting local geophysical analyses, local deposit tests, and many other kinds of operations. In the case of horizontal bores, the section where the trajectory changes is counted in terms of many meters, but with the lateral bores described herein, the change occurs at lengths no bigger than several meters, and frequently at even less than one meter. The geometric dimensions of such mechatronic subsurface systems have to be adapted in such a way that they are able to go through a deflector from a vertical borehole to a lateral borehole and back.

We have also been observing the development of mobile robots for pipe inspection and cleaning. The geometric limitations described above also concern this kind of devices, since they have to be able to freely deal with bends of pipes with a radius frequently smaller than one meter, or even much less.

For these reasons, a method enabling the verification of whether a device modelled with a cylinder shape with the radius r and length H, may go freely through a pipe with a bore with a radius R and a bend radius ρ, has been developed. A mathematical model has been provided for the method under consideration. Its implementation will enable the determination of a given value of parameters r, H, R (and more precisely $a = R - r$) the minimum value of the bend radius ρ, ensuring the free movement of that device.

2. Definition of the scientific problem

The issue described in this article is a problem of running (pushing) a cylinder with the radius r and height H in a curved pipe with an internal radius R, the internal pass-through part of which is first a cylinder, next 1/4 torus, and then a cylinder again. The internal radius (of the borehole) is equal to $r + a$, where “a” is a given clearance value. Minimum pipe bending radiuses (torus radius) ρ_{min}, through which the cylinder of a given size will go through for a specific r value and different “a” and H values, have to be determined.

This problem can be presented mathematically. To this end, it is necessary to define a set describing the geometric limitations of the pipe inside which a cylinder moves. It should be defined against the selected main coordinate system indicated as $O(x_0, y_0, z_0)$. Next, other cross-sectional fields are created in the agreed pipe section, which determine planes perpendicular to the axis of that pipe. It is then checked whether it is possible to find on its area the position of the center of gravity of the cylinder with a specific radius r and height H for each of those cross-sectional fields, so that it is possible to establish the orientation of the said cylinder so that it does not go beyond the pipe area in which it runs. Failure to meet this condition in at least one cross-sectional field of the pipe means that it is impossible to move a cylinder through it with the required geometric dimensions. In order to conduct such analysis, it is necessary to define a set to describe geometric limitations of the cylinder being moved. It should be remembered that the position of the center of gravity of the cylinder may differ, like its orientation, and that is why it is best to describe it in the local coordinate system (related to that cylinder), and subsequently transform it to the $O(x_0, y_0, z_0)$ system, in which the geometric limitations of the pipe are described mathematically. The mathematical model presented in the section below enables mathematical notation of ideas to be described. It is worth remembering that subsequent cutting planes are indexed by the α parameter. Since the value of that parameter is included in the continuous set of real numbers, the number of possible cross-sectional areas of the pipe is indefinite and discretization of this parameter is necessary. In practice, it suffices to conduct the above-described analysis for subsequent cross-sectional areas of the pipe with values of the α parameter changing by an adequately small step so that it is still accurate and corresponds to real conditions.

3. Results

A mathematical model was created using the description employed in robotics to describe manipulators. Figures 1–3 present the coordinate systems, angles, and symbols applied in the mathematical model.

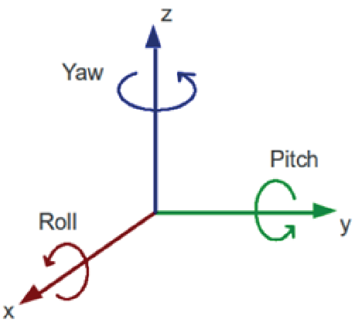

Fig. 1. RPY angles – Roll (ϕ), Pitch (θ), Yaw (ψ)

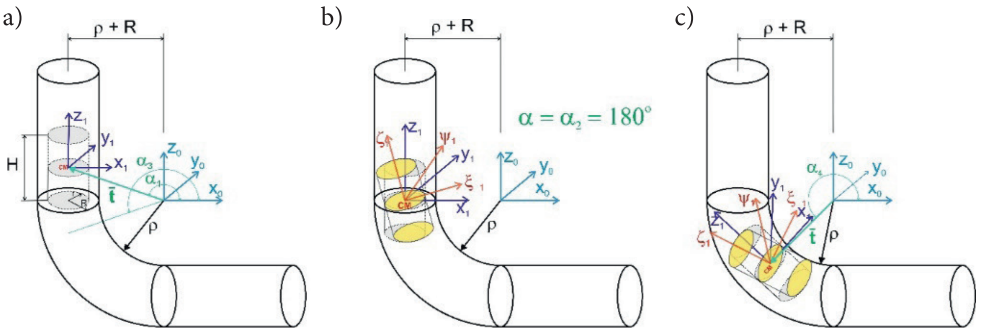

Fig. 2. Conceptual drawings for the mathematical model

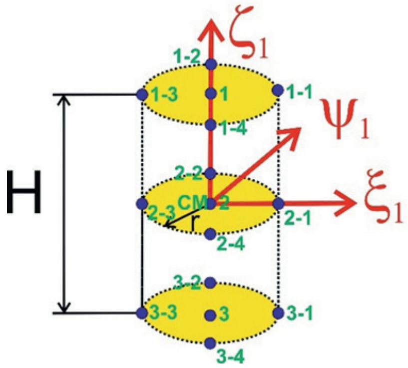

Fig. 3. Cylinder moving through a pipe hole and main points on it

3.1. Mathematical notations used

The following mathematical notations were used in the created mathematical model:

$O(x_0, y_0, z_0)$ – a coordinate system against which the geometric limitations of the pipe through which a cylinder moves are described. This is a basic coordinate system to which coordinates described against other coordinate systems are transformed,

$O(x_1, y_1, z_1)$ – a coordinate system related to the cylinder. The circle being the cross-section of the cylinder through the plane parallel to both its bases and going through the center of gravity, *CM*, is normally set to the axis of the pipe hole through which this cylinder moves,

$O(\xi_1, \psi_1, \zeta_1)$ – a coordinate system related to the cylinder rotated around the center of gravity by the Roll (ϕ) and Pitch (θ) angles,

CM – the center of gravity of the cylinder,

t – the vector connecting the center of the $O(x_0, y_0, z_0)$ system with the center of gravity of the cylinder,

α – the angle between the 0-x_0 axis and the ***t*** vector,

ϕ – the angle of rotation of the cylinder around the 0-x_1 axis (Roll) beginning in the center of gravity, CM, of this cylinder,

$\phi_{\min}$ – the minimum value of the angle of rotation of the cylinder around the 0-x_1 axis (Roll) beginning in the center of gravity, CM, of this cylinder,

$\phi_{\max}$ – the maximum value of the angle of rotation of the cylinder around the 0-x_1 axis (Roll) beginning in the center of gravity, CM, of this cylinder,

$\Delta\phi$ – a change (step) of the angle of rotation of the cylinder around the 0-x_1 axis (Roll) beginning in the center of gravity, CM, of this cylinder,

θ – the angle of rotation of the cylinder around the 0-y_1 axis (Pitch) beginning in the center of gravity, CM, of this cylinder,

$\theta_{\min}$ – the minimum value of the angle of rotation of the cylinder around the 0-y_1 axis (Pitch) beginning in the center of gravity, CM, of this cylinder,

$\theta_{\max}$ – the maximum value of the angle of rotation of the cylinder around the 0-y_1 axis (Pitch) beginning in the center of gravity, CM, of this cylinder,

$\Delta\theta$ – a change (step) of the angle of rotation of the cylinder around the 0-y_1 axis (Pitch) beginning in the center of gravity, CM, of this cylinder

$A1$ – matrix transforming coordinates described in the $O(x_1, y_1, z_1)$ system to coordinates in the $O(x_0, y_0, z_0)$ system,

$A2$ – matrix transforming coordinates described in the $O(\xi_1, \psi_1, \zeta_1)$ system to coordinates in the $O(x_1, y_1, z_1)$ system,

ρ – the bend radius of the pipe,

$\rho_{\min}$ – the minimum bend radius of the pipe,

$\rho_{\max}$ – the maximum bend radius of the pipe,

$\Delta\rho$ – a change in the bend radius of the pipe (step),

r – the radius of the cylinder,

$r_{\min}$ – the minimum radius of the cylinder,

$r_{\max}$ – the maximum radius of the cylinder,

Δr – a change (step) of the cylinder radius,

H – height of the cylinder moving through the pipe,

$H_{\min}$ – the minimum height of the cylinder moving through the hole,

$H_{\max}$ – the maximum height of the cylinder moving through the hole,

ΔH – a change in the height of the cylinder moving through the hole,

R – the radius of the hole in the pipe: $R = r + 2a$,

a – clearance between the cylinder and the internal wall of the pipe hole,

$a_{\min}$ – the minimum clearance between the cylinder and the internal wall,

$a_{\max}$ – the maximum clearance between the cylinder and the internal wall of the pipe hole,

Δa – a change (step) of clearance between the cylinder and the internal wall of the pipe hole.

3.2. Mathematical model

The $O(x_0, y_0, z_0)$ system is a basic coordinate system. In this system, geometric limitations of the pipe (through which the cylinder moves) have been described. The pipe is first a cylinder, then it constitutes 1/4 of a torus and a cylinder again, which has been described in the below formulas (1), (2) and (3), respectively. The sum of S_1, S_2, S_3 sets gives an S set, which represents the whole pipe (4).

$$S_1 = \{(x,y,z): \\ x \le 0 \wedge z \ge 0 \wedge (x + (\rho + R))^2 + y^2 \le R^2 \wedge z \le 2H\} \tag{1}$$

$$S_2 = \{(x,y,z): \\ x \le 0 \wedge z \le 0 \wedge (\sqrt{x^2 + z^2} - (\rho + R))^2 + y^2 \le R^2\} \tag{2}$$

$$S_3 = \{(x,y,z): \\ x \ge 0 \wedge z \le 0 \wedge y^2 + (z + (\rho + R))^2 \le R^2 \wedge x \le 2H\} \tag{3}$$

$$S = \bigcup_{i=1}^{3} S_i = S_1 \cup S_2 \cup S_3 \tag{4}$$

S_1, S_2, S_3 sets are sets of points in the $\boldsymbol{R}^3$ space of real numbers. Those sets depend on parameters ρ, R, $\boldsymbol{H}$, which signify the bend radius of the pipe, the radius of the pipe hole and cylinder height, respectively. The $2H$ value was introduced in order to limit S_1 and S_3 sets. The adopted limitation assumes arbitrarily that the height of cylinders represented by S_1 and S_3 sets is twice as big as the height of the cylinder moving through the pipe. There is dependence between the radius of the hole in the pipe and the radius of the cylinder and clearance (5).

$$\boldsymbol{R} = \boldsymbol{r} + 2\boldsymbol{a} \tag{5}$$

The cylinde, which moves through a curved pipe described with the S set is described against the $O(\xi_1, \psi_1, \zeta_1)$ system. As mentioned in Item 2, the method proposed in this article assumes that for subsequent cross-sections of the pipe included in planes perpendicular to the pipe axis it is checked whether there is such a position of the center of gravity of the cylinder (located within the area of a given cross-section) and its orientation which ensures that the cylinder is included in the pipe. From the mathematical point of view, such an operation boils down to checking whether for subsequent centers of gravity of the cylinder, located within the above-mentioned cross-section, there is at least one set of points (x, y, z) which describes this cylinder (one cylinder location), which is included in the S set. If this condition is not met, it means that the cylinder projects beyond the pipe and it is impossible to move it. Other section planes are indexed by the α parameter, and possible centers of gravity of the cylinder within the cross-section area are determined by $((x_1,CM)_i, (y_1,CM)_j)$. The condition described is expressed here by the following formula (6) and (7).

$$C \subset S \tag{6}$$

$$C_{\alpha,((x_{1,CM})_i,(y_{1,CM})_j)} = \Big\{(\xi_1,\psi_1,\zeta_1): \left(\zeta_1 \geq -\frac{H}{2}\right) \wedge \left(\zeta_1 \leq \frac{H}{2}\right) \wedge ((\xi_1)^2+(\psi_1)^2 \leq r^2)\Big\} \tag{7}$$

The formula (7) is very general. In the designation of this set *C*, and more precisely in the index, there is information that the center of gravity of the cylinder described with the *C* set is in the point at $((x_1, CM)_i, (y_1, CM)_j)$, located on the cutting plane described with the α parameter. Those symbols will be explained below. Checking of the condition (6) is difficult when applying a general notation of *C* sets. However, one may use the property of the solid, which a cylinder is, that it is a convex set. For a given set to be convex, each section made up by two points being set elements has to be included in this set. Owing to this property of the *C* set, if an adequately dense grid is defined on its edge, all of the points will belong to the *S* set, it may be assumed that the *C* set is included in the *S* set. Formulas from (8) to (11) define a set of subsequent points in the grid on the edge of the cylinder being the set described with the formula (7).

$$\begin{gathered}\partial(C_{\alpha,((x_{1,CM})_i,(y_{1,CM})_j)})_1 = \{((\xi_1)_{klm},(\psi_1)_{klm},(\zeta_1)_{klm}): k = 0, \ldots,\\ [2\pi r/0.5];\ l = 0;\ m = 0, \ldots, (r/0.5);\ \Delta\varphi = 0.5/r;\\ (\xi_1)_{klm} = 0.5 \cdot m \cdot \cos(k \cdot \Delta\varphi);\ (\psi_1)_{klm} = 0.5 \cdot m \cdot \sin(k \cdot \Delta\varphi);\\ (\zeta_1)_{klm} = -(H/2) + 0.5 \cdot l\}\end{gathered} \tag{8}$$

$$\begin{gathered}\partial(C_{\alpha,((x_{1,CM})_i,(y_{1,CM})_j)})_2 = \{((\xi_1)_{klm},(\psi_1)_{klm},(\zeta_1)_{klm}): k = 0, \ldots,\\ [2\pi r/0.5];\ l = 1; \ldots, ((H/0.5) - 1);\ m = (r/0.5);\\ \Delta\varphi = 0.5/r;\ (\xi_1)_{klm} = 0.5 \cdot m \cdot \cos(k \cdot \Delta\varphi);\\ (\psi_1)_{klm} = 0.5 \cdot m \cdot \sin(k \cdot \Delta\varphi);\ (\zeta_1)_{klm} = -(H/2) + 0.5 \cdot l\}\end{gathered} \tag{9}$$

$$\begin{gathered}\partial(C_{\alpha,((x_{1,CM})_i,(y_{1,CM})_j)})_3 = \{((\xi_1)_{klm},(\psi_1)_{klm},(\zeta_1)_{klm}): k = 0, \ldots,\\ [2\pi r/0.5];\ l = (H/0.5);\ m = 0, \ldots, (r/0.5);\ \Delta\varphi = 0.5/r;\\ (\xi_1)_{klm} = 0.5 \cdot m \cdot \cos(k \cdot \Delta\varphi);\ (\psi_1)_{klm} = 0.5 \cdot m \cdot \sin(k \cdot \Delta\varphi);\\ (\zeta_1)_{klm} = -(H/2) + 0.5 \cdot l\}\end{gathered} \tag{10}$$

$$\partial(C_{\alpha,((x_{1,CM})_i,(y_{1,CM})_j)}) = \bigcup_{n=1}^{3} \partial(C_{\alpha,((x_{1,CM})_i,(y_{1,CM})_j)})_n \tag{11}$$

Although formulas from (8) to (11) are long, they are not complicated. This is a notation enabling recording of all points which might belong to the ∂*C* set, being the edge of the *C* set, in a general way. ∂C_1, ∂C_2, ∂C_3 sets are sets of the above-mentioned grid located on the lower base of the cylinder, the side wall of the cylinder and on the upper base of the cylinder, respectively. The sum of those sets (11) determines the ∂*C* set, being a set of grid points located on the edge of the *C* set. The *k* index relates to the angle growth. The precision of the angle dimension is such that the corresponding length of the arch with the radius equal to the radius of the cylinder *r* is 0.5 mm. Thus, the *k* index has to change from zero to the value of the ceiling function from the expression: $2pr/0.5$. The expression $2pr/0.5$, in a general case, is not the total multiple of 0.5, so it was necessary to apply the ceiling function in order to make a full circle. It causes adding some points, as the ceiling function rounds up a real number to the nearest higher integer, but it does not cause any problems with calculations or any errors. The l index relates to the z_1 coordinate of points, which may change from $-H/2$ to $H/2$. Since the precision of the linear dimension is 0.5 mm, the l index may change from 0 to $H/0.5$. The m index relates to the radius growth. It may change from 0 to the value equal to *r* (cylinder radius). Since the precision of the linear dimension is 0.5 mm, the m index may change from 0 to $r/0.5$.

It should be noted that the ∂C_1, ∂C_2, ∂C_3 sets only depend on two parameters: cylinder radius, *r* and cylinder height, *H*. The $O(x_1, y_1, z_1)$ system is permanently related to the cylinder and hooked in the point which is its center of gravity. A set of grid points for the ∂*C* edge of the cylinder with established dimensions of *r* and *H* will be the same towards the $O(x_1, y_1, z_1)$ system, regardless of whether the cylinder will be tilted (Roll, Pitch) or moved towards the $O(x_1, y_1, z_1)$ system. That is why, in the implementing program presenting the model it will be enough to set coordinates of all grid points on the edge of the cylinder only once (i.e. to determine the ∂*C* set), and next, in subsequent steps, to transform them to the $O(x_1, y_1, z_1)$ system and further to the $O(x_0, y_0, z_0)$ system.

In planes of subsequent pipe cross-sections described by the α parameter, circles with the radius expressed by the formula (12) are determined. The center of those circles is always the intersection of the center line of the pipe with a given cutting plane. This point is the point where the beginning of the $O(x_1, y_1, z_1)$ coordinate system is hooked. If the center of the cylinder is within the area of this circle, angles of the cylinder rotation (roll, pitch) are zero, the area being the cross-section of this cylinder (circle) is included in the area being the cross-section of the pipe. It may turn out that for a given bend radius of the pipe ρ, if the center of gravity of the cylinder located in the cutting plane of the pipe moves from the center of the O_α circle to a different point included in this circle, it will be possible to find such cylinder orientation that it will be included in the pipe (which might not be possible if the cylinder's center of gravity overlaps with the center of the circle, O_α). Obviously, it is not possible to check each point of the O_α circle, as it contains infinitely many points. Discretization of that set is necessary. To this end, a rectangular grid of points located in the cutting plane, described against the $O(x_1,y_1,z_1)$ system, whose $Dx_1 = Dy_1 = 0.5$ mm, is created. All points of this grid, which belong to the O_α circle, create a discrete set, $O_{\alpha,dis}$, described with the equation (13). Vectors of translation of the center of gravity of the cylinder into subsequent points of the $O_{\alpha,dis}$ set have been described with the formula (14).

$$R - r = r + a - r = a \tag{12}$$

$$\begin{gathered} O_{\alpha,dis} = \{((x_1)_i, (y_1)_j) : i, j = 0, \ldots, (2 \cdot (a/(0.5)); \\ (x_1)_i = -a + 0.5 \cdot i;\ (y_1)_j = -a + 0.5 \cdot j; \\ ((x_1)_i)^2 + ((y_1)_j)^2 \leq a^2\} \end{gathered} \tag{13}$$

$$\vec{k}_{i,j} = [(x_1)_i, (y_1)_j];\ \ ((x_1)_i, (y_1)_j\ ) \in O_\alpha \tag{14}$$

As mentioned above, a set of points of the grid at the edge of the cylinder, ∂C, is described against the $O(x_1, y_1, z_1)$ system, which is permanently related to the cylinder and hooked in the point which is its center of gravity. It is necessary to describe those points against the $O(x_0, y_0, z_0)$ system. However, first transformation of coordinates of those points to the $O(x_1, y_1, z_1)$ system has to be done. Transformation from the $O(x_1, y_1, z_1)$ system to the $O(x_1, y_1, z_1)$ system requires three steps:

$$T(\vec{k}_{i,j}) \rightarrow R(x_1, \phi) \rightarrow R(y_2, \theta) \tag{15}$$

The first step is translation by the vector k given in the formula (14), the second is rotation around the x'_1 axis by the ϕ angle, the third one is rotation around the y''_1 axis by the θ angle. In order to perform inverse transformation, it is necessary to find inverse matrixes of the described transformations. A transformation matrix has the form given with the equation (17).

$$\begin{bmatrix} x_1 \\ y_1 \\ z_1 \\ 1 \end{bmatrix} = A_2 \begin{bmatrix} \xi_1 \\ \psi_1 \\ \zeta_1 \\ 1 \end{bmatrix} \tag{16}$$

$$\begin{gathered} A_2 = \begin{bmatrix} \cos\theta & 0 & \sin\theta & 0 \\ 0 & 1 & 0 & 0 \\ -\sin\theta & 0 & \cos\theta & 0 \\ 0 & 0 & 0 & 1 \end{bmatrix} \\ \cdot \begin{bmatrix} 1 & 0 & 0 & 0 \\ 0 & \cos\phi & -\sin\phi & 0 \\ 0 & \sin\phi & \cos\phi & 0 \\ 0 & 0 & 0 & 1 \end{bmatrix} \cdot \begin{bmatrix} 1 & 0 & 0 & (x_1)_i \\ 0 & 1 & 0 & (y_1)_j \\ 0 & 0 & 1 & 0 \\ 0 & 0 & 0 & 1 \end{bmatrix} \end{gathered} \tag{17}$$

Next, the transformation has to take place from the $O(x_1, y_1, z_1)$ system to the $O(x_0, y_0, z_0)$ system. Figure 2a presents the initial position of the cylinder. Its lower base is on the Ox_0y_0 plane, the center of gravity of the cylinder is on the center line of the pipe. The location of the center of gravity of the cylinder, *CM*, located on the center line of the pipe against the $O(x_0, y_0, z_0)$ system determines the radial vector ***t***. The angle between the Ox_0 axis and the radial vector ***t*** is determined by α. As mentioned before, this angle parameterizes (or numbers) subsequent cutting planes of the pipe, which are normal to the axis of this pipe. For the situation presented in Figure 2a the α parameter is given with the formula (18)

$$\alpha = \alpha_1 = \pi - \mathrm{arctg}\left(\frac{H/2}{\rho + R}\right) \tag{18}$$

The location of the cylinder, which $\alpha = a_1$ corresponds to, is the initial location from which checking whether the cylinder moving through the pipe with a given value of its bend radius ρ (of that pipe) is included in this pipe begins. Importantly, it is not necessary to check this condition along the whole pipe length. It is enough to do it only:

1. At the section of the pipe in which it leaves the part of the pipe described with the S_1 set and enters the part described with the S_2 set (torus). For $\alpha = \alpha_2 = \pi$ there is a change in the pipe curvature. The problem is to determine the α_3 angle for which the cylinder has left the S_1 set and may be only in the S_2 set. It was assumed that it is an angle for which the distance of the projection on the bottom (negative) part of the Oz_0 axis of the point corresponding to this angle and located on the circle with the radius $\rho + R$ (negative coordinate z_0) from the center of the $O(x_0, y_0, z_0)$ coordinate system is higher than or equal to $3 \cdot H$.

   If the value of the bend radius of the pipe is so small that the said value is smaller than $3 \cdot H$, in such case, the inclusion of the cylinder in the pipe at the section from $\alpha = \alpha_1$ to $\alpha = 3\pi/2$ occurs;
2. For $\alpha = \alpha_4 = \pi + \pi/4$ (torus center). Due to the torus rotational symmetry, if the cylinder with the center of gravity located within the circle O_α, being in the cutting plane corresponding to the desired value of the angle $\alpha = \alpha_4$ may be included in the pipe, then for other values of the α angle (higher than a_3 and smaller than $(3\pi/2 - (a_3 - \pi))$) it will be also possible.

In order to move from the $O(x_0, y_0, z_0)$ system to the $O(x_1, y_1, z_1)$ system, it is necessary to perform a string of operations, as given in the formula (19). The first one is translation by vector $\boldsymbol{t}_\alpha$, the second one is a rotation around the y'_0 axis by the α angle. However, the orientation of the $O(x_1, y_1, z_1)$ system and the vector of the $\boldsymbol{t}_\alpha$ translation depend on the value of the α angle and in what range of values the current value of that angle is. It has been described in detail in Table 1. For each case, transformation matrix $\boldsymbol{A}_1$ was determined (formulas (21)–(23)), transforming coordinates in the $O(x_1, y_1, z_1)$ system to coordinates in the $O(x_0, y_0, z_0)$ system, in accordance with the formula (20).

Table 1. Ranges of the α angle and corresponding cutting planes of the pipe in which Oα circles and $O(x_1, y_1, z_1)$ coordinate systems are determined

Range of α angle	Cutting plane	$O(x_1, y_1, z_1)$ coordinate system	Vector of translation ***t***/Notes
$\alpha\in[\alpha_1;\alpha_2=p]$ Center of gravity of the cylinder, *CM*, in the S_1 set Angle α is set	Parallel to the Ox_0y_0 plane	Orientation identical as of the $O(x_0, y_0, z_0)$ system Beginning of the system is moved against the beginning of the $O(x_0, y_0, z_0)$ system by vector ***t***	$\vec{t}=\left[-(\rho+R);\ 0;\ H/2-0.5m\right]$ $m=0,\cdots,\dfrac{H/2}{0.5}$ $\alpha=\pi-arctg\left(\dfrac{H/2-0.5m}{\rho+R}\right)$
$\alpha\in(\pi;3\pi/2]$ Center of gravity of the cylinder, *CM*, in the S_2 set	Plane overlapped with the Ox_0y_0 plane, rotated by the angle α	System rotated by the angle (α – π) around the y_0 axis of the $O(x_0, y_0, z_0)$ system Beginning of the system is moved against the beginning of the $O(x_0, y_0, z_0)$ system by vector ***t***	$\vec{t}=\left[(\rho+R)\cos\alpha;\ 0;\ (\rho+R)\sin\alpha\right]$ The step by which angle α should be changed is an angle for which the arch length is 0.5 mm $\Delta\alpha=\dfrac{0.5}{\rho+R}$
α > 3π/**2** Center of gravity of the cylinder, *CM*, in the S_3 set	Parallel to the Oy_0z_0 plane	System rotated by the π/2 angle around the y_0 axis of the $O(x_0, y_0, z_0)$ system Beginning of the system is moved against the beginning of the $O(x_0, y_0, z_0)$ system by vector ***t***	$\vec{t}=\left[0.5m;\ 0;\ -(\rho+R)\right]$ $m=1,\ \cdots,\ \dfrac{H/2}{0.5}$ In this part of the pipe it is not checked, whether the cylinder being moved will be included inside the pipe, because due to the symmetry (of the pipe), it corresponds geometrically to the first range of the α angle Minimum value of the parameter m equal to one results from α > 3π/2

$$T(\vec{t}_\alpha)\rightarrow R(y_0,\alpha) \tag{19}$$

$$\begin{bmatrix} x_0 \\ y_0 \\ z_0 \\ 1 \end{bmatrix} = A_1 \begin{bmatrix} x_1 \\ y_1 \\ z_1 \\ 1 \end{bmatrix} \tag{20}$$

$$\alpha\in\left[\alpha_1;\ (\alpha_2=\pi)\right]\Rightarrow A_1=\begin{bmatrix} 1 & 0 & 0 & -(\rho+R) \\ 0 & 1 & 0 & 0 \\ 0 & 0 & 1 & H/2-0{,}5m \\ 0 & 0 & 0 & 1 \end{bmatrix};\ m=0,\ \cdots,\ \frac{H/2}{0.5\ \text{mm}} \tag{21}$$

$$\alpha\in\left[\alpha_1;(\alpha_2=\pi)\right]\Rightarrow A_1=\begin{bmatrix} \cos(\alpha-\pi) & 0 & \sin(\alpha-\pi) & 0 \\ 0 & 1 & 0 & 0 \\ -\sin(\alpha-\pi) & 0 & \cos(\alpha-\pi) & 0 \\ 0 & 0 & 0 & 1 \end{bmatrix}\cdot\begin{bmatrix} 1 & 0 & 0 & (\rho+R)\cos\alpha \\ 0 & 1 & 0 & 0 \\ 0 & 0 & 1 & (\rho+R)\sin\alpha \\ 0 & 0 & 0 & 1 \end{bmatrix} \tag{22}$$

$$\alpha > \frac{3\pi}{2} \cdot A_1 = \begin{bmatrix} \cos(\pi/2) & 0 & \sin(\pi/2) & 0 \\ 0 & 1 & 0 & 0 \\ -\sin(\pi/2) & 0 & \cos(\pi/2) & 0 \\ 0 & 0 & 0 & 1 \end{bmatrix} \cdot \begin{bmatrix} 1 & 0 & 0 & 0.5m \\ 0 & 1 & 0 & 0 \\ 0 & 0 & 1 & -(\rho + R) \\ 0 & 0 & 0 & 1 \end{bmatrix}; \; m = 1, \; \cdots, \; \frac{H/2}{0.5 \text{ mm}} \tag{23}$$

If transformations described with $\boldsymbol{A_1}$ and $\boldsymbol{A_2}$ matrixes are now made, full transformation is acquired, which enables moving from the $O(x_1, y_1, z_1)$ system to the $O(x_0, y_0, z_0)$ system, in which geometric limitations of the pipe (S set) are described by formula (24):

$$\begin{bmatrix} x_0 \\ y_0 \\ z_0 \\ 1 \end{bmatrix} = A_1 \cdot A_2 \cdot \begin{bmatrix} \xi_1 \\ \psi_1 \\ \zeta_1 \\ 1 \end{bmatrix} \tag{24}$$

Now, with regard to the subsequent values of the α angle (for which it is checked whether the cylinder is included in the pipe), it should be checked whether the points belonging to ∂C_α being the edge of the cylinder, whose center of gravity belongs to some of the points of the $O_{\alpha,dis}$ set (described with the formula (4–14)), are included in the S set. We now search for the smallest value of the bend radius ρ, for which the described condition is satisfied for all the examined values of the α angle.

4. Conclusions

This article presents an original model to solve the problem of running the cylinder in a bent pipe. This model and method may be implemented in the form of a computer program which will enable to determine tables informing, for specific geometrical dimensions: r (radius) and H (height) of the cylinder, clearance a, what should be the minimum bend radius of a rigid pipe so that it is possible to move this cylinder through it. This problem is particularly important in the context of designing miniature mechatronic devices to operate in lateral boreholes going out from the main vertical borehole. It is also significant for mobile robotics in terms of designing robots moving inside pipes.

The proposal contained in the article ensures a high precision of calculation by adopting a suitably dense grid of points creating the edge of the cylinder. The proposed precision of the linear dimension is 0.5 mm, whereas the precision of the angle dimension is the precision corresponding to an angle for which an arch with the radius equal to the cylinder radius r has the length equal to 0.5 mm. In the opinion of the author, such detailed analysis will enable valuable numeric analysis. However, it relates to high computational complexity, which requires the application of a supercomputer for this purpose and using many of its nodes. To this end, it will be necessary to implement the model and method presented here in the form of a computational program using the so-called parallel computing. Works on the preparation of such a program are ongoing.

Funding: This research received no external funding.

Conflicts of Interest: The author of this paper declares no conflicts of interest.

References

[1] Abdel-Ghany M.A., Siso S., Hassan A.M., Pierpaolo P., Roberto Ch.: *New technology application, radial drilling petrobel, first well in Egypt*. In: *10th Offshore Mediterranean Conference and Exhibition,* Paper No. OMC-2011-163, Ravenna 2011.

[2] Dickinson W., Dickinson R., Herrera A., Dykstra H., Nees J.: *Slim hole multiple radials drilled with coiled tubing*. In: *SPE Latin America Petroleum Engineering Conference*, Paper No. SPE-23639-MS, Caracas 1992. https://doi.org/10.2118/23639-MS.

[3] Bruni M., Biasotti H., Salomone G.: *Radial Drilling in Argentina*. In: *Latin American & Caribbean Petroleum Engineering Conference*, Buenos Aires 2017, Paper No. SPE-107382-MS. https://doi.org/10.2118/107382-MS.

[4] Balch R., Ruan T., Savage M., Harvard J.: *Field Testing and Validation of a Mechanical Alternative to Radial Jet Drilling for Improving Recovery in Mature Oil Wells*. In: *SPE Western Regional Meeting*, Anchorage 2016, Paper No. SPE-180410-MS. https://doi.org/10.2118/180410-MS.

[5] Hossain M.E., Al-Majed A.A.: *Fundamentals of Sustainable Drilling Engineering*. Scrivener Publishing LLC, Wiley, 2015.

[6] Bar-Cohen Y., Zacny K.: *Drilling in Extreme Environments: Penetration and Sampling on Earth and other Planets*. Wiley-VCH Verlag GmbH & Co. KGaA 2009.

Journal of Geotechnology and Energy | vol. 41 | no. 4 | 2024 | pp. 35–42

https://doi.org/10.7494/jge.2024.41.4.6741

ARTICLE

SECONDARY ARSENATES FROM THE ĽUBIETOVÁ-SVÄTODUŠNÁ COPPER DEPOSIT IN SLOVAKIA

Urszula Solecka

University of Agriculture in Krakow, Faculty of Environmental Engineering and Geodesy,
Department of Rural Building, Poland
ORCID: 0000-0001-9149-6184
e-mail: u.solecka@urk.edu.pl

Date of submission:
19.11.2024

Date of acceptance:
24.11.2024

Date of publication:
30.12.2024

https://journals.agh.edu.pl/jge

Abstract: In the vicinity of Lubietová in the Banská Bystrica region in Slovakia, copper was mined in three deposits: Podlipa, Svätodušná, and Kolba. The study concerns the association of secondary arsenates of the Lubietová-Svätodušná copper deposit. The Lubietová-Svätodušná deposit contains a large number of secondary minerals, formed as a result of weathering in the hypergene zone. Among them, copper arsenates are the most important, due to the rare occurrence of some of them. Four secondary arsenates have been characterized: chalcophyllite, euchroite, olivenite and pharmacosiderite. The minerals were identified using X-ray diffraction (XRD), whereas observations under a scanning electron microscope (SEM) and chemical analysis (EDS) showed that some of them are heterogeneous, contain different substitutions, and show significant variability in the content of individual elements within single specimens.

Keywords: secondary minerals; arsenates; euchroite; Ľubietová-Svätodušná, copper

1. Introduction

Arsenic is a highly toxic element. It occurs in nature in various forms and at various oxidation states. Its toxicity and mobility in the environment depend on both its chemical form and the form of occurrence [1]. Heaps rich in arsenic are particularly dangerous to the natural environment. This element can be transported from them by rainwater, running water and industrial sewage over very long distances. Usually, the sources of arsenic are sulfur salts and metal arsenides such as arsenopyrite, cobaltite, nickelite; arsenic sulfides, e.g. realgar and arsenic oxides [2]. An example of such a dump is the heap created because of mining the copper deposit Ľubietová-Svätodušná in the Slovak Republic. In addition to primary minerals, secondary minerals also occur there, mainly arsenates, although sulphates and carbonates also appear. This heap is the place where euchroite $Cu_2(AsO_4)(OH) \cdot 3H_2O$ was first found and described [3] vide [4].

Despite many studies, descriptions and characteristics of these arsenates [4–16] and continuous interest in this topic, the conditions and processes that had to occur in the Ľubietová-Svätodušná deposit heap for these minerals to form and co-occur together have not yet been fully described [17]. In this work, the arsenates occurring in the heap were characterized in order to use them for further research on the conditions of formation of such secondary arsenates' associations.

2. Location

The village and commune of Ľubietová is located in the central part of the Slovak Republic. It is located 15 km east of Banská Bystrica [4]. Administratively, it is located in the Banská Bystrica district in the Banská Bystrica region. The Ľubietová-Svätodušná deposit is located about 5 km from the center of the village [18], in the upper part of the Peklo Valley, on the southwestern slope of Kolba (1 162.1 m MSL) (Fig. 1).

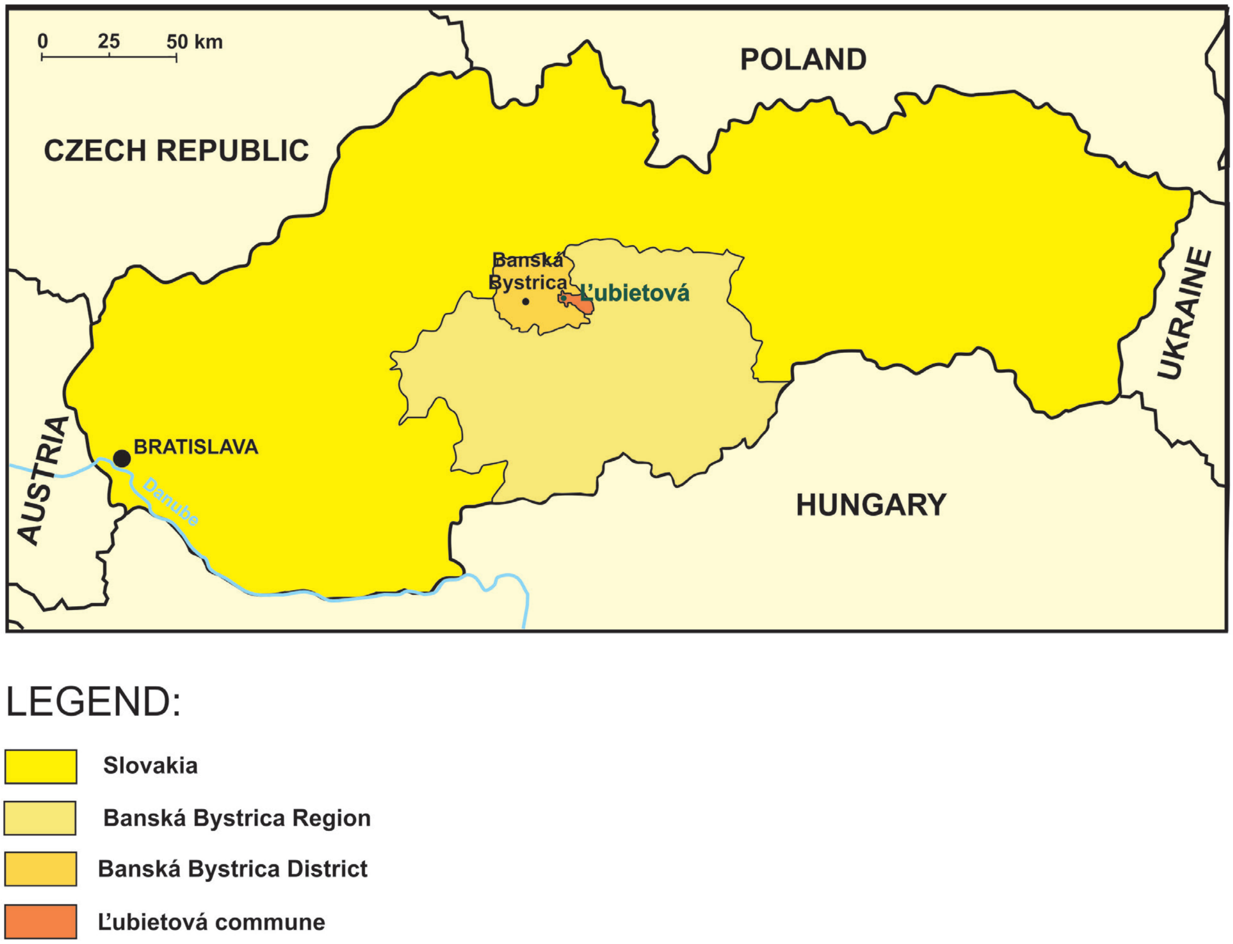

Fig. 1. Location of Ľubietová in Slovakia

3. Geology of research area

The studied area is located on the border of Mesozoic and late Paleozoic formations and crystalline complexes of Fatricum and northern Veporicum, as well as Neogene and Quaternary volcanites (Fig. 2). Fatricum represents a system of nappes lying close to the surface, covering Tatricum. It consists of Permian and Mesozoic sequences, with local relics of crystalline basement. Veporicum also consists of a crystalline basement and late Paleozoic and Mesozoic cover.

The cover formations are divided into northern and southern. The northern one is mainly composed of Permian clastic sediments and Mesozoic sediments. The southern one is composed of Upper Carboniferous, Permian and Triassic sediments. The crystalline basement has a complicated internal structure. There are both granitoid units with highly metamorphosed rocks and units of weakly metamorphosed Early Paleozoic rocks. Volcanites are associated with andesitic volcanism. In central Slovakia, it lasted from the early Badenian to the Pannonian. It was preceded by acidic, rhyodacitic-rhyolitic volcanism. The last stage of volcanic activity in Slovakia was alkaline basaltic volcanism (Pannonian, Pliocene and Pleistocene) [19].

The geological substratum of the studied area is very diverse. The Hron Valley is filled with sandy gravels [21]. In the south, the area is built of neogenous, volcanic rocks of the Poľana Massif, such as pyroclasts (tuffs and tuffites) with a composition of pyroxene andesites, lying on rhyodacitic tuffs and pyroxene andesites. The tuffs and andesites cover the Paleozoic rocks of the Ľubietová crystalline rock (Veporicum). The crystalline rock is composed of gneisses, schists, migmatites, amphibolites and Vepor granitoids. The crystalline rock is covered by Permian sediments such as variegated schists, arkosic and greywacke sandstones and quartz porphyries. The Permian rocks are covered by layers of quartzites, Lower Triassic schists, and Middle and Upper Triassic dolomites. They are considered to be a sedimentary series belonging to the Veporicum. In the western part of the area, Neogene sediments (sands, sandstones and gravels) appear [4].

The Ľubietová deposit is a hydrothermal-vein copper deposit and it is located in the Permian formations of the Ľubietová ridge [5]. This deposit is epigenetic, Upper Cretaceous and is associated with the Alpine orogeny. Genetically, it is related to the tectonic-metamorphic and tectonic-magmatic processes of that period [22], see [4]. The greater part of the Ľubietová deposit is associated with arkosic rocks.

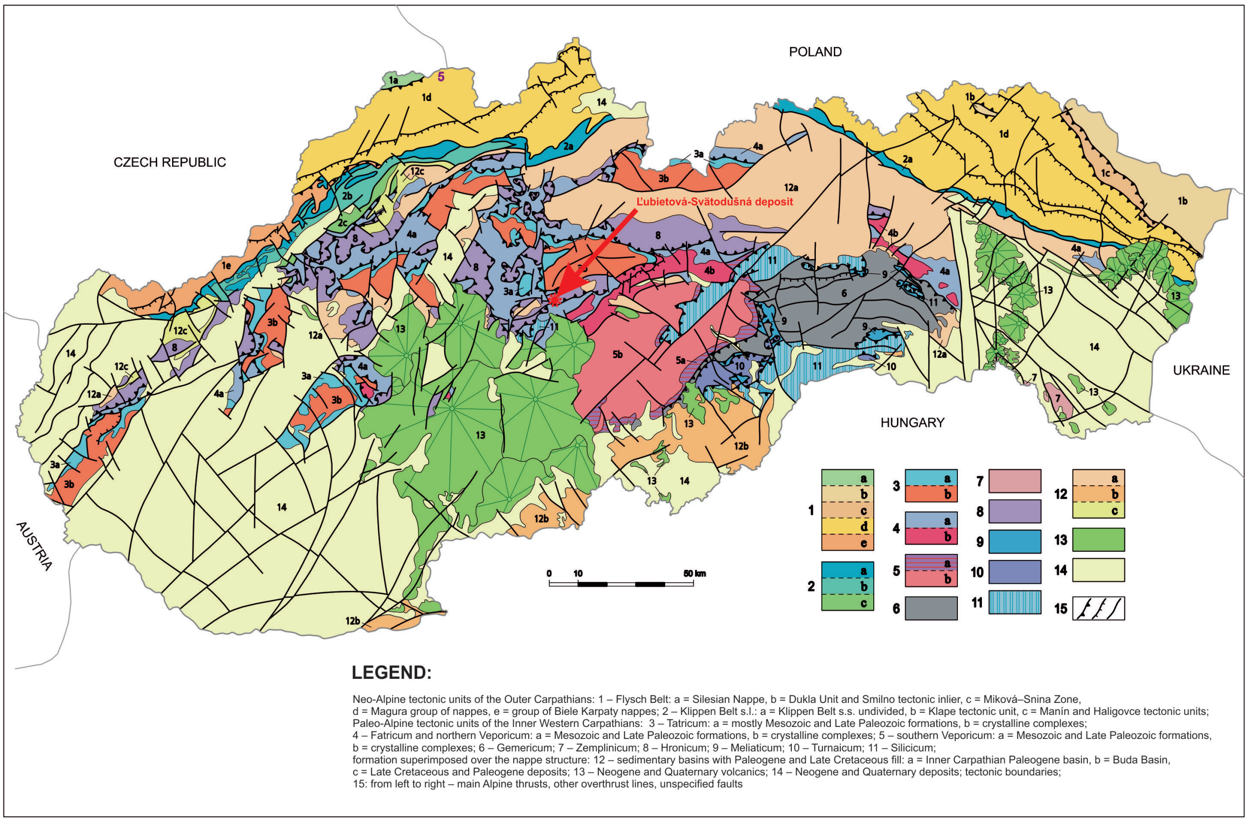

LEGEND:

Neo-Alpine tectonic units of the Outer Carpathians: 1 – Flysch Belt: a = Silesian Nappe, b = Dukla Unit and Smilno tectonic inlier, c = Miková–Snina Zone, d = Magura group of nappes, e = group of Biele Karpaty nappes; 2 – Klippen Belt s.l.: a = Klippen Belt s.s. undivided, b = Klape tectonic unit, c = Manín and Haligovce tectonic units;
Paleo-Alpine tectonic units of the Inner Western Carpathians: 3 – Tatricum: a = mostly Mesozoic and Late Paleozoic formations, b = crystalline complexes;
4 – Fatricum and northern Veporicum: a = Mesozoic and Late Paleozoic formations, b = crystalline complexes; 5 – southern Veporicum: a = Mesozoic and Late Paleozoic formations, b = crystalline complexes; 6 – Gemericum; 7 – Zemplinicum; 8 – Hronicum; 9 – Meliaticum; 10 – Turnaicum; 11 – Silicicum;
formation superimposed over the nappe structure: 12 – sedimentary basins with Paleogene and Late Cretaceous fill: a = Inner Carpathian Paleogene basin, b = Buda Basin, c = Late Cretaceous and Paleogene deposits; 13 – Neogene and Quaternary volcanics; 14 – Neogene and Quaternary deposits; tectonic boundaries;
15: from left to right – main Alpine thrusts, other overthrust lines, unspecified faults

Fig. 2. Location of the Ľubietová-Svätodušná deposit at the simplified geological map of Slovakia (after [19], according to the General geological map of the Slovak Republic 1:200,000 [20])

Currently, the underground parts of the deposit are almost inaccessible and material for research was collected from numerous dumps. The largest spoil heaps are located above the Podlipa settlement and in the Peklo Valley (the Ľubietová-Svätodušná deposit, the Kolba deposit) [5].

In the Ľubietová-Svätodušná deposit, mineralization occurs mainly in quartz or quartz-carbonate veins. The primary minerals are [4, 5, 11]:

- ankerite $Ca(Fe^{2+},Mg)[CO_3]_2$,
- arsenopyrite FeAsS,
- chalcopyrite $CuFeS_2$,
- cobaltite CoAsS,
- Fe-bearing magnesite $(Mg,Fe)CO_3$,
- gersdorffite NiAsS, tennantite $Cu_6[Cu_4(Fe,Ag,Zn)_2]As_4S_{13}$.

Secondary minerals include [4, 5, 11]:

- annabergite $Ni_3(AsO_4)_2 \cdot 8H_2O$,
- azurite $Cu_3(CO_3)_2(OH)_2$,
- brochantite $Cu_4(SO_4)(OH)_6$,
- chalcophyllite $Cu_{18}Al_2(AsO_4)_4(SO_4)_3(OH)_{24} \cdot 36H_2O$,
- clinoclase $Cu_3(AsO_4)(OH)_3$,
- erythrite $Co_3(AsO_4)_2 \cdot 8H_2O$,
- euchroite $Cu_2(AsO_4)(OH) \cdot 3H_2O$,
- malachite $Cu_2(CO_3)(OH)_2$,
- pharmacosiderite $KFe^{3+}{}_4(AsO_4)_3(OH)_4 \cdot 6\text{-}7H_2O$,
- olivenite $Cu_2(AsO_4)(OH)$,
- scorodite $Fe^{3+}AsO_4 \cdot 2H_2O$,
- strashimirite $Cu_8(AsO_4)_4(OH)_4 \cdot 5H_2O$,
- tyrolite $Ca_2Cu_9(AsO_4)_4(CO_3)(OH)_8 \cdot 11H_2O$.

4. Materials and methods

4.1. Sampling in the Ľubietová-Svätodušná deposit

Samples for the study were taken from the surface and subsurface layers of the spoil heap created during the exploitation of the Ľubietová-Svätodušná deposit. The spoil heap is located in a forest at the end of the Peklo valley. It is several hundred meters long and several meters wide. The largest amount of secondary minerals is located in the lower parts of the heap and at its eastern and western ends. Samples were taken from places with the highest concentration of secondary minerals. The selection of the research material was guided by the presence of macroscopically visible (usually green) secondary minerals in the rocks.

4.2. Characteristics of natural samples

Studies were carried out in the laboratories of the Department of Mineralogy, Petrography and Geochemistry, the Department of Economic and Mining Geology (Laboratory of Ore Microscopy) and the Faculty Laboratory of the Faculty of Geology, Geophysics and Environmental Protection of AGH University of Science and Technology, as well as in the Laboratory of Scanning Microscopy of the Geological Institute of the Slovak Academy of Sciences in Banská Bystrica.

Macroscopic observations of the collected secondary minerals were performed using an Olympus SZX-9 stereoscopic microscope with an Olympus DP-12 digital camera controlled by the Analysis program. They were then separated and ground in an agate mortar and identified using X-ray diffractometry (XRD). A Philips PW 3020 X'Pert-APD diffractometer equipped with a graphite reflection monochromator was used for the study. Qualitative identification was performed using the XRAYAN computer program. The crystal morphology of natural secondary minerals from the Ľubietová-Svätodušná deposit was analyzed by scanning electron microscopy (SEM). For this purpose, a JEOL JSM 6390 LV microscope was used together with an energy dispersive spectrometer (EDS).

5. Results

Eleven secondary mineral phases differing in color and formation were collected from the heap, including five identified as arsenates (samples LS1, LS2, LS3, LS4, LS5).

In sample LS1, the studied mineral has an emerald color and forms crystals with a tabular shape. The plates are 0.5 mm to 4 mm in size but are 2 mm on average. Some plates are hexagonal in shape. The mineral under study has a strong pearl luster, a pale green streak, and excellent, unidirectional cleavage (Fig. 3a). It is brittle and soft. The crystals occur on quartz arkose. Based on the results of XRD analysis, the emerald plates from sample LS1 were identified as chalcophyllite. The analysis did not reveal any other phases within the detection limits of the method (Fig. 3b). Observations made with a scanning electron microscope (SEM) show that chalcophyllite has a lamellar segregation (Fig. 3c). Chemical analysis of the crystals performed with an energy dispersive spectrometer (EDS, data not shown) confirmed the presence of Cu, Al, S, As, and O in their composition.

In the LS2 sample, the studied mineral has a blue-green color. It forms veins and larger aggregates. The crystal sizes range from about 0.5 mm to about 4 mm. Some reach 6 mm. The veins have an average thickness of about

1.5 mm, but there are also 3 mm thick. The mineral has a glassy luster and a pale green streak (Fig. 4a). It occurs in strongly cracked quartz-limonite breccias. Based on the results of the XRD analysis, the green crystals from the LS2 sample were identified as euchroite. The analysis did not reveal any other phases within the detection limits of the method (Fig. 4b). Observations made using SEM show that in the tested sample, the euchroite crystals are irregular and cracked, have a conchoidal fracture, and the surfaces of the crystal walls are uneven (Fig. 4c). EDS chemical analysis (data not presented) confirmed the presence of Cu, As and O in their composition.

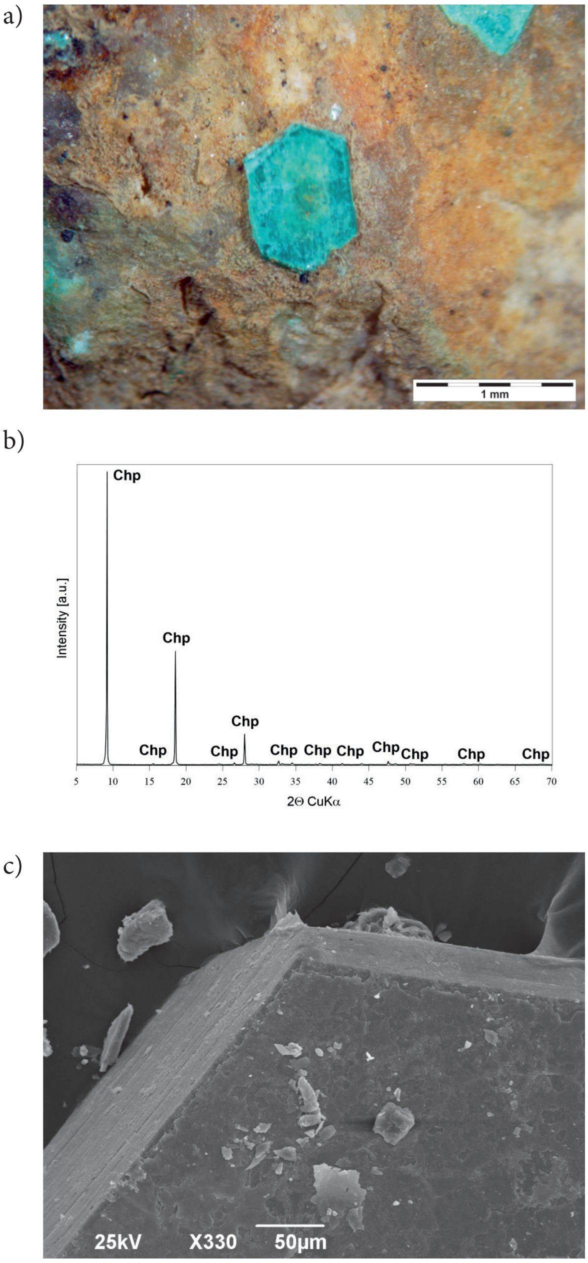

Fig. 3. Sample LS1: a) macrophotography of chalcophyllite; b) the XRD patterns of chalcophyllite (Chp); c) the SEM images of chalcophyllite

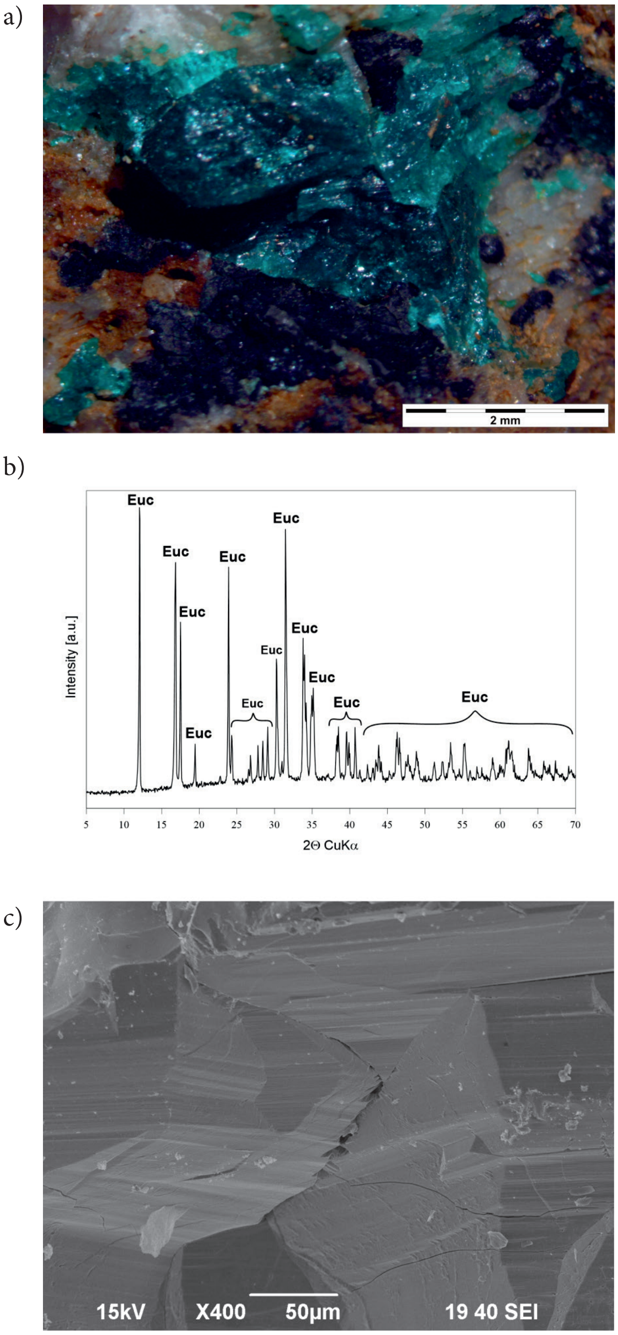

Fig. 4. Sample LS2: a) macrophotography of euchroite; b) the XRD patterns of euchroite (Euc); c) the SEM images of euchroite

In the LS3 sample, the studied mineral has an olive color. It forms very fine-crystalline clusters in druses and voids and on the surface. It has a diamond luster (Fig. 5a). Based on the XRD analysis results, very fine dark green crystals from the LS3 sample were identified as olivenite. In addition to olivenite peaks, peaks originating from minerals from the garnet group, potassium feldspars and plagioclase are also visible (Fig. 5b). Observations made using SEM show that in the tested sample, olivenite forms mostly thick-tabular or pyramidal crystals. The wall surfaces are uneven, rough (Fig 5c). EDS chemical analysis (data not presented) confirmed the presence of Cu, As and O in their composition.

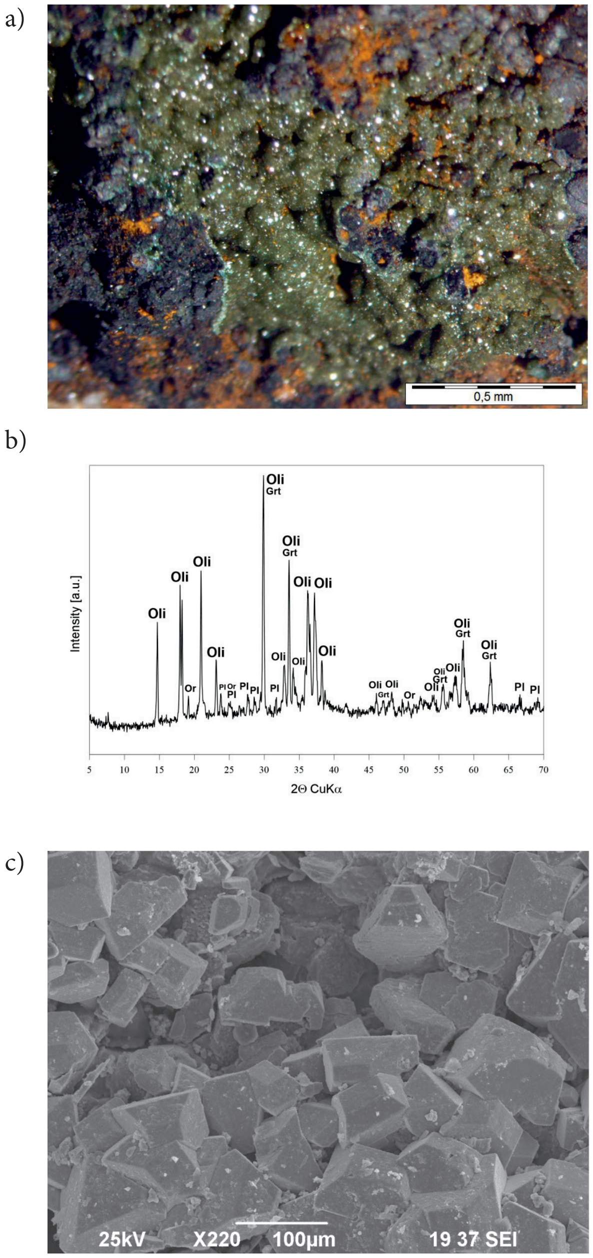

Fig. 5. Sample LS3: a) macrophotography of olivenite; b) the XRD patterns (Oli – olivenite, Grt – garnet, Or – potassium feldspar, Pl – plagioclase); c) the SEM images of olivenite

In the LS4 sample, the studied mineral has a light green color. It forms very small crystals. Their size ranges from 0.1 to 1.5 mm. Crystals of 0.5 mm and smaller predominate. The mineral has a glassy luster (Fig. 6a). It appears in the zones between quartz veins and limonite. Based on the results of the XRD analysis, the light green crystals from the LS4 sample were identified (similarly to the LS3 sample) as olivenite. The diffraction pattern shows mostly peaks originating from olivenite. One can also observe peaks indicating the presence of mica (muscovite), quartz and a small amount of euchroite (Fig 6b). Observations made using SEM show that in the tested sample olivenite forms plates or elongated crystals. They have an uneven surface and form intergrowths (Fig 6c). EDS chemical analysis (data not presented) confirmed the presence of elements such as Cu, As and O.

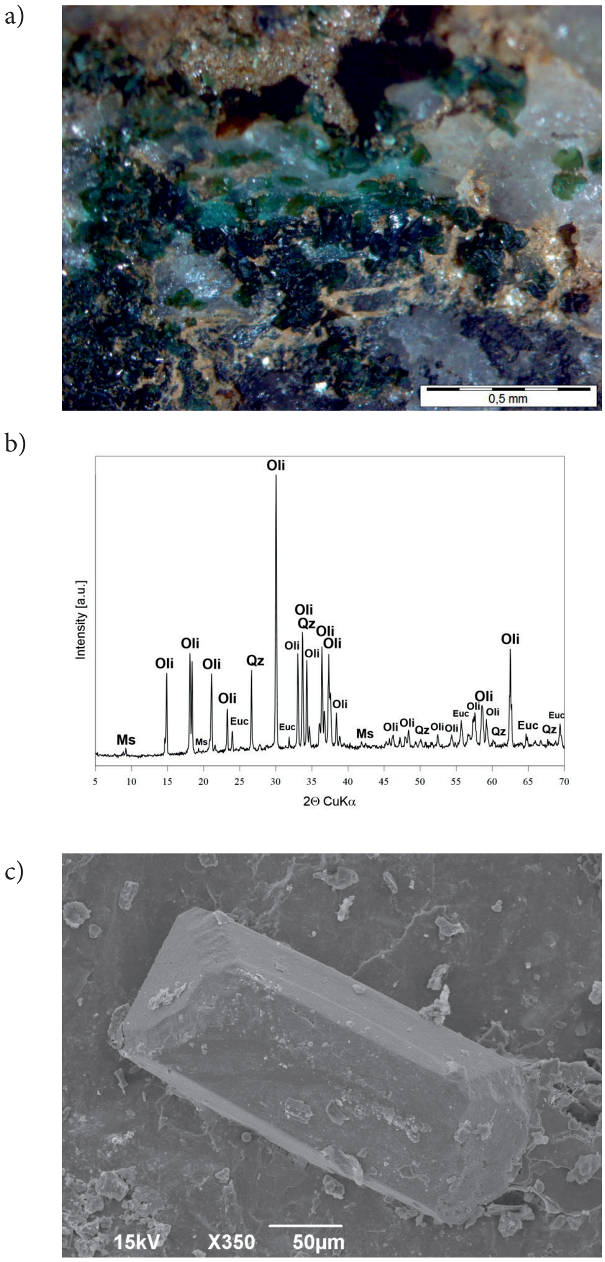

Fig. 6. Sample LS4: a) macrophotography of olivenite; b) the XRD patterns (Oli – olivenite, Ms – muscovite, Qz – quartz, Euc – euchroite); c) the SEM images of olivenite

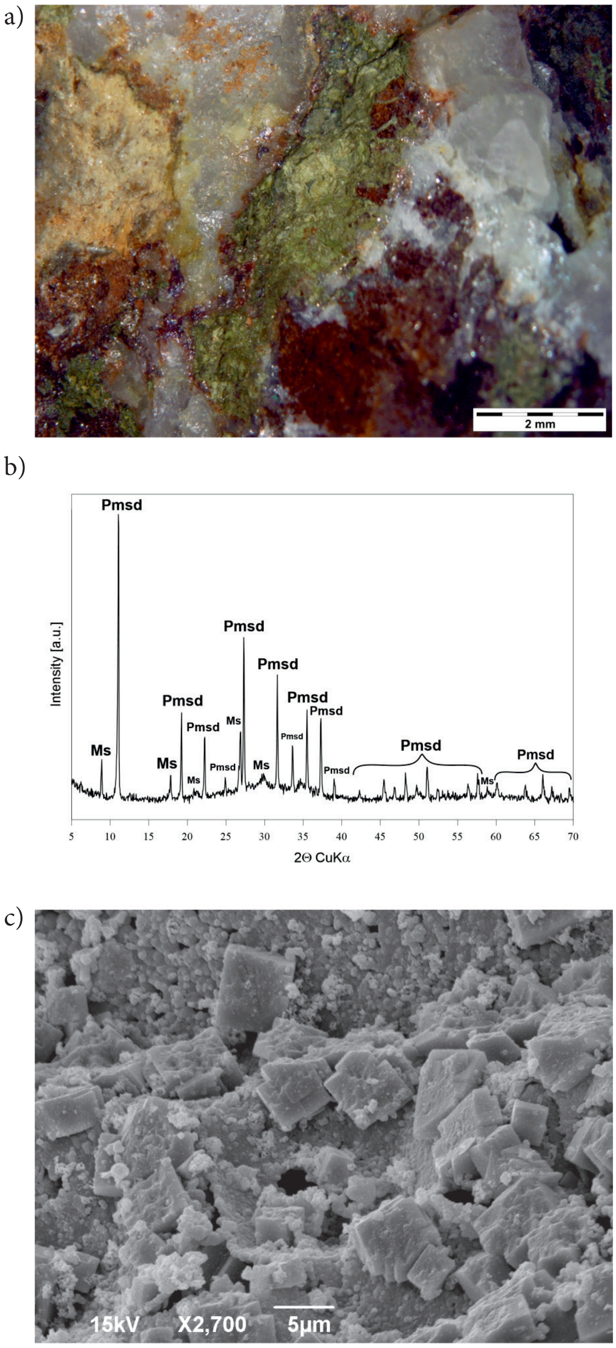

Fig. 7. Sample LS5: a) macrophotography of pharmacosiderite; b) the XRD patterns (Pmsd – pharmacosiderite, Ms – muscovite); c) the SEM images of pharmacosiderite

In the LS5 sample, the studied mineral has a light green color. It is found on limonite (more often) and quartz. It is a very loose mineral. It has a matte, dusty, and sometimes oily luster (Fig. 7a). Based on the results of the XRD analysis, the light green mineral from the LS5 sample was identified as pharmacosiderite. In addition to the pharmacosiderite peaks, the diffractogram also shows peaks indicating the presence of micas (Fig. 7b). Observations made using SEM show that in the sample under study, pharmacosiderite forms thin rhombohedral plates or oval grains (Fig. 7c). EDS chemical analysis (data not presented) confirmed the presence of elements such as As, Fe, and O, which corresponds to the chemical composition of minerals from the pharmacosiderite group.

Macroscopic observations and observations using a scanning electron microscope (SEM) of the tested arsenate samples confirm the forms of their occurrence presented in the literature [4]. Observations using SEM and chemical analysis (EDS) showed that some of the tested crystals are heterogeneous, contain various substitutions and show significant variability in the content of individual elements within single grains.

6. Conclusions

In summary, numerous secondary minerals were found in the Ľubietová-Svätodušná deposit heap, but only four of them belonged to the arsenate group. These were chalcophyllite, euchroite, pharmacosiderite and olivenite. These minerals were described and characterized in detail using XRD and SEM/EDS. It was noted that euchroite and olivenite predominate in the arsenate heap. Euchroite is emerald green in color and occurs mainly in the form of veins filling the cracks, while olivenite forms various crystals with colors from light to dark green. It appears both in the form of plates and small needles. Sometimes the needles form radial clusters. The results of SEM-EDS analyses showed that natural arsenates do not form pure phases, they contain numerous substitutions.

Funding: This research received no external funding.

Conflicts of Interest: The author of this paper declares no conflicts of interest.

References

[1] Pongratz R.: *Arsenic Speciation in Environmental Samples of Contaminated Soil.* Science of the Total Environment, 224, 1998, pp. 133–141.

[2] Ernst W.H.O., Josse-van Damme E.N.G.: *Zanieczyszczenie środowiska substancjami mineralnymi.* Państwowe Wydawnictwo Rolnicze i Leśne, Warszawa 1989, pp. 219–229.

[3] Haidinger W.: *Ueber den Euchroit, eine neue Mineralspecies. 1. Vorläufige Notiz über dieses Mineral.* Journal für Chemie und Physik, 45, 1825, pp. 231–232.

[4] Koděra M. (ed.): *Topografická Mineralógia Slovenska. II.* Vydavateľstvo SAV, Bratislava 1990, pp. 731–738.

[5] Figuschová M.: *Sekundárne minerály medi z Ľubietovej.* In: *Zborník referátov z konferencie Ložiskotvorné procesy Západných Karpát*, Bratislava 1977, pp. 135–137.

[6] Magalhäes M.C.F., Pedrosa de Jesus J.D., Williams P.A.: *The Chemistry of Formation of Some Secondary Arsenate Minerals of Cu(II), Zn(II) and Pb(II).* Mineralogical Magazine, 52, 1988, pp. 679–690.

[7] Řidkošil T., Medek Z.: *Nové nálezy nerostů na lokalite Svätoduška na středním Slovensku.* Časopis pro Mineralogii a Geologii, 26, 1, 1981, pp. 91.

[8] Charykova M.V., Krivovichev V.G., Depmeier W.: *Thermodynamics of Arsenates, Selenites, and Sulfates in the Oxidation Zone of Sulfide Ores: Part I: Thermodynamic Constants at Ambient Conditions.* Geology of Ore Deposits, 52, 8, 2010, pp. 689–700.

[9] Števko M., Sejkora J., Bačík P.: *Mineralogy and Origin of Supergene Mineralization at the Farbište Ore Occurrence Near Poniky, Central Slovakia.* Journal of Geosciences, 56, 2011, pp. 273–298.

[10] Charykova M.V., Krivovichev V.G., Yakovenko O.S., Depmeier W.: *Thermodynamics of Arsenates, Selenites, and Sulfates in the Oxidation Zone of Sulfide Ores: Part III: Eh-pH Diagrams of the Me-As-H2O Systems (Me = Co, Ni, Fe, Cu, Zn, Pb) at 25°C.* Geology of Ore Deposits, 53, 7, 2011, pp. 501–513.

[11] Majzlan J., Števko M., Dachs E., Benisek A., Plášil J., Sejkora J.: *Thermodynamics, Stability, Crystal Structure, and Phase Relations among Euchroite, $Cu_2(AsO_4)(OH)\cdot 3H_2O$, and Related Minerals.* European Journal of Mineralogy, 29, 1, 2017, pp. 5–16.

[12] Frost R.L., Bahfenne S.: *Thermal analysis and Hot-stage Raman spectroscopy of the basic copper arsenate mineral.* Journal of Thermal Analysis and Calorimetry, 100, 2010, pp. 89–94. https://doi.org/10.1007/s10973-009-0599-x.

[13] Eby R.K., Hawthorne F.C.: *Euchroite, a Heteropolyhedral Framework Structure.* Acta Crystallographica Section C: Structural Chemistry, 45, 1989, pp. 1479–1482.

[14] Frost R.L., Čejka J., Sejkora J., Plášil J., Bahfenne S., Palmera S.J.: *Raman spectroscopy of the basic copper arsenate mineral: euchroite*. Journal of Raman Spectroscopy, 41, 2010, pp. 571–575.

[15] Krivovichev S.V., Zolotarev A.A., Pekov I.V.: *Hydrogen bonding system in euchroite, Cu2(AsO4)(OH)(H2O)3: low-temperature crystal-structure refinement and solid-state density functional theory modeling*. Mineralogy and Petrology, 110, 2016, pp. 877–883. https://doi.org/10.1007/s00710-016-0450-6.

[16] Frost R.L., Reddy B.J., Keeffe E.C.: *Spectroscopy of selected copper group minerals: Chalcophyllite and chenevixite-implications for hydrogen bonding*. Spectrochimica Acta Part A: Molecular and Biomolecular Spectroscopy, 77, 2010, pp. 388–396.

[17] Janicka U.: *Asocjacja wtórnych arsenianów złoża Ľubietová-Svätodušná i eksperymentalna symulacja warunków towarzyszących ich powstawaniu*. Master thesis, KGZiG WGGiOŚ AGH Archive, Kraków 2012.

[18] Wyrobek P., Sermet E., Musiał A.: *Ľubietovskie hałdy miedziowe – świadkowie dziejów górnictwa w centralnej Słowacji*. Górnictwo Odkrywkowe, 3, 2017, pp. 49–55.

[19] Bezák V., Biely A., Elečko M., Konečný V., Mello J., Polák M., Potfaj M.: *A new synthesis of the geological structure of Slovakia – the general geological map at 1:200 000 scale*. Geological Quarterly, 55, 2011, pp. 1–8.

[20] Bezák V. (ed.), Elečko M., Fordinál K., Ivanička J., Kaličiak M., Konečný V., Kováčik M., Maglay J., Mello J., Nagy A., Polák M., Potfaj M., Biely A., Bóna J., Broska I., Buček S., Filo I., Gazdačko Ľ., Grecula P., Gross P., Havrila M., Hók J., Hraško Ľ., Jacko S. (jn.), Jacko S. (sn.), Janočko J., Kobulský J., Kohút M., Kováčik M., Lexa J., Madarás J., Németh Z., Olšavský M., Plašienka D., Pristaš J., Rakús M., Salaj J., Siman P., Šimon L., Teťák F., Vass D., Vozár J., Vozárová A., Žec B.: *General geological map of the Slovak Republic 1:200,000*. Ministry of Environment of the Slovak Republic, State Geological Institute of Dionýz Štúr, Bratislava 2008.

[21] PHSR Ľubietová: *Program hospodárskeho a sociálneho rozvoja obce na roky 2009–2013 – Ľubietová*, 2008.

[22] Hvožďara P.: *Štúdium zlatých mineralizácii niektorých jadrových pohorí Západných Karpát*. Manuscript, Geofond, Bratislava 1971.

Journal of Geotechnology and Energy | vol. 41 | no. 4 | 2024 | pp. 43–52

https://doi.org/10.7494/jge.2024.41.4.6737

ARTICLE

POSSIBILITIES OF APPLYING THE EXTENDED EYRING RHEOLOGICAL MODEL IN THE TECHNOLOGY OF CEMENT SLURRIES USED IN OIL DRILLING

Krzysztof Skrzypaszek

AGH University of Krakow, Faculty of Drilling, Oil and Gas, Poland
ORCID: 0000-0003-2358-7361
e-mail: varna@agh.edu.pl

Date of submission:
19.11.2024

Date of acceptance:
20.11.2024

Date of publication:
30.12.2024

https://journals.agh.edu.pl/jge

Abstract: This study explores the feasibility of implementing an extended Eyring rheological model to describe the dependence between shear stress and shear rate in cement slurries used in drilling technologies. Advances in cement slurry technology have rendered traditional mathematical models, particularly the widely used linear Bingham model recommended by the API RP 13D (American Petroleum Institute Recommended Practice 13D) standard, insufficient for accurately predicting flow resistance during pumping operations. A misalignment between the model and the actual behavior of cement slurries can result in significant errors, potentially increasing operational costs. By identifying and applying the relevant rheological model, it is possible to optimize the system's performance, minimizing total pressure losses and thereby reducing overall drilling costs. This paper investigates the applicability of more sophisticated three-parameter rheological models, commonly utilized in other engineering disciplines, to address these challenges. Specifically, the extended Eyring model was adapted to the proprietary RheoSolution methodology developed by the Department of Drilling, Oil and Gas. To validate this approach, a series of laboratory tests were conducted on cement slurries widely used in the oil industry. The results were analyzed and compared against mathematical models recommended by the API standard. The findings confirm that the extended Eyring model offers superior accuracy in determining the rheological parameters of cement slurries for drilling applications, underscoring its potential as a robust tool for improving the efficiency of drilling operations.

Keywords: drilling, rheology, drilling fluids, cement slurries, rheological model, computer aided, numerical methods, gradient method

1. Introduction

The first attempts to use cement in drilling were made in 1903 when Frank Hill applied it to seal off water in a drilling well. By 1910, well cementing began to develop on a larger scale, initiating systematic advancements in drilling cement technology. Today, cement is primarily used in drilling to seal the space between the wellbore and casing, reduce mud leakage, and create stabilizing plugs. The requirements for cement slurries used in deep well drilling and for sealing and strengthening operations in challenging geological conditions are continuously increasing. In drilling and geoengineering, there is a growing need to develop new cement formulations that meet these demands. However, less emphasis has been placed on procedures for verifying their flow and rheological parameters. The widely used standard – API RP 13D (American Petroleum Institute Recommended Practice 13D) – recommends employing the linear Bingham model and the exponential Ostwald–de Waele model [1–3]. However, experience in analyzing the flow parameters of cement slurries for various drilling applications suggests that these models are far from optimal and, in many cases, they produce results with significant errors [4]. In order to minimize these errors, a methodology for selecting the optimal rheological model for technological drilling fluids – RheoSolution by Prof. Rafal Wiśniowski and the author of this article [5–9] – was developed at the Faculty of Drilling Oil and Gas. The idea was to create an algorithm to evaluate the correlation of the mathematical model with the actual values of shear stress as a function of shear rate [11–12]. Higher correlation results in higher accuracy in calculating the amount of pressure loss when pumping cement slurry during the cementing procedure. The consequence of this is the selection of appropriate cementitious aggregates, which has an economic dimension. The procedure for determining rheological parameters (API RP 13D) can be improved by replacing simple mathematical models with more advanced ones (often with higher correlation) and by replacing more advanced viscosity meters with the Fann and Chan models widely used in the petroleum industry [1]. This article will present the application of the extended Eyring rheological model (so far not used in drilling practice) for the purpose of describing the dependence of shear stresses as a function of shear rate occurring during the pumping of sample cement slurries of various applications [8].

2. Rheological models used in the oil industry

The most popular used rheological models in the oil industry are [5, 9, 13–15].

- Bingham model:

$$\tau = \tau_y + \eta_{pl}\left(-\frac{dv}{dr}\right) \tag{1}$$

A linear model of a plastic body, which at rest has a three-dimensional structure with a certain elasticity. Once this elasticity is exceeded – the flow limit or yield point – the body flows. The flow limit is a measure of the intermolecular forces present in a fluid. Once it is exceeded, a Bingham body takes on the characteristics of a Newtonian fluid, in which stresses propagate in direct proportion to the forces causing them – linearly. The body is described by two parameters. This model is the first modification of Newton's model and was widely used as the basic rheological model because of its simplicity. It is now being replaced in most calculations by more complex models that better describe the dependence between shear stress and shear rate in a fluid.

- Ostwald–de Waele model:

$$\tau = k\left(-\frac{dv}{dr}\right)^n \tag{2}$$

Exponential pseudoplastic body model. This model was introduced when it was noticed that in the graph of shear stress from shear rate with both axes logarithmic, the plotted curve is close to a straight line. The equation is two-parameter and well describes the behavior of most fluids especially shear-thinning fluids, but it lacks consideration of the flow boundary in the form of a free expression.

- Herschel–Bulkley model:

$$\tau = \tau_y + k\left(-\frac{dv}{dr}\right)^n \tag{3}$$

Three-parameter model, an extension of the power model by supplementing it with the value of the flow limit. Currently, the model that is most widely used due to its high accuracy, versatility and the ability to adapt the model to the parameters. It describes pseudoplastic shearthinning fluids very well and describes dilatant shearthickening fluids well [3, 4].

Less commonly used models and not included in the API methodology are:

- Casson's model modified to a nonlinear form of Bingham's model. This is a pseudoplastic fluid model which is quite accurate in the low shear rate range while less accurate in the shear rate range >60 s^{-1}. It is rarely used in drilling practice [5, 13, 14].
- Newton's model – an equation describing a Newtonian fluid. For approximating the properties of non-Newtonian fluids, it is used occasionally, but

only when it is a sufficiently accurate approximation or in situations where accuracy is not required but simplicity of calculation is [4].

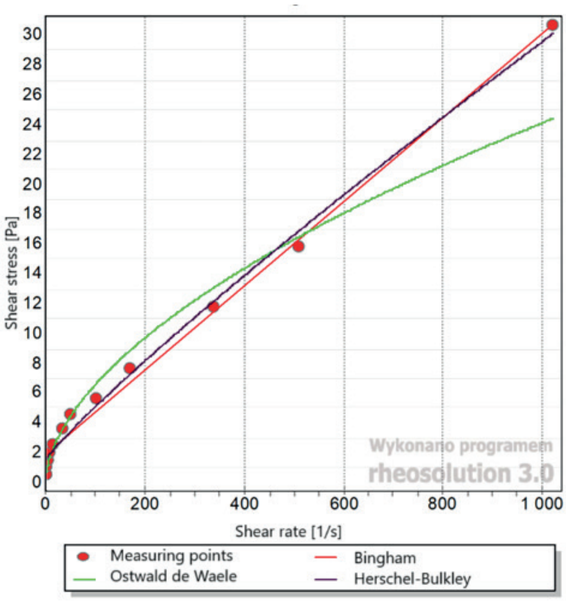

Fig. 1. Summary of rheological models for a sample test fluid recommended by API RP 13D standard: Bingham, Ostwald–de Waele, Herschel–Bulkley

The aforementioned models are successfully used in drilling practice, but it has been noted that linear models perform poorly in the low shear rate range and the process fluids used in drilling are now being modified with chemical additives essentially changing their initial flow parameters. Often during research there is a situation where some models better describe the dependence of shear stress as a function of shear rate for low shear rates and others perform better for high shear rates. Therefore, the author analyzed several rheological models used in other industries with the idea of adapting a multi-parameter rheological model for the drilling industry. The primary criterion was comparable or better correlation than the Herschel–Bulkley model for test data, which would provide a good reference for the applicability of the models in question. The Herschel–Bulkley power model gives the best fit in most situations and most accurately reflects the rheological parameters of the technological drilling fluids tested at the Faculty of Drilling, Oil and Gas. As a result of this analysis, the Eyring model extended with a linear element was selected for further study (4).

$$\tau = A\left(-\frac{dv}{dr}\right) + B\sinh^{-1}\left(\frac{-\frac{dv}{dr}}{C}\right) \tag{4}$$

The Eyring model gave very satisfactory results for simple fluids and suspensions, and when extended with a linear element also for cement slurries.

The Eyring model was chosen after analyzing rheological models used in other areas of engineering that are applied to fluids similar to cement slurries. The following rheological models were analyzed:

- Robertson – Stiff,
- Sisko,
- Vom Berg,
- Eyring,
- Ellis,
- Cross,
- Mizrahi – Berka,
- Vocaldo,
- Shangrawa – Grim – Mattocks.

3. Methodology for selecting the optimal rheological model – RheoSolution 5.0

The result of laboratory tests conducted with FANN-type rotational viscometers is a set of measuring points, where the values of shear stresses in the technological fluid arising under different shear rates are given. Regression is used to fit the rheological parameters of the model to the values of the measurement points. For the Bingham model, which is a linear model, and for the exponential Ostwald–de Waele model, which can be linearized, linear regression analysis is used [6]. Another recommended rheological model of Herschel–Bulkley cannot be linearized, because when determining the equations of the parameters, an entangled equation of one variable will be obtained. Also, the linearization of equations is not possible for the postulated Eyring model, the notation of these models is as follows.

- Herschel–Bulkley [5, 8]:

$$\tau = \tau_y + k\left(-\frac{dv}{dr}\right)^n \tag{5}$$

Simplified formulation for the Herschel–Bulkley model:

$$y = a + bx^c \tag{6}$$

Least squares method for the Herschel–Bulkley model:

$$\begin{aligned} U &= \sum_{i=1}^{m}(y_i - (a + bx_i^c))^2 \\ &= \sum_{i=1}^{m}(y_i^2 - 2y_i - 2bx_i^c + a^2 + 2abx_i^c + b^2x^{2c}) \to \min \end{aligned} \tag{7}$$

The partial derivatives of the parameters *a*, *b* and *c* form the following system of equations:

$$\begin{cases} \dfrac{\partial U}{\partial a} = -2\sum\limits_{i=1}^{m} y_i + 2b\sum\limits_{i=1}^{m} x_i^c + 2am = 0 \\ \dfrac{\partial U}{\partial b} = -2\sum\limits_{i=1}^{m} y_i x_i^c + 2a\sum\limits_{i=1}^{m} x_i^c + 2b\sum\limits_{i=1}^{m} x_i^{2c} = 0 \\ \dfrac{\partial U}{\partial c} = -2\sum\limits_{i=1}^{m} (y_i x_i^c \ln x_i) + 2ab\sum\limits_{i=1}^{m} (x_i^c \ln x_i) \\ \qquad + 2b^2\sum\limits_{i=1}^{m} (x_i^{2c} \ln x_i) = 0 \end{cases} \tag{8}$$

- Eyring:

$$\tau = A\left(-\frac{dv}{dr}\right) + B\sinh^{-1}\left(\frac{-\dfrac{dv}{dr}}{C}\right) \tag{9}$$

Simplified formulation for the Eyring model:

$$y = ax + b\sinh^{-1}\left(\frac{x}{C}\right) \tag{10}$$

Least squares method for the Eyring model:

$$\begin{aligned} U &= \sum_{i=1}^{m}\left(y_i - \left(ax_i + b\sinh^{-1}\left(\frac{x_i}{c}\right)\right)\right)^2 \\ &= \sum_{i=1}^{m}\left(y_i^2 - 2ax_i y_i - 2y_i b\sinh^{-1}\left(\frac{x_i}{c}\right) + a^2x_i^2\right. \\ &\quad \left. + 2ax_i b\sinh^{-1}\left(\frac{x_i}{c}\right) + b^2\left(\sinh^{-1}\left(\frac{x_i}{c}\right)\right)^2\right) \end{aligned} \tag{11}$$

The system of equations is formed by the partial derivatives of the parameters *a*, *b* and *c*:

$$\begin{cases} \dfrac{\partial U}{\partial a} = \sum\limits_{i=1}^{m}(-2x_i\left(-ax_i - b\sinh^{-1}\left(\dfrac{x_i}{c}\right) + y_i)\right) = 0 \\ \dfrac{\partial U}{\partial b} = \sum\limits_{i=1}^{m}\left(-2\sinh^{-1}\left(\dfrac{x_i}{c}\right)\left(-ax_i - b\sinh^{-1}\left(\dfrac{x_i}{c}\right) + y_i\right)\right) = 0 \\ \dfrac{\partial U}{\partial c} = \sum\limits_{i=1}^{m}\dfrac{2bx_i\left(-ax_i - b\sinh^{-1}\left(\dfrac{x_i}{c}\right) + y_i\right)}{c^2\sqrt{1 + \dfrac{x_i^2}{c^2}}} = 0 \end{cases} \tag{12}$$

The systems of derived equations are unsolvable analytically, as attempts result in a tangled equation involving a single variable. To address this, nonlinear regression techniques are essential for estimating equation parameters. One commonly used method is the gradient-based approach [7, 10, 15]. This technique identifies local minima within a function and selects the smallest one as the global minimum. The procedure involves starting from an initial point in the function's domain, where the fit of the model is evaluated as the sum of squared differences. A vector is then calculated, moving in the reverse direction of the function's gradient. The step size is determined by a unit value adjusted by a scaling factor, which can be tuned to improve the method's performance.

$$U(a,b,c) = \sum_{i=1}^{n}(f(a,b,c) - y_i)^2 \to \min \tag{13}$$

$$\hat{v} = \frac{-\vec{\nabla}U(a,b,c)}{\left|-\vec{\nabla}U(a,b,c)\right|}\cdot\alpha_k \tag{14}$$

The parameters of the model are adjusted based on the vector values, with the algorithm treating the modified point as a fresh starting location. This process repeats iteratively until a local minimum is achieved with the specified precision. Once this is done, the initial point is relocated, and the search for another local minimum begins. After executing the algorithm a set number of times, the smallest local minimum among those discovered is identified and accepted as the global minimum. A depiction of this process can be found in Figure 2 [11, 12, 15].

To simplify the notation, individual parameters are assigned to variables ***a***, ***b***, ***c***, and constants $\boldsymbol{y_i}$ and $\boldsymbol{x_i}$ are data from successive measurement points [10]. With each step, only the variables are modified (Fig. 3). Assignment of the model equations to the scheme:

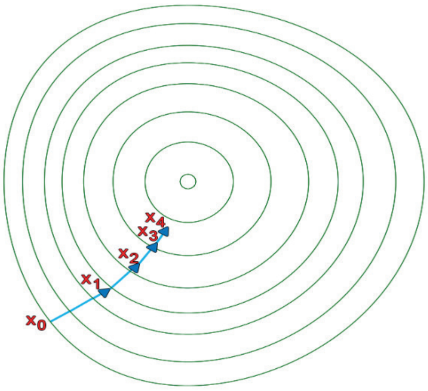

Fig. 3. Graphical representation of the gradient method

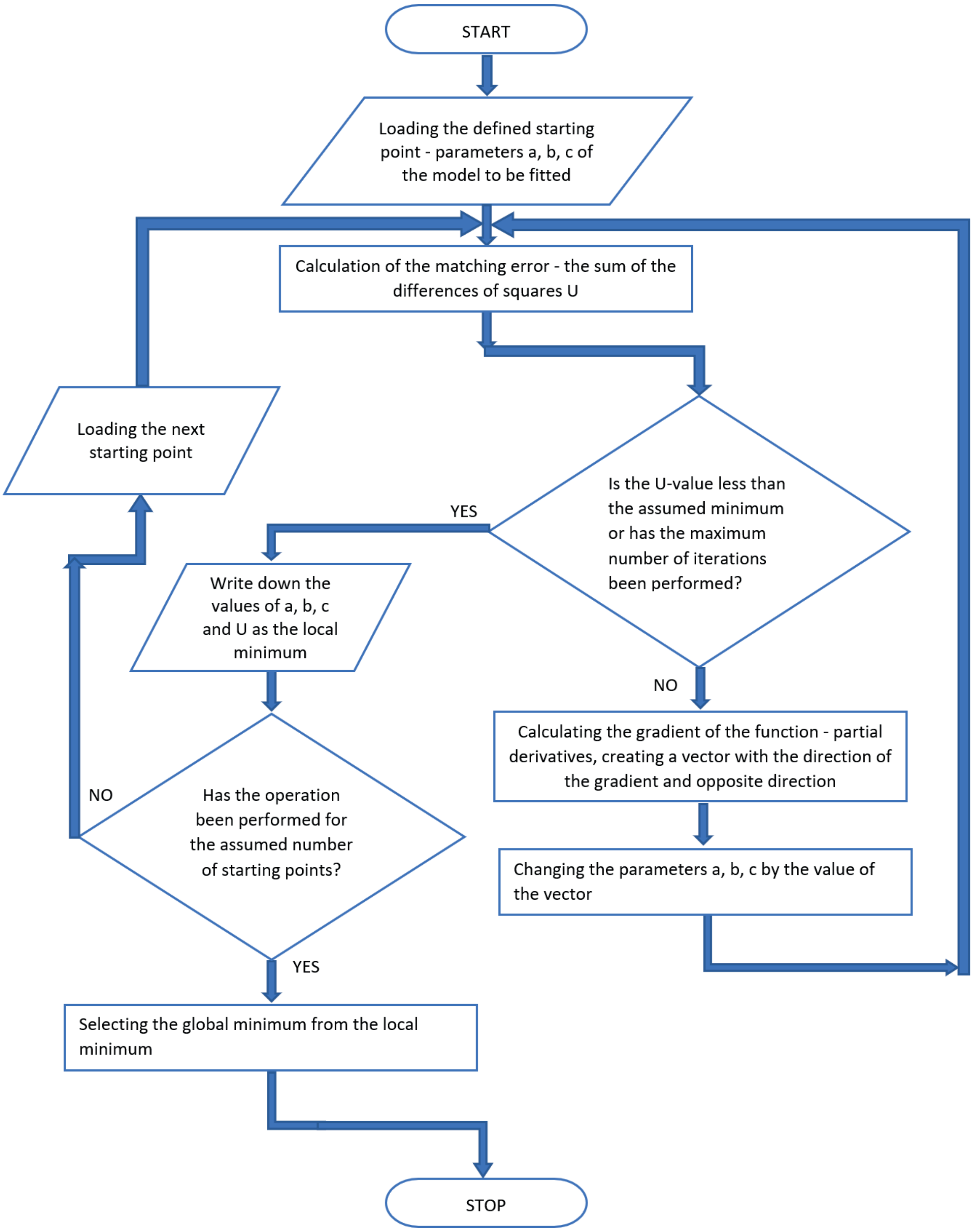

Fig. 2. Algorithm diagram for the simple gradient method

To streamline the notation, individual parameters are represented as variables *a*, *b*, and *c*, while the constants y_i and x_i correspond to data from consecutive measurement points (10). At each iteration, only the variables are updated.

The model equations are then incorporated into the framework as follows:

$$\tau = A\left(-\frac{dv}{dr}\right) + B\sinh^{-1}\left(\frac{-\frac{dv}{dr}}{C}\right) \qquad (15)$$

$$\begin{aligned} a &= A \\ b &= B \\ c &= C \\ y_i &= \tau_i \\ x_i &= -\frac{dv}{dr_i} \end{aligned} \tag{16}$$

$$U(a,b,c) = \sum_{i=1}^{n} \left(f(a,b,c) - y_i \right)^2 = \sum_{i=1}^{n} \left(ax_i + b\sinh^{-1}\left(\frac{x_i}{c} \right) - y_i \right)^2 \rightarrow \min \tag{17}$$

This method is universal and, once the formulas for the partial derivatives (6) are derived, it can be applied to any model with any number of parameters [12, 15], which greatly facilitates the process of implementing subsequent models into tools such as the RheoSolution 5.0 program developed at the Department of Drilling and Geoengineering of the Faculty of Drilling, Oil and Gas based on the proprietary RheoSolution methodology.

4. Laboratory testing

To verify the applicability of the extended Eyring model in determining the rheological parameters of cement slurries, laboratory tests were conducted on sample cement slurries. Samples 1 and 2 are relatively simple cement slurries modified with additives used in geothermal drilling. Samples 3, 4, 5 are cement slurries with w/c ratios = 0.5 that differ in the type of cement used in their preparation [4]. The tests were performed using a 12-range viscosity meter of the FANN type recommended by the API standard [3]. Then, using the RheoSolution methodology presented earlier, the rheological parameters, statistical parameters and correlation of the Bingham, Ostwald–de Waele and the Herschel–Bulkley models with the laboratory fluid tested were determined [2]. The results of these calculations served as a reference to the results obtained with the extended Eyring model and are shown in Tables 1–10 and Figures 4–8.

Sample No. 1: cement slurry w/c = 0.6 (CEM I 42.5R) with the addition of 20% diatomite (BWOC).

Table 1. Results of rheological measurements for sample No. 1

Rotor speed [rot/min]	Angle [°]	Shear rate [s^{-1}]	Shear stress [Pa]
600	107	1 022.040	54.643
300	69	511.020	35.237
200	56	340.680	28.598
100	37	170.340	20.427
60	28	102.204	16.852
30	24	51.102	13.278
20	21	34.068	11.746
10	18	17.034	9.192
6	13	10.220	6.639
3	8	5.110	4.085
2	7	3.406	3.575
1	4	1703	2.043

Table 2. Summary of correlation coefficients of the analyzed rheological models for sample No. 1

Rheological model	Pearson correlation coefficient, *R*	Fischer-Sneadecor coefficient, *F*	Sum of squares, *U*
Bingham	0.978	1 021.92	54.64
Ostwald–de Waele	0.992	510.96	35.23
Herschel–Bulkley	0.995	340.64	28.59
Eyring	0.998	2 848.47	9.42

The determined rheological parameters of the Eyring model for sample No. 1: parameter A – 0.03834 [Pa·s], parameter B – 2.10052 [Pa·s], parameter C – 0.87642 [–].

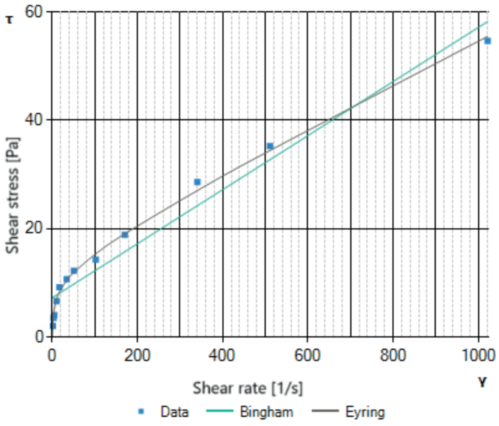

Fig. 4. Comparison of the Eyring model with the Bingham model (API) for sample No. 1

Sample No. 2: cement slurry w/m = 1.1 (CEM I 42.5R) with the addition of 20% graphite (BWOC).

Table 3. Results of rheological measurements for sample No. 2

Rotor speed [rot/min]	Angle [°]	Shear rate [s^{-1}]	Shear stress [Pa]
600	39	1 022.040	21.448
300	26	511.020	13.278
200	17	340.680	8.682
100	9	170.340	4.596
60	6	102.204	3.066
30	4	51.102	2.044
20	3	34.068	1.533
10	3	17.034	1.533
6	2	10.220	1.022
3	2	5.110	1.022
2	1	3.406	0.511
1	1	1.703	0.511

Table 4. Summary of correlation coefficients of the analyzed rheological models for sample No. 2

Rheological model	Pearson correlation coefficient, *R*	Fischer-Sneadecor coefficient, *F*	Sum of squares, *U*
Bingham	0.995	1 040.49	4.39
Ostwald–de Waele	0.948	87.95	47.09
Herschel–Bulkley	0.997	2 273.39	2.02
Eyring	0.997	1 485.24	3.08

Determined rheological parameters of the Eyring model for sample No. 2: parameter A – 0.01901 [Pa · s], parameter B – 0.3336 [Pa · s], parameter C – 1.1391 [–].

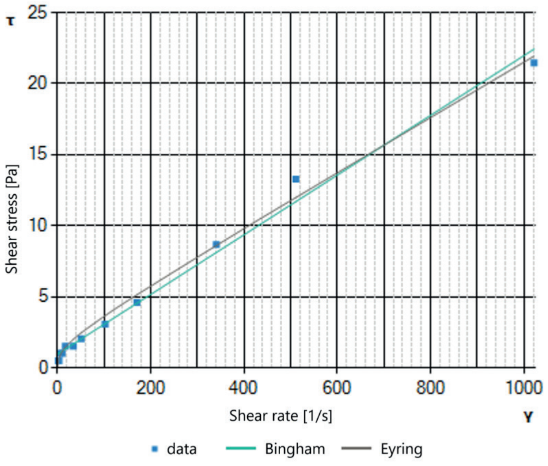

Fig. 5. Comparison of the Eyring model with the Bingham model (API) for sample No. 2

Sample No. 3: cement slurry w/c = 0.5 (CEM III/A 32.5R) without additives.

Table 5. Results of rheological measurements for sample No. 3

Rotor speed [rot/min]	Angle [°]	Shear rate [s^{-1}]	Shear stress [Pa]
600	Out of range	–	–
300	Out of range	–	–
200	112	340.680	57.196
100	85	170.340	43.408
60	72	102.204	36.769
30	57	51.102	29.109
20	49	34.068	25.023
10	34	17.034	17.363
6	24	10.220	12.256
3	15	5.110	7.660
2	11	3.406	5.617
1	8	1.703	4.085

Table 6. Summary of correlation coefficients of the analyzed rheological models for sample No. 3

Rheological model	Pearson correlation coefficient, *R*	Fischer-Sneadecor coefficient, *F*	Sum of squares, *U*
Bingham	0.917	42.34	453.29
Ostwald–de Waele	0.961	126.54	169.59
Herschel–Bulkley	0.984	266.41	83.14
Eyring	0.973	139.57	154.61

The determined rheological parameters of the Eyring model for sample No. 3: parameter A – 0.1081 [Pa · s], parameter B – 3.1171 [Pa · s], parameter C – 0.2797 [–].

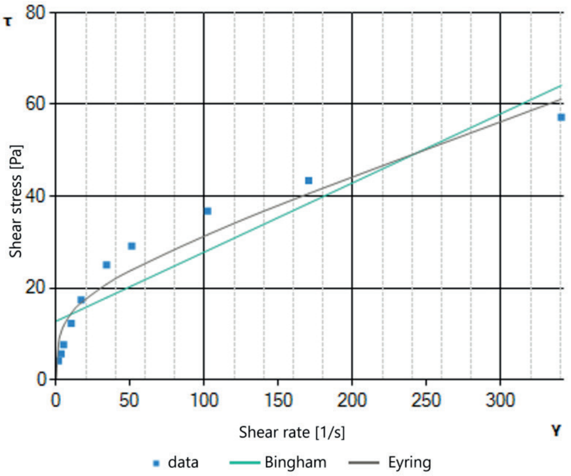

Fig. 6. Comparison of the Eyring model with the Bingham model (API) for sample No. 3

Sample No. 4: cement slurry w/c = 0.5 (CEM I 42.5R) without additives.

Table 7. Results of rheological measurements for sample No. 4

Rotor speed [rot/min]	Angle [°]	Shear rate $[s^{-1}]$	Shear stress [Pa]
600	144	1 022.040	73.538
300	103	511.020	52.600
200	77	340.680	39.322
100	57	170.340	29.109
60	46	102.204	23.491
30	35	51.102	17.874
20	30	34.068	15.320
10	23	17.034	11.746
6	15	10.220	7.660
3	11	5.110	5.617
2	9	3.406	4.596
1	7	1.703	3.575

Table 8. Summary of correlation coefficients of the analyzed rheological models for sample No. 4

Rheological model	Pearson correlation coefficient, *R*	Fischer-Sneadecor coefficient, *F*	Sum of squares, *U*
Bingham	0.964	42.34	360.64
Ostwald–de Waele	0.997	2 299.09	22.49
Herschel–Bulkley	0.998	2 843.365	18.21
Eyring	0.994	644.233	79.38

Determined rheological parameters of the Eyring model for sample No. 4: parameter A – 0.0544 [Pa · s], parameter B – 2.5926 [Pa · s], parameter C – 0.4705 [–].

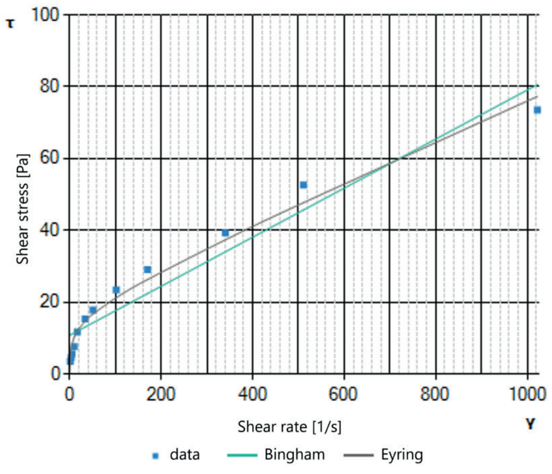

Fig. 7. Comparison of the Eyring model with the Bingham model (API) for sample No. 4

Sample No. 5: cement slurry w/c = 0.5 (CEM G HSR).

Table 9. Results of rheological measurements for sample No. 5

Rotor speed [rot/min]	Angle [°]	Shear rate $[s^{-1}]$	Shear stress [Pa]
600	118	1 022.040	60.260
300	78	511.020	39.833
200	61	340.680	31.151
100	45	170.340	22.981
60	37	102.204	18.895
30	29	51.102	14.810
20	26	34.068	13.278
10	20	17.034	10.214
6	15	10.220	7.660
3	10	5.110	5.107
2	8	3.406	4.085
1	6	1.703	3/064

Table 10. Summary of correlation coefficients of the analyzed rheological models for sample No. 5

Rheological model	Pearson correlation coefficient, *R*	Fischer-Sneadecor coefficient, *F*	Sum of squares, *U*
Bingham	0,971	168.567	180.58
Ostwald–de Waele	0.993	795.722	40.02
Herschel–Bulkley	0.996	1 355.444	23.61
Eyring	0.999	7 014.752	4.59

Determined rheological parameters of the Eyring model for sample No. 5: parameter A – 0.0388 [Pa · s], parameter B – 2.842 [Pa · s], parameter C – 1.2355 [–].

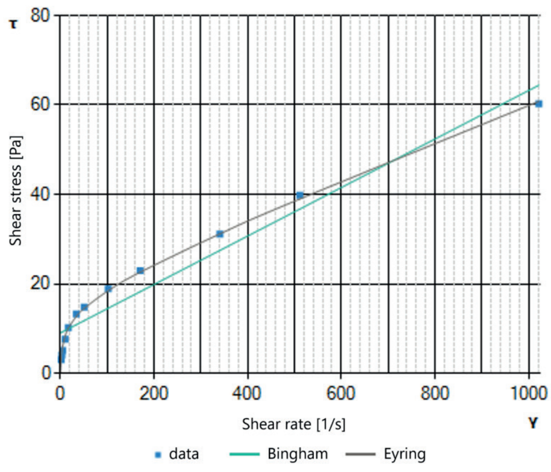

Fig. 8. Comparison of the Eyring model with the Bingham model (API) for sample No. 5

5. Conclusions

Analysis of the laboratory results obtained showed almost full correlation of the Eyring rheological model with all samples. The average correlation is 0.992 proving that the Eyring model is very suitable for describing cement slurries with basic formulations. Significant differences can be observed between the linear Bingham model and the Eyring model, particularly in the low shear rate range, where the Eyring model demonstrates better accuracy. In samples with a high yield stress, the Eyring model shows a much stronger correlation compared to the Ostwald–de Waele pseudoplastic fluid model. When compared to the Herschel–Bulkley model, the results are generally comparable, with the Eyring model showing a slight advantage. When studying the rheology of cement slurries used in the drilling industry, it is recommended to take into account the extended Eyring model, laboratory tests have shown its usefulness in this regard and the RheoSolution methodology is a tool that effectively helps select the appropriate rheological model for the cement slurry used in industrial practice. At the AGH Faculty of Drilling, Oil and Gas, further development work is being carried out on the usefulness of this model for other, more chemically complex technological drilling fluids. The Eyring model is implemented in the RheoSolution version 5 software, based on the proprietary RheoSolution methodology, which is commonly used by academics and students of the Faculty of Drilling, Oil and Gas when studying technological fluids used in drilling.

Funding: The project was supported by the AGH University of Krakow, subsidy 16.16.190.779.

Conflicts of Interest: The author of this paper declares no conflicts of interest.

References

[1] Bourgoyne A.T., Milheim K.K., Chenevert M.E., Young F.S.: *Applied Drilling Engineering.* Society of Petroleum Engineers, SPE Textbook Series, Houston 1986, Section 4.8.

[2] Klotz J.A., Brigham W.E.: *Determining Parameters for the Herschel–Bulkley Model.* Journal of Petroleum Technology, 50, 1998, pp. 80–81.

[3] American Petroleum Institute. *Rheology and Hydraulics in Oil-Well Drilling Fluids (API RP 13D).* API Standards, Washington D.C. 2006.

[4] Pellegrino C., Faleshini F.: *Improving Sustainability in Concrete Industry by Using Recycled Materials.* Springer International Publishing, Cham 2016, pp. 37–43.

[5] Wiśniowski R., Skrzypaszek K., Toczek P.: *Analysis of Rheological Models in Drilling Fluid Dynamics: Vom Berg and Hahn–Eyring Approaches.* Energies, 15, art. 5583, 2022. http://doi.org/10.3390/en15155583.

[6] Kutner M.H., Nachtsheim C.J., Neter J., Li W.: *Applied Linear Statistical Models.* 5th ed., McGraw-Hill – Irwin, New York 2004.

[7] Chapra S.C.: *Applied Numerical Methods with MATLAB for Engineers and Scientists.* 3rd ed., McGraw-Hill Education, New York 2012.

[8] Press W.H., Teukolsky S.A., Vetterling W.T., Flannery B.P.: *Numerical Recipes: The Art of Scientific Computing.* 3rd ed., Cambridge University Press, Cambridge, 2007.

[9] Wiśniowski R.: *Application of Nonlinear Models in Drilling Fluid Hydraulics.* Modern No-Dig Techniques and Technologies, 2, 2000, pp. 20–28.

[10] Wiśniowski R., Skrzypaszek K., Małachowski T.: *Numerical Analysis for Selecting Rheological Models of Drilling Fluids.* Energies, 13, art. 3192, 2020.

[11] Sharma M.M., Zhang R., Chenevert M.E.: *Novel Nanoparticle-Based Drilling Fluids.* SPE Annual Technical Conference and Exhibition, San Antonio, October 8–10, 2012, pp. 1–13.

[12] Nocedal J., Wright S.J.: *Numerical Optimization.* 2nd ed., Springer, New York 2006.

[13] Boyd S., Vandenberghe L.: *Convex Optimization.* Cambridge University Press, Cambridge, 2004.

[14] Papo A.: *Rheological models for cement pastes.* Materials and Structures, 21, 1988, pp. 41–46. https://doi.org/10.1007/BF02472527.

[15] Stryczek S., Wiśniowski R., Skrzypaszek K.: *Kierunki rozwoju badań nad reologią płynów wiertniczych.* Wiertnictwo, Nafta, Gaz, 24, 1, pp. 243–250.

[16] Wiśniowski R., Skrzypaszek K.: *Analiza modeli reologicznych stosowanych w technologiach inżynierskich.* Wiertnictwo, Nafta, Gaz, 23, 1, pp. 293–299.

Nomenclature

Symbol	Explanations	Unit
a, b, c	regression coefficient	[–]
A, B, C	rheological parameter in the extended Eyring model	[–]
U	sum of residuals squared	[–]
F	Fisher-Snedecor index	[–]
dv/dr	gradient of shear rate	$[\mathrm{s}^{-1}]$
η_{pl}	plastic viscosity	[Pa·s]
$\dot{\gamma}_i$	shear rate measured at i^{th} rotate speed	$[\mathrm{s}^{-1}]$
k	consistency	$[\mathrm{Pa \cdot s^n}]$
m	measurements number	[–]
n	exponential index	[–]
R	correlation coefficient	[–]
τ	shear stress	[Pa]
τ_{i-}	shear stress measured at i-th rotational speed	[Pa]
τ_y	YP	[Pa]
$\bar{\tau}$	average value of shear stress	[Pa]
w/c	water/cement ratio	[–]
w/m	water/mixture ratio	[–]

Journal of Geotechnology and Energy | vol. 41 | no. 4 | 2024 | pp. 53–60

https://doi.org/10.7494/jge.2024.41.4.6730

ARTICLE

EVALUATION OF OPERATING CONDITIONS OF FILTRATION COLUMNS OF RELIEF WELLS SITED WITHIN THE "ŻELAZNY MOST" MINING WASTE DISPOSAL FACILITY

Jan Macuda

AGH University of Krakow, Faculty of Drilling, Oil and Gas, Poland
ORCID: 0000-0002-8180-8014
e-mail: macuda@agh.edu.pl

Date of submission:
15.11.2024

Date of acceptance:
22.11.2024

Date of publication:
30.12.2024

https://journals.agh.edu.pl/jge

Abstract: Regardless of geological conditions, the drilling of deep wells always disturbs the original state of tension in the drilled rock mass. In the course of drilling, the stability of the borehole wall is maintained by the drilling mud, and afterwards by the installed casing or filtration column, which usually are steel or plastic pipes with appropriately designed diameter and wall thickness.

Casing columns in the wellbore should be sized so as to withstand the pressure of the rock mass without becoming deformed. Their strength parameters can be determined from the components of the primary state of stress in the rock mass and the magnitude of pressure occurring at the interface between the casing wall or filtration column wall, and the rock environment.

In this paper, an analytical method based on the Coulomb–Mohr model was used to calculate rock mass pressures around the filtration column of relief wells situated in the slope of the "Żelazny Most" Mining Waste Disposal Facility (MWDF).

Based on archival materials, a rock mass model was developed and was used for calculating undisturbed rock mass pressures at the filtration column wall and pressures coming from the gravel pack. The results obtained will be used for designing the filter pipe columns.

Keywords: borehole, borehole designing, rock mass pressure, strength of filtration columns, crushing of casing pipes

1. Introduction

Regardless of geological conditions, the drilling of deep wells always disturbs the original state of tension in the drilled rock mass. In the course of drilling, the stability of the borehole wall is maintained by the drilling mud, and afterwards by the installed casing or filtration column, which usually are steel or plastic pipes with appropriately designed diameter and wall thickness.

Casing columns in the wellbore should be sized so as to withstand the pressure of the rock mass without becoming deformed.

Their strength parameters can be determined from the components of the primary state of stress in the rock mass and the magnitude of pressure occurring at the interface between the casing wall or filtration column wall, and the rock environment. Apart from purely technological aspects, the proper operation of the well is determined by the strength of the casing, i.e. the applied casing column and filtration column.

If the compressive strength condition is to be met for the casing or filtration columns, a pressure distribution function around the drilled wellbore should be provided. Therefore, the geological and geotechnical conditions should be analyzed in detail and relevant factors affecting the behavior of the rock mass selected [1].

In rockmass mechanics, the analyzed phenomenon is described with mathematical equations. These are usually partial differential or ordinary differential equations defined in an area in which the analyzed phenomenon occurs. These equations supply the basis for developing a mathematical model of the studied phenomenon.

In the process of designing deep well structures implemented in formations having ground parameters, the Coulomb–Mohr model is most frequently used to calculate the rock mass pressures [2].

In this paper, an analytical method based on the Coulomb–Mohr model was used to calculate rock mass pressures around the filtration column of dewatering wells sited in the slope of the "Żelazny Most" Mining Waste Disposal Facility (MWDF).

2. Location and characteristic of the "Żelazny Most" MWDF

The "Żelazny Most" Mining Waste Disposal Facility is located in the Lower Silesia province, within the Lubin and Polkowice districts (Fig. 1). It was designed as a storing site for tailings from the processing and enrichment of copper ore provided by the Lubin, Polkowice-Sieroszowice, and Rudna mines. This facility is completely surrounded by earth embankments with a total length of 14.35 km. The area of the eastern dam, where the wells are planned, is located in the Rudna municipality [3].

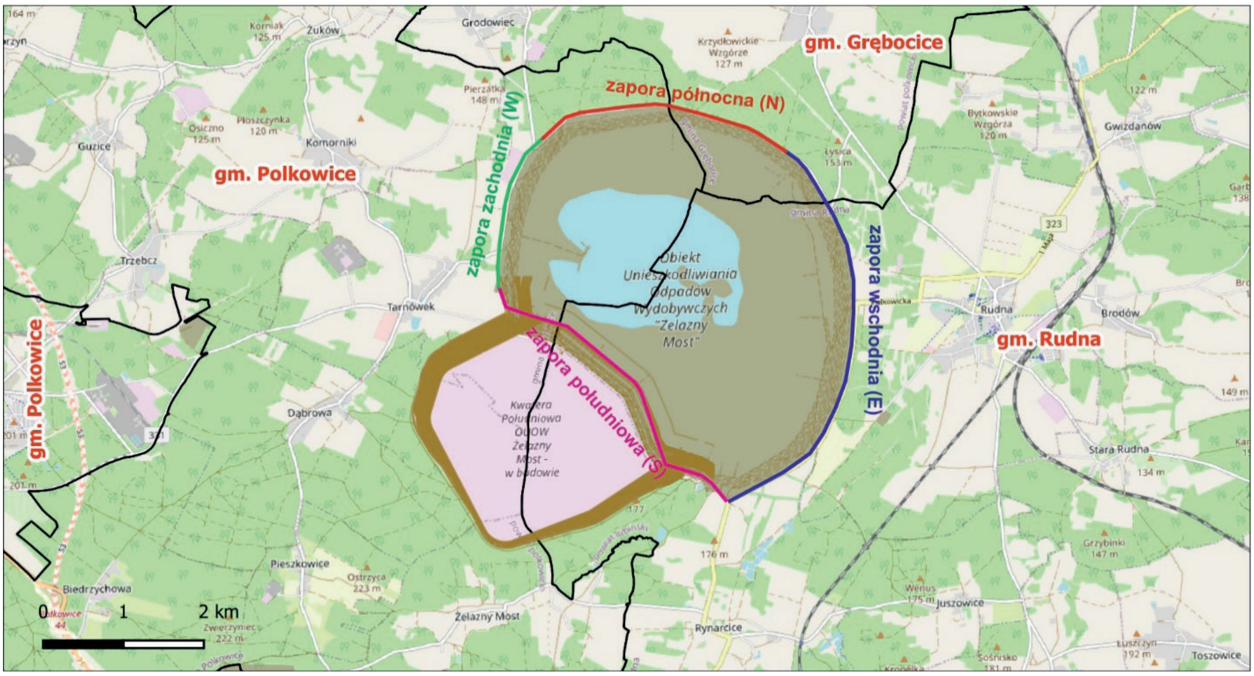

Fig. 1. Location of the "Żelazny Most" MWDF [3]

The embankments of the “Żelazny Most” MWDF are formed using the inward structure method in biennial cycles, at approximately 2.5-meter intervals within each of the 26 silted up sections. Silting up is carried out using a system of pipelines placed along the dam crown. Material from the deposited beach waste is used for shaping the structure, whereas landside slopes are protected with material from local deposits. Inside the reservoir there is a basin, filled with supernatant waters. The depth of the basin at its deepest point is about 3.0 meters. The supernatant water is captured by overflow towers and directed to a pumping station, from where it is pumped back to the Ore Enrichment Plant. After treatment, excess water is periodically discharged into the Oder River [3].

3. Characteristic of geological-engineering conditions

The general characteristics of the geological and engineering conditions in the area of the “Żelazny Most” MWDF are based on studies carried out in 2014–2023 [4, 5].

In the upper part of the subsoil of the analyzed area, Quaternary sediments with a thickness of several to several dozen meters occur. A zone of soils exhibiting the influence of periglacial processes taking place at the end of the Pleistocene are observed to a depth of several meters below the original ground surface. In places, in the near-surface part, young fluvial and stagnant Holocene formations with a large admixture of organic matter have also developed.

Pleistocene formations are mainly represented by sandy-gravel water glacial deposits, to a lesser extent morainic clays and silty clays or dust of stagnant origin. The deeper parts are mostly made up of Pliocene clays overlapped from the north and northwest, deformed glacitectonically several times during Pleistocene glaciations. They were subsequently severed and displaced as scales within the Quaternary sand and gravel deposits. These deformations also included overlays and interbeddings of silty and compact clays and lenses of sands and dusts within the clays. In some areas there are two overlaps and then they are separated by fluvioglacial deposits. The top surface of the overlap often forms outcrops under the sediments of the beach or the dam structure. The sediments of the Neogene are developed as dense gray-blue, blue-green and flame-green clays or spotted clays of the Poznan Pliocene series. Multiple, superimposed glacitectonic deformations have also led to a strong deglaciation of the clays, as well as the severing of smaller entrails and their secondary displacement [4, 5]. The geotechnical properties of subsoil of the “Żelazny Most” MWDF reservoir were recognized as part of a comprehensive and interdisciplinary research program, including both field and laboratory studies. Despite the very extensive research program, the geological model of the subsoil as well as the derived values of geotechnical parameters are still burdened with considerable uncertainty. The ground layers underlying the site as a result of the occurrence of many glacitectonic and periglacial processes, have been strongly deformed, displaced and shuffled, leading to a complex and hardly predictable arrangement of layers.

According to [4] the basic types of subsoil formations deciding on the stability of the site are solifluction silts and clays and Neogene silts occurring in the subsoil over the entire spectrum of variation in the values of index parameters. The soils with the highest plasticity, and therefore the weakest, can occur practically throughout the landfill area. Table 1 shows an exemplary profile of boreholes drilled to a depth of 350 m, along with the geomechanical parameters of the drilled rocks.

Table 1. Exemplary depth profile of ground layers with their geomechanical parameters for wellbore No. 1 [4]

Wellbore No. 1			ρ	ρ_{sat}	ϕ	c’	y	E	ν
Depth interval [m]	Lithology	Name of geotechnic layers according to [30]	[kN/m^3]	[kN/m^3]	[°]	[kPa]	[°]	[MPa]	[–]
0.0–7.5	NN	1	19	20.5	34	1	9	80	0.2
7.5–17.0	NN	3	18	19.5	34	1	9	80	0.2
17.0–21.0	NN	4	17	18.5	34	1	9	80	0.2
21.0–68.4	NN	4’	17	18.5	34	1	9	80	0.2
68.4–71.2	Sandy clay	7n	16.06	20	18	1	1.8	96	0.25
71.2–73.6	Compact clay	14n	20.20	–	20	5	–	–	–
73.6–82.4	Silt	9n	17.3	20.5	14.5	5	1.5	36	0.25
82.4–86.9	Fine sand	18n	15.86	19.8	30	1	5	240	0.2

Wellbore No 1			ρ	$\boldsymbol{\rho}_{sat}$	ϕ	c'	y	E	ν
Depth interval [m]	Lithology	Name of geotechnic layers according to [30]	[kN/m^3]	[kN/m^3]	[°]	[kPa]	[°]	[MPa]	[–]
86.9–98.9	Silt	9n	17.3	20.5	14.5	5	1.5	36	0.25
98.9–103.6	Fine sand	18n	15.86	19.8	30	1	5	240	0.2
103.6–111.8	Silt	9n	17.3	20.5	14.5	5	1.5	36	0.25
111.8–112.3	Silt	10n	16.8	20	10	1	1	36	0.25
112.3–113.2	Lignite	10n	16.8	20	10	1	1	36	0.25
113.2–121.8	Silt	10n	16.8	20	10	1	1	36	0.25
121.8–128.8	Silt	9n	17.3	20.5	14.5	5	1.5	36	0.25
128.8–133.9	Silty clay	9n	17.3	20.5	14.5	5	1.5	36	0.25
133.9–194.5	Silt	9n	17.3	20.5	14.5	5	1.5	36	0.25
194.5–198.1	Coaly silt	9n	17.3	20.5	14.5	5	1.5	36	0.25
198.1–208.3	Fine sand	18n	15.86	19.8	30	1	5	240	0.2
208.3–229.3	I; silt	9n	17.3	20.5	14.5	5	1.5	36	0.25
229.3–240.5	Compact clay	9n	17.3	20.5	14.5	5	1.5	36	0.25
240.5–264.0	Silt	9n	17.3	20.5	14.5	5	1.5	36	0.25
264.0–273.8	Compact silty clay	9n	17.3	20.5	14.5	5	1.5	36	0.25
273.8–286.6	Dusty sand	18n	15.86	19.8	30	1	5	240	0.2
286.6–292.1	Dust	15n	17.97	21.3	24	3	2.4	96	0.25
292.1–313.1	Silt	9n	17.3	20.5	14.5	5	1.5	36	0.25
313.1–319.9	Fine sand	18n	15.86	19.8	30	1	5	240	0.2
319.9–329.1	Sandy clay	9n	17.3	20.5	14.5	5	1.5	36	0.25
329.1–333.0	Sandy dust	15n	17.97	21.3	24	3	2.4	96	0.25
333.0–350.0	Silt	9n	17.3	20.5	14.5	5	1.5	36	0.25

Explanations:
ρ – density
ρ_{sat} – density saturated
ϕ – friction angle of soil
c' – cohesion
y – dilatancy angle
E – Young's module
ν – Poisson's ratio

4. Hydrogeological conditions

The "Żelazny Most" MWDF is located in the area of Uniform Groundwater Body (JCWPd) No. 78 in which one or two aquifers exist in the Quaternary beds. There are 1 to 4 Miocene levels in Neogene sandy formations. The fractured-zone waters in the Triassic formations are highly mineralized. The area of the Uniform Groundwater Body JCWPd includes the Oder River drainage basin, and within its boundaries there is a Major Groundwater Reservoir (GZWP) 314 – Oder River Valley (Głogów). This reservoir is present in permeable sand and gravel formations filling erosion depressions of a Neogene series [3].

Quaternary aquifer formations in the area of the "Żelazny Most" MWDF occur in the form of extensive layers of sandy and sandy-gravel deposits, directly underlying the body of the dams and beach tailings, or occurring at greater depths under glacial till or Pliocene clays. The total thickness of Quaternary formations in the area of the eastern and northern dams is small, and the aquifers are built up by sand and gravel layers with thicknesses of 5 to 40 m. The filtration coefficients of these formations range from 2.7 to 79.6 m/day, averaging 24.1 m/day. The water table in the near-surface layers of the Quaternary level has a free character in the foreground of the dams and a tense character under the filling sediments of the "Żelazny Most" MWDF.

Three levels are distinguished within the Paleogene-Neogene floor: supracoal, intercoal and subcoal.

In the immediate subsoil of the MWDF, there is a level of supercoal, composed of fine and medium sands in the form of lens. In natural conditions, this level, like its deeper Tertiary counterparts, is characterized by subartesian pressure, lower than the placement of the Quaternary water level.

The groundwater of the Cenozoic floor is strongly influenced by the post-flotation water accumulated in the sediments of the "Żelazny Most" MWDF reservoir. The depth of water in these sediments depends on the water level in the sedimentation pond and the distance from the water reservoir. The occurrence of suspended waters stabilizing at different ordinates is a common phenomenon.

Water penetration from the settling pond takes place continuously and is dependent on the water level in the landfill and the extent of the boundary line. Infiltration of water from the tailings pond into the ground caused hydrodynamic and hydrochemical changes in the groundwater around the landfill. The hydrated layers of waste in the sand and gravel bedding zone are locally in contact with waters of the Quaternary horizon [3, 4].

5. Scope of planned drilling operations

It is planned to drill 4 dewatering wells of 250 and 350 m b.s.l. as part of the designed drilling program. All the wells will be drilled in the slopes of the "Żelazny Most" MWDF in adapted cavities. All the boreholes will be drilled with a drill of 0.56 m in diameter, after which a surface casing ϕ 0.508 m will be tripped down. The borehole will then be drilled to the planned depth with a drill ϕ 0.444 m and a 0.280 m diameter filtration column will be installed. An appropriately sized gravel pack will be introduced into the annular space.

6. Methodology for calculating rock mass pressures according to Coulomb–Mohr theory

The basis for determining the strength parameters of the filtration columns in the designed boreholes is the knowledge of components of the primary state of stress in the rock mass and the magnitude of pressure occurring at the interface between the wall of the casing column or the filtration column and the rock environment [1, 2, 6].

Apart from purely technological considerations, the proper operation of the well is determined by the strength of the casing, i.e. the casing column and filtration column tripped into it.

If the compressive strength condition is to be met for the casing or filtration columns, a pressure distribution function around the drilled wellbore should be provided.

6.1. Determining the highest vertical and horizontal pressures in the intact rock mass by the analytical method

In this paper, only the method used to determine the state of stress in a loose medium having internal cohesion will be addressed. The original state of stress in such a medium is determined based on the Coulomb–Mohr method with the following equation [5, 7, 8]:

$$\delta_2 = \frac{1+\sin\phi_i}{1-\sin\phi_i}\,\delta_1 + 2k_i\frac{\cos\phi_i}{1-\sin\phi_i} = \sum_{i=1}^{n} g h_i \rho_i \tag{1}$$

where:

δ_2 – the highest principal stresses acting vertically at the bottom of a given layer,
δ_1 – the lowest principal stresses acting horizontally,
g – acceleration of gravity,
h_i – thickness of i-th layer,
ϕ_i – angle of internal friction of the i-th layer,
ρ_i – density of the i-th rock layer,
k_i – cohesion of the i-th layer.

If veritical stress δ_2 is denoted as p_z, and horizontal stress $\delta_1$is denoted as p_x, then equation (1) will assume the following form:

$$p_z = \frac{1+\sin\phi_i}{1-\sin\phi_i}\,p_x + 2k_i\frac{\cos\phi_i}{1-\sin\phi_i} = \sum_{i=1}^{n} g h_i \rho_i \tag{2}$$

The physicomechanical parameters of rocks appearing in equation (2) were assumed in compliance with materials presented in [4] and given in Table 1.

The horizontal pressure of rocks at a given depth in the top of the i-th layer was determined from the transformed equation (2).

$$p'_x = \left(\sum_{i=1}^{n-1} g h_i \rho_i - 2k_i\frac{\cos\phi_i}{1-\sin\phi_i}\right)\frac{1-\sin\phi_i}{1+\sin\phi_i} \tag{3}$$

whereas the horizontal pressure in the bottom of the i-th layer equals to:

$$p''_x = \left(\sum_{i=1}^{n} g h_i \rho_i - 2k_i\frac{\cos\phi_i}{1-\sin\phi_i}\right)\frac{1-\sin\phi_i}{1+\sin\phi_i} \tag{4}$$

6.2. Determining pressure in the immediate vicinity of a casing pipe

The theoretical principles of calculating pressure in the immediate vicinity of a casing column have been described in detail in [1, 9–11] and literature [12–16].

The values of pressure on the contact of casing and gravel pack contact can be calculated from the below equation [8, 19]:

$$\delta_a = p_x \left(\frac{a}{R} \right)^{C-1} \tag{5}$$

where:

- δ_a – pressure on the contact of gravel pack and a casing pipe,
- p_x – horizontal pressure of rock is in the intact rock mass, described with equations (3) and (4),
- a – outer diameter of a casing pipe,
- R – diameter of the drilled wellbore,

$$C = \frac{1 + \sin\phi_{zw}}{1 - \sin\phi_{zw}}$$

ϕ_{zw} – angle of internal friction of gravel pack after thickening in the wellbore.

Having assumed that the angle of internal friction for gravel $\phi = 36^0$ is $C = (1 + \sin\phi_{zw})/(1 - \sin\phi_{zw}) = 3.852$, then the ultimate form of equation (5) will take the following form:

$$\delta_a = p_x \left(\frac{a}{R} \right)^{C-1} = p_x \left(\frac{a}{R} \right)^{3.852-1} = p_x \left(\frac{a}{R} \right)^{2.852} \tag{6}$$

If the pressure acting on the casing equals to the pressure evoked by the weight of the gravel pack, then the pressure can be determined from the equation:

$$p_x^* = p_z^* \cdot \frac{1 - \sin\phi_{zw}}{1 + \sin\phi_{zw}} = g \cdot \rho \cdot h \cdot \frac{1 - \sin\phi_{zw}}{1 + \sin\phi_{zw}} \tag{7}$$

No cohesion parameter was assumed in above equation.

7. Results of calculations of rock mass pressure distribution around dewatering well No. 1

Calculations of rock mass pressures were performed for the planned dewatering well No. 1 with a depth of 350 m and a filter column of 0.28 m diameter installed within the slope of the "Żelazny Most" MWDF. Figure 2 graphically shows the distributions of vertical and horizontal pressures in the rock mass and gravel pack and in the immediate vicinity of the filtration column in well No. 1.

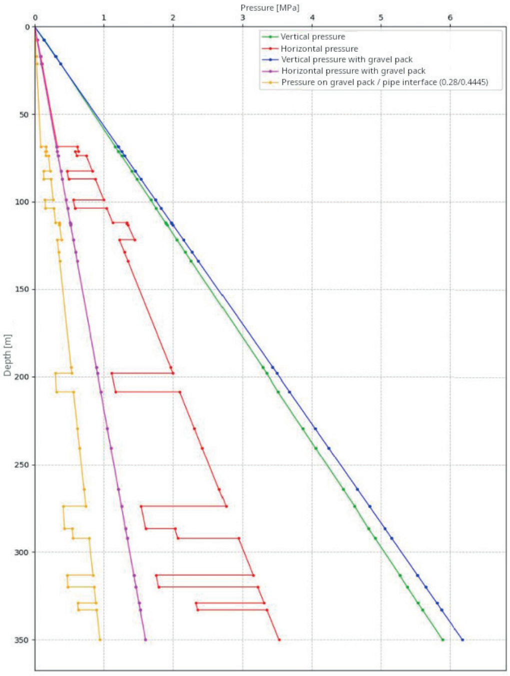

Fig. 2. Collective plots of vertical and horizontal pressures evoked by the rock mass and gravel pack in the dewatering well No. 1

8. Summary of the results of rock mass pressure calculations according to Coulomb–Mohr theory

The analysis of the calculated values of horizontal components shows that the lowest values of stresses acting on the walls of the filtration columns at a given depth are obtained when the pressures are assumed to come from the gravel pack loaded with rock mass. In contrast, the highest pressures result from calculations of the original state of stress in the rock mass.

In line with the widely discussed principles of wellbore design and the calculation of casing strength to the outer crushing pressure [5, 11, 18–22], a less favorable case should be selected from the strength point of view, i.e. the value of horizontal pressure exerted by the rock mass. Accordingly, the dimensions of the casing and filtration pipes, as well as their strength characteristics, should be so designed in dewatering wells that horizontal pressures from the rock mass in the interval of layers with soil properties do not crush the columns.

The analysis of the rock mass pressures calculated by the Coulomb–Mohr method reveals that the maximum values that can lead to the crushing of the filtration columns appear at different depths in individual wells, in their lower intervals.

Taking into account the results of calculations of rock mass pressures in the immediate vicinity of the designed dewatering wells within the “Żelazny Most” MWDF and the experience gained while designing and drilling wells for various purposes, it should be concluded that filter columns with a crushing pressure strength of at least 3.5 MPa should be used for the wells in question.

When adopting such a value for the crushing pressure of the filter pipe columns, account was also taken of the variable geological structure and the very different (but also very low) geomechanical parameters of rocks encountered in the profiles of the planned wells.

Funding: This article was written within the framework of the author’s own research program carried out at the Faculty of Drilling, Oil and Gas of AGH University of Krakow.

Conflicts of Interest: The author of this paper declares no conflicts of interest.

References

[1] Macuda J., Solecki T., Łaciak S.: *Ocena stanu naprężeń w górotworze w aspekcie zgniecenia kolumn rur okładzinowych i filtrowych w otworach 72SD i 73SD*. WWNiG AGH, Kraków 2014 [unpublished].

[2] Macuda J., Kubsik I.: *Projektowanie i wdrożenie nowych efektywnych technologii dla budowy ujęć wód podziemnych*. Grant “EKOŁUPKI”, WWNiG AGH, Kraków 2019.

[3] Michalak J., Świętnicka E., Otrębski A., Borto M.: *Projekt robót geologicznych dla rozpoznania warunków geologiczno-inżynierskich podłoża OUOW Żelazny Most dla potrzeb opracowania dokumentacji geologiczno-inżynierskiej w związku z wykonaniem 7 studni odciążających*. ARCADIS, Wrocław 2022.

[4] Romaniuk D., Tymiński W., Zawadzki Ł.: *Aktualizacja rozpoznania warunków geologiczno-inżynierskich podłoża i osadów OUOW Żelazny Most dla potrzeb wykonania aktualizacji projektów formowania zapór do rzędnej 195.00 m n.p.m.* GEOTEKO SERWIS Sp. z o.o., Warszawa 2022.

[5] Sterrett R.: *Groundwater and Wells*. Litho Tech, Bloomington, MN, New Brighton 2007.

[6] Macuda J.: *Opracowanie techniki i technologii prowadzenia wierceń w warunkach utworów skrasowiałych i silnego krasu na polu Szczerców*. WWNiG AGH, Kraków 2017 [unpublished].

[7] Macuda J.: *Efficiency of drilling large diameter wells with cutter bits on Szczerców opencast*. AGH Drilling, Oil, Gas, 30, 1, 2015.

[8] Macuda J., Wosz R.: *Metodyka obliczania naprężeń w górotworze i w kolumnach stalowych rur okładzinowych dla studni odwadniających i otworów obserwacyjnych w KWB Bełchatów*. WWNiG AGH, Kraków 2004 [unpublished].

[9] Macuda J., Gasiński J., Lesiecki J.: *Wykorzystanie rur z żywic poliestrowych w konstrukcjach studni odwadniających BOT KWB Bełchatów S.A.* Wiertnictwo, Nafta, Gaz, 24, 1, 2007, pp. 317–324.

[10] Macuda J., Solecki T.: *Analiza wytrzymałości konstrukcji otworów odwodnieniowych KWB Bełchatów*. Technika Poszukiwań Geologicznych, Warszawa 1987.

[11] Macuda J., Łaciak S., Solecki T.: *Ekspertyza dotycząca awarii wiertniczej w otworze 23E w KWB Bełchatów*. Zespół Rzeczoznawców SITPNIG, Kraków 1994 [unpublished].

[12] Azar J.J., Samuel G.R.: *Drilling Engineering*. PennWell, Tusa, Oklahoma, 2007.
[13] Borecki M., Chudek M.: *Mechanika górotworu*. Wydawnictwo Śląsk, Katowice 1972.
[14] Driscoll F.G.: *Groundwater and Wells*. Johnson Division St. Paul MN. 1986.
[15] Gonet A., Macuda J., Zawisza L., Duda R., Porwisz J.: *Instrukcja obsługi wierceń hydrogeologicznych*. Wydawnictwa AGH, Kraków 2011.
[16] Kidybiński S.: *Podstawy geotechniki kopalnianej*. Wydawnictwo Śląsk, Katowice 1982.
[17] Gonet A., Macuda J.: *Wiertnictwo hydrogeologiczne*, 3rd ed. Uczelniane Wydawnictwa Naukowo-Dydaktyczne AGH, Kraków 2004.
[18] Harter T.: *Water Well Design and Construction*. University of California 2009.
[19] Macuda J.: *Technologie wiercenia otworów pionowych z powierzchni terenu dla celów pozyskania metanu ze zrobów po eksploatacji węgla kamiennego*. Grant POIR.04.01.01-00-0024/18, WWNiG AGH, Kraków 2023 [unpublished].
[20] Macuda J.: *Analysis of Efficiency of Drilling of Large-diameter Wells with a Profiled Wing Bit*. Archives of Mining Sciences, 57, 2, 2012, pp. 363–373.
[21] Macuda J.: *Reverse Circulation Air Lift Methods for Big Hole Drilling in Brown – Coal Mines*. 9th International Scientific and Technical Conference „New Knowledges in Sphere of Drilling, Production and Gas Storages" Technical University Kosice. Kosice 8–10 October 1996, Slowak Republic 1996.
[22] Macuda J., Łaciak S.: *Opracowanie techniki i technologii wykonywania piezometrów w KWB Bełchatów*. WWNiG AGH, Kraków 2007 [unpublished].

Journal of Geotechnology and Energy | vol. 41 | no. 4 | 2024 | pp. 61–69

https://doi.org/10.7494/jge.2024.41.4.6652

ARTICLE

USING SURFACE GEOPHYSICAL METHODS TO DETECT VOIDS IN THE NEAR-SURFACE ZONE

Michał Maruta

AGH University of Krakow, Faculty of Drilling, Oil and Gas, Poland
ORCID: 0000-0002-1642-8189
e-mail: maruta@agh.edu.pl

Abstract: This study investigates the properties of rock formations using seismic down/up-hole measurements and electrical resistivity methods to identify structural anomalies such as voids. Surveys were conducted in four test wells in southern Poland and the analysis emphasizes the practical applications of mentioned geophysical techniques in subsurface imaging. The seismic method measured wave propagation, while electrical resistivity assessed rock resistance variability, aiding subsurface zoning. The methodology involved designing resistivity maps as depth cuts, based on seismic results. Presented velocity profiles identified weak zones, and was establishing critical geomechanical boundaries in depth, which was a basis for further resistivity geometry projecting. Resistivity measurements were conducted radially around wells, highlighting resistivity anomalies that signify risks related to subsurface void migration and changes in geomechanical properties. The analysis confirmed a general trend of increasing seismic velocity with depth, with significant deviations suggesting differences in rock quality. The resistivity method at the selected depth-cuts, mapped zones with high resistance, which was a direct indicator of the presence of changes in the rock mass. These findings are crucial for planning safe earthworks, soil stabilization, and environmental monitoring, particularly in subsidence-prone areas. Future research may enhance anomaly detection and monitor changes in rock mass properties over time. Combining seismic velocity profiling and resistivity measurements proves effective in identifying subsurface structures, which is vital for risk mitigation in engineering and environmental projects.

Keywords: uphole measurements, resistivity measurements, voids detection, subsurface mapping, shallow surveying

Date of submission:
17.10.2024

Date of acceptance:
25.10.2024

Date of publication:
30.12.2024

https://journals.agh.edu.pl/jge

1. Introduction

Studies employing uphole measurements and electrical resistivity methods aim to determine the physical and mechanical properties of the rock and detect potential structural anomalies, such as voids or changes in geological composition. Velocity profiling enables the measurement of seismic wave propagation speed in rocks, allowing for the assessment of their geomechanical condition, while the electrical resistivity method examines the variability of the rock electrical resistance, which is helpful in identifying different zones in the subsurface. In such studies, understanding the geological setup is crucial for engineering, mining, or environmental protection projects, allowing for risk minimization related to underground voids or terrain deformations [1–5]. The article presents the results of velocity and electrical resistivity measurements analyses, conducted in four test boreholes located in southern Poland. The studies were carried out to examine changes in the mechanical properties of the rock with a focus on detecting potential anomalies, such as voids or structural disturbances.

2. Methodology of conducting velocity profiling and electrical resistivity method

2.1. Description of the down/uphole method

The borehole velocity measurement is one of the most accurate techniques for determining the physical and mechanical properties of rocks. The measurement is based on using an impact source that generates P seismic waves. These waves propagate through the geological layers and are received at various depths by an appropriate system of receivers which are then recorded by a seismograph. The receiving probe typically consists of a receiver made up of three geophone coils oriented in space along the (z, x, y) axes or several to a dozen hydrophones. The probe is placed in the borehole at known depths, while the wave is simultaneously triggered at the surface, where "d" is the distance from the borehole's axis to the source, "r" is the distance between the source and the triplet of sensors, and "z" is the depth (Fig. 1).

The standard data processing methodology consists of the following phases:

- picking the first arrivals of the seismic wave;
- determining the wave arrival times (*t*);
- calculating the velocity values for individual depth intervals [1–5].

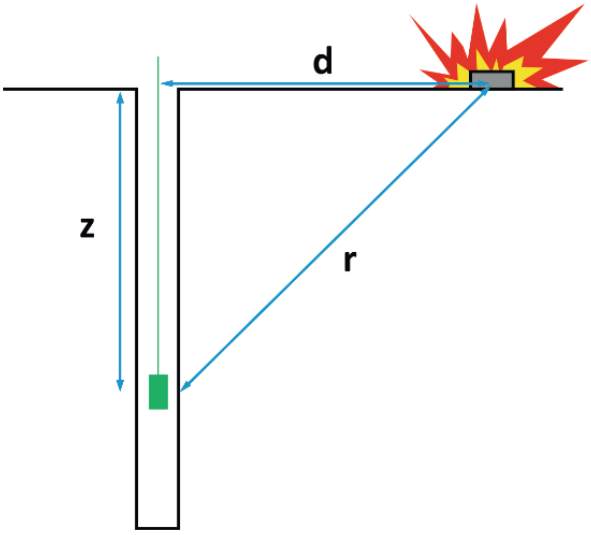

Fig. 1. Schema of down/up-hole measurements

Based on the obtained hodographs, the interval velocity is calculated, defined by the following relation:

$$V\,int = \frac{(Z_2 - Z_1)}{(T_2 - T_1)} \tag{1}$$

where:
Z – depth,
T – wave arrival time [1–5].

During the tests, a point-loading probe was used, with a natural frequency of the built-in sensors equal to 10 Hz. The source of vibrations during the tests was a seismic hammer weighing 5 kg.

2.2. Description of the electrical resistivity method

The electrical resistivity method is a geophysical technique used to investigate the structure of subsurface, utilizing the variation in the electrical properties of rocks (e.g., the ability to conduct electric current and the capacity to polarize the rock environment) [1–3, 6, 7]. Geoelectrical methods are applied to understand the geological structure for engineering, hydrogeological, mining, and environmental protection purposes [2, 6–10].

In the electrical resistivity method, the change in the electric field induced artificially in the ground by applying current electrodes is observed. A key element of this technique is measuring the potential difference across a pair of potential electrodes located within the influence range of the electric field between the current electrodes. Ultimately, this method determines the apparent resistivity values of the rocks within the generated field's reach [1, 8]. Electrical resistivity surveys belong to a subgroup of electrical methods characterized by effectively registering disturbances in the rock mass in areas with significant electrical resistivity contrasts [5]. When applying the electrical resistivity method during field surveys, the apparent resistivity of the rock substrate is measured by deploying four electrodes on the ground's surface, forming a measurement configuration [4, 9]. A known current is generated from a power source connected to two current electrodes (A and B). The potential difference is measured across the other two electrodes, known as measurement or potential electrodes (M and N). The depth range of the electrical resistivity method depends on the distance between the electrodes A and B, as well as the lithology of the area. The choice of the depth range for the setup is determined by the specific, often complex geological structure, which frequently serves as the basis for conducting field tests [3–9]. The investigation of the zone around boreholes above mining excavations was carried out using a modified electrical resistivity sounding method [4, 7, 11]. One of the current electrodes was placed at the bottom of the borehole, while the other was positioned at a distance according to the methodological recommendations for Wenner-type measurement configurations [7–10]. The measurement of the potential difference was conducted using a regular radial measurement setup (with a potential change interval of 3 m). This allowed for determining the distribution of resistivity in the rock mass around the borehole selected for seismically established depth-cut.

2.2. Measurement geometry – resistivity method

Studies were conducted in a radial arrangement with a minimum of 8 profiles, each approximately 18 m long, rotated every 45 degrees relative to the well. In cases where significant changes in resistivity were observed, the profiles were densified. One of the current electrodes was permanently placed in the well, while the other was positioned at an appropriate distance to ensure adequate depth of electrical resistivity investigation – usually maintaining a ratio of 3 times the depth of the resistivity cut. On each of the radial profiles, measurements of the potential change in the electric field were taken at intervals of 3 m. Measurements were carried out on the available measurement surface. The measurement data in the area of well W2 were limited due to the inability to maintain the measurement geometry caused by terrain obstacles.

3. Results

3.1. Results of measurements in well

The interpretation of seismic data involved identifying the first arrivals of longitudinal waves and calculating the interval velocity values for the entire well. The mentioned velocity distributions characterize the rock mass in two ways: by identifying the longitudinal wave velocity and by observing changes in the characteristics of velocity distributions (e.g., decreases). This allowed for the detection of discontinuities and profiling was performed in wells W1, W2, W3 and W4.

The results are presented as velocity distributions within the depth range of the investigated wells. A key feature of the obtained results is the general increase in velocity with depth. A distinguishing feature of the distributions is the variable characteristic of velocity values with depth.

It should be noted that, apart from well W1 (Fig. 2), the velocity values associated with the presence of sandstones in the range of 1 100 m/s to 1 200 m/s. This indicates that the medium is highly fractured. Well W1 represents an exception to this trend, as the rock medium in it has values of approximately 1 400–1 500 m/s, indicating it is fractured, but no displacements occur. Profiling in well W2 (Fig. 3) was concluded at a depth of 26 meters due to the heaving and clogging of the well with sand and water. In well W3 (Fig. 4), part of the recorded data from the near-bottom zone did not contain useful signals, a similar situation was observed in well W4 (Fig. 5).

It is particularly noteworthy that the mentioned distortions in the seismic signal are noticeable above the level of a probable void caused by the disturbance of rocks. This may be related to the so-called migration of the void towards the surface. On each of the profiles, locations marked with red squares indicate values greater than 700 m/s and greater than 1200 m/s. These served to design studies using the electrical resistivity technique. It was determined that the boundary of 700 m/s marks the transition from a highly altered near-surface zone to a naturally formed unconsolidated material. This boundary, on average across the four wells, occurs at about 7 m. The boundary of 1 200 m/s signals the transition to the proper rock medium, occurring on average at 19.5 m for all wells.

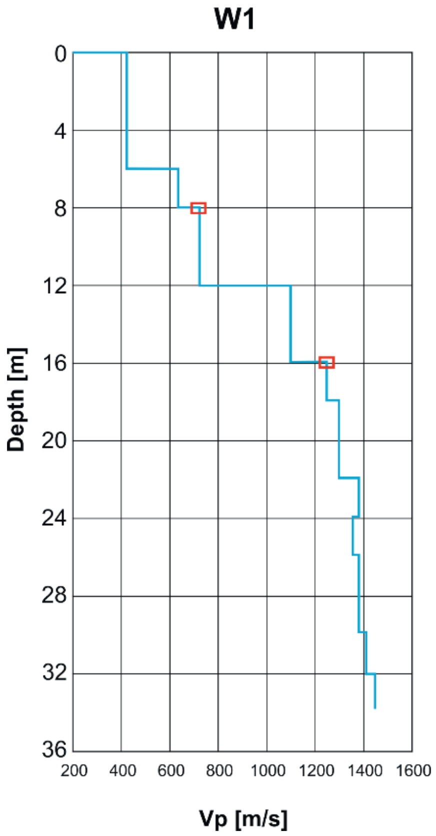

Fig. 2. Results of up/down – hole measurements in Well W1

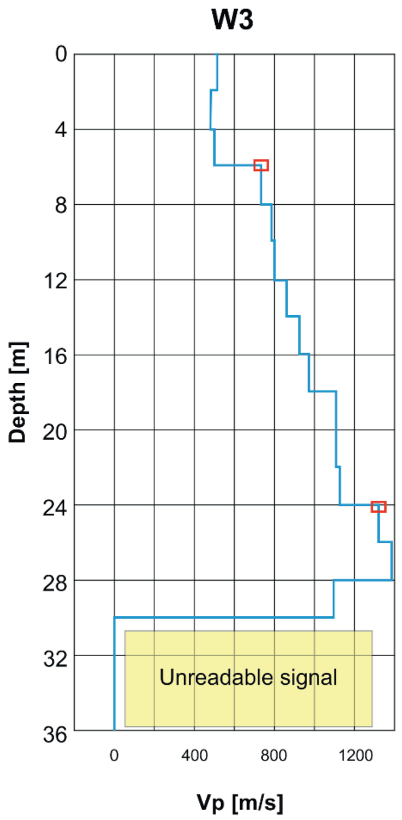

Fig. 4. Results of up/down – hole measurements in Well W3

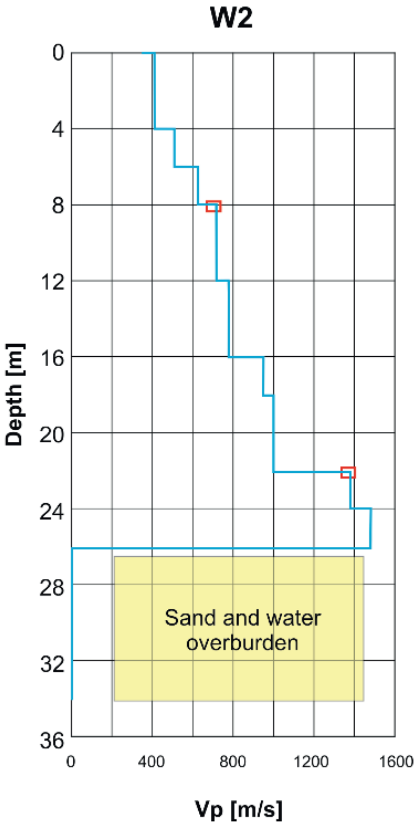

Fig. 3. Results of up/down – hole measurements in Well W2

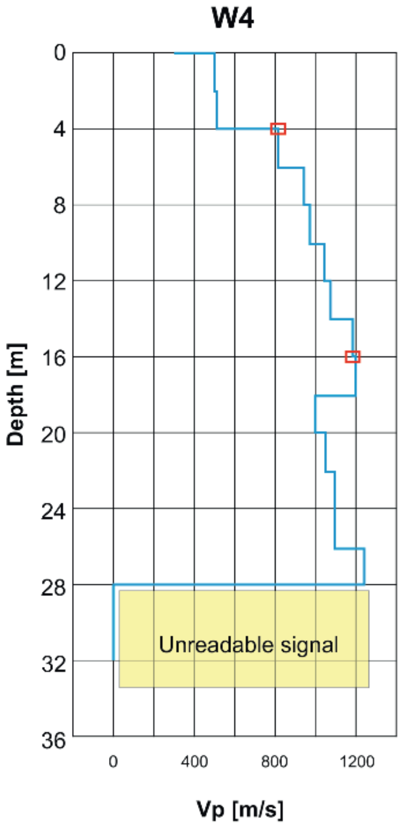

Fig. 5. Results of up/down – hole measurements in Well W4

3.2. Method of investigating the zone around the borehole using the electrical resistivity method

The depths of the electrical resistivity depth-cuts were designed based on the results of seismic velocity profiles, which indicated that the first approximately 6 m of cover consists of weakly bearing material. Therefore, its activation occurs immediately after the continuity of the deeper layers is interrupted. Moreover, this material is poorly consolidated and highly susceptible to changes in the saturation of rainfall. The quantitative interpretation of velocity profiles allowed for the identification of two characteristic geomechanical boundaries within the studied medium. These boundaries are associated with changes in geomechanical parameters, which were investigated through electrical resistivity methods.

Initially, the imaging surface was designed at the level of the bottom of the well, with subsequent depth-cuts assigned to significant changes – velocity boundaries in the wells- assigned by red marks on velocity profiles. The nearest cut to the surface was placed at approximately 10 meters below the surface level (b.s.l.), determined by the increase in velocity values above 700 m/s. The deeper electrical resistivity cut was set at a level of 20 m b.s.l., based on the averaged level where the velocity increased above 1200 m/s.

The work began sequentially in the following wells: W1, W2, W3 and W4. The data obtained at the bottom of the wells (test measurements were conducted for wells W1 and W2) exhibited weak electrical resistivity differentiation, oscillating around <= 20 Ohm·m. The main reason for this phenomenon is likely the presence of mine water with high mineralization, masking the presence of potential voids and causing low variability in the resistivity image. Ultimately, conducting cuts at the bottom of wells W1, W2, and W4 proved to be pointless.

Considering this fact, it became strategic for the investigation of the subsurface to perform measurements at the mentioned levels of 10 and 20 m b.s.l. The level of approximately 20 m b.s.l. corresponds to the upper layer of rocks and appears to be a critical depth due to observed changes in the bedrock. This level is characterized by velocities of 1200 m/s or greater (proper bedrock). On average, this velocity transition occurs at around 19.5 m (depth-cut on 20 m below the surface). The second cut at about 10 m b.s.l. was designed to be representative of the voids breaking through the weakly cohesive material above the bedrock.

This discussed level was also chosen considering the velocity profiles, as the rocks at an average depth of around 7 m b.s.l. exhibits velocities oscillating around 700 m/s or greater, marking the boundary between the heavily altered near-surface zone and more consolidated sediments, so the value of 10 m b.s.l. below the surface was adopted.

In the case of well W3, an attempt was made to conduct an electrical resistivity measurement at a level of 35 m b.s.l. (depth of electrode placement), and test measurements were performed, revealing variability in resistivity measurements. This suggests that the near-bottom zone around this well is not filled with mine water to the extent observed in wells W1, W2 and W4. Considering this result, a full intended measurement geometry was established, resulting in an electrical resistivity map.

Ultimately, for wells W1, W2 and W4 (Figs. 6–9), two depth cuts were obtained, while for well W3, three cuts were made (Figs. 10–12). It should be emphasized that the obtained resistivity maps represent an averaged resistivity value of ±1.5 m concerning the depth position of the cut.

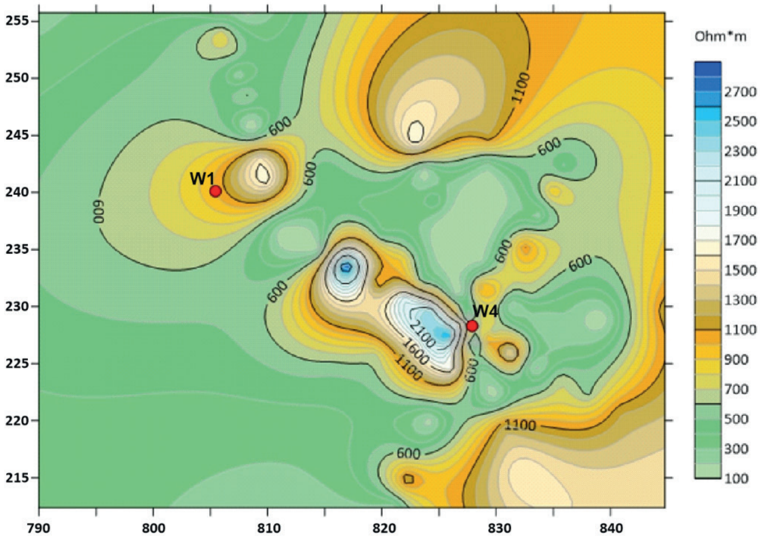

Fig. 6. Resistivity map in the Zone of Wells W1 and W4, Cut – 10 m b.s.l.

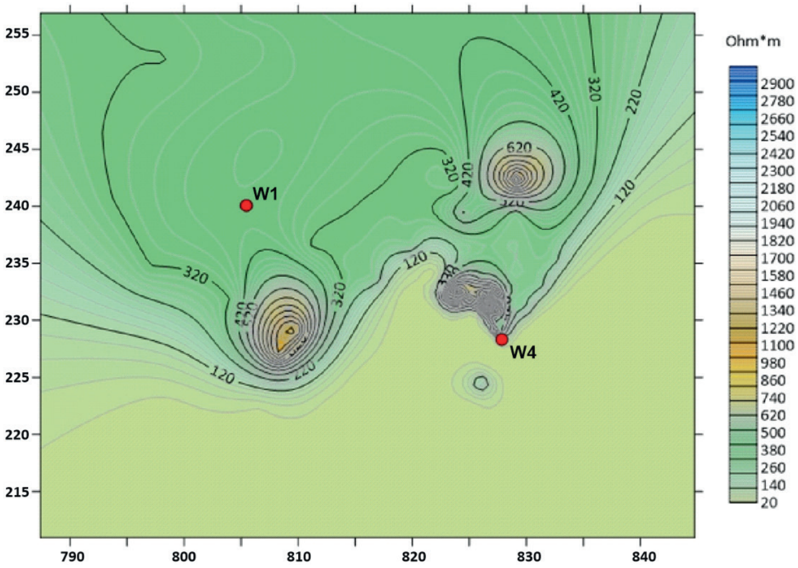

Fig. 7. Resistivity map in the Zone of Wells W1 and W4, depth – 20 m b.s.l.

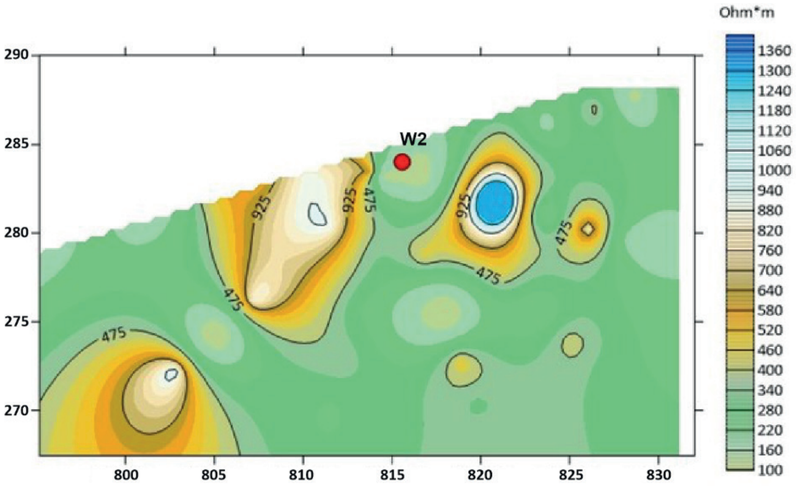

Fig. 8. Resistivity map in the Zone of Well W2, depth – 10 m b.s.l.

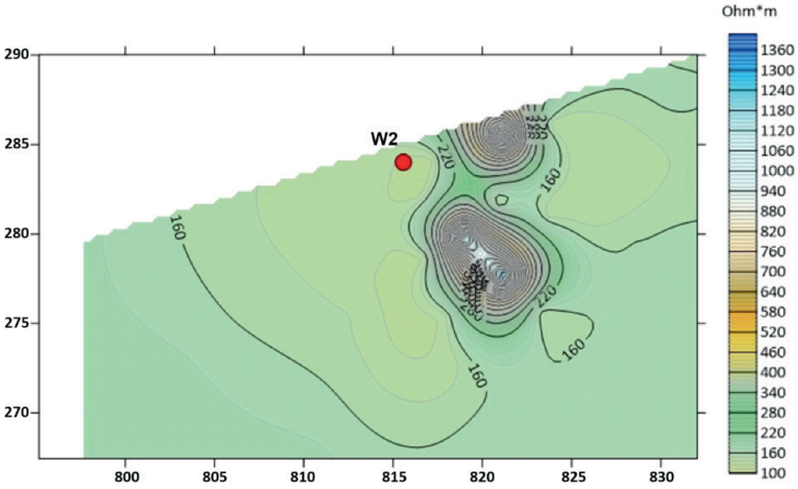

Fig. 9. Resistivity map in the Zone of Well W2, depth – 20 m b.s.l.

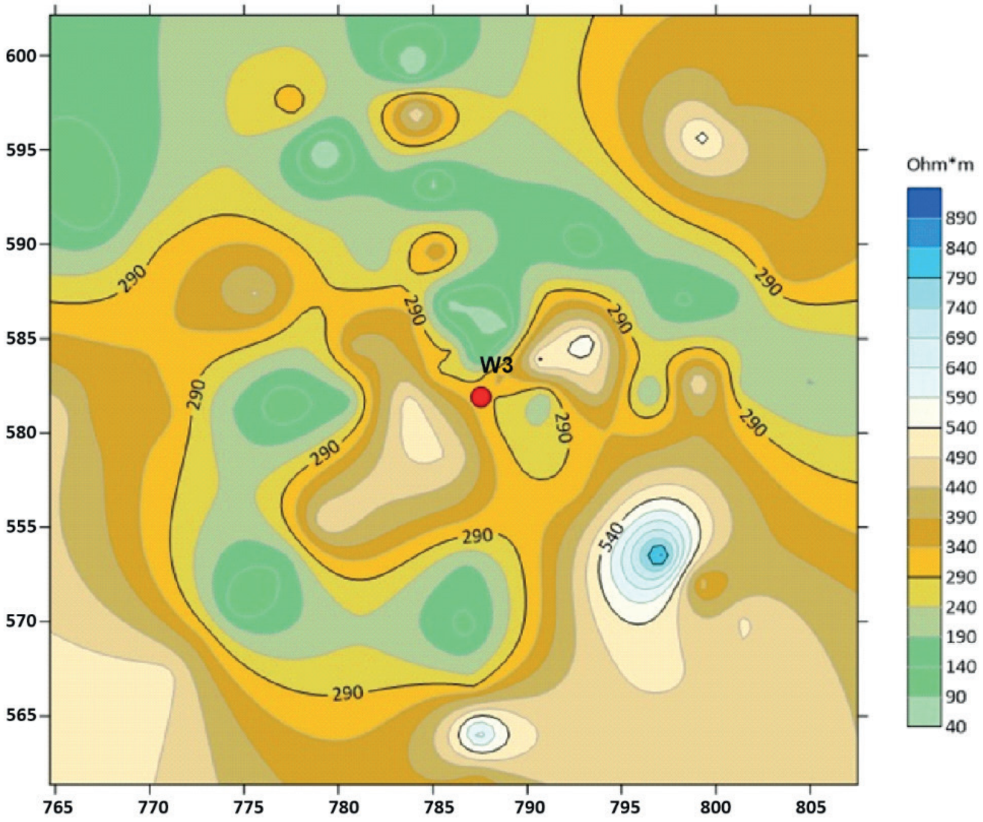

Fig. 10. Resistivity map in the Zone of Well W3, depth – 10 m b.s.l.

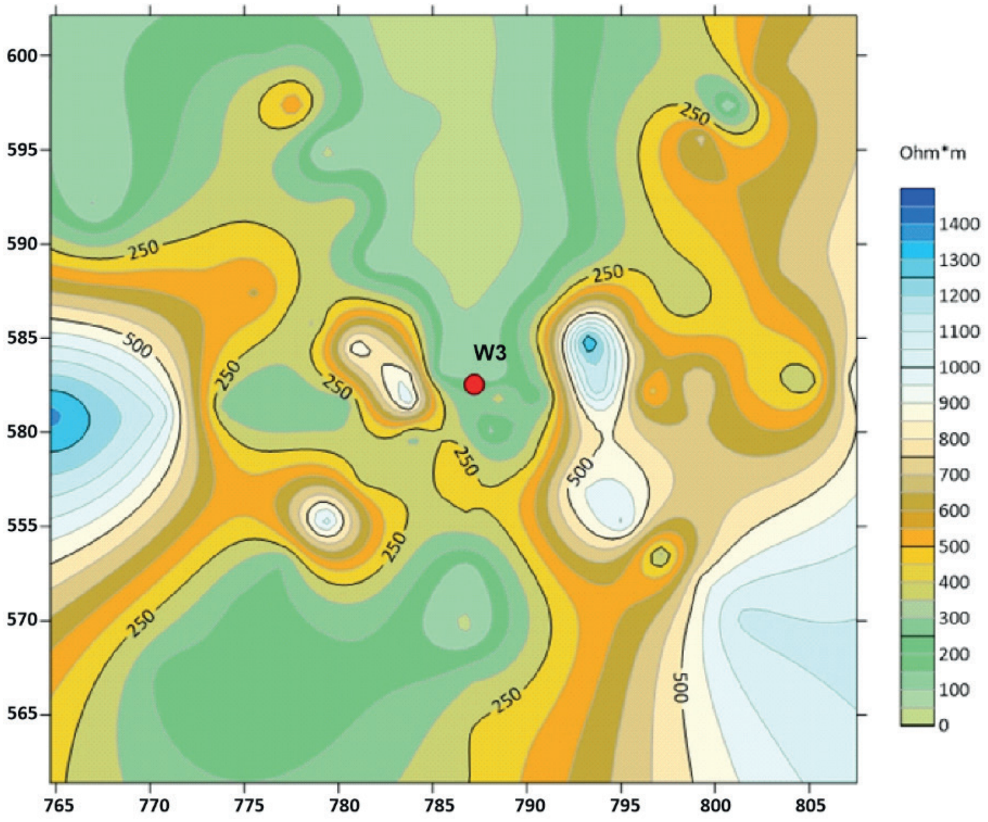

Fig. 11. Resistivity map in the Zone of Well W3, depth – 20 m b.s.l.

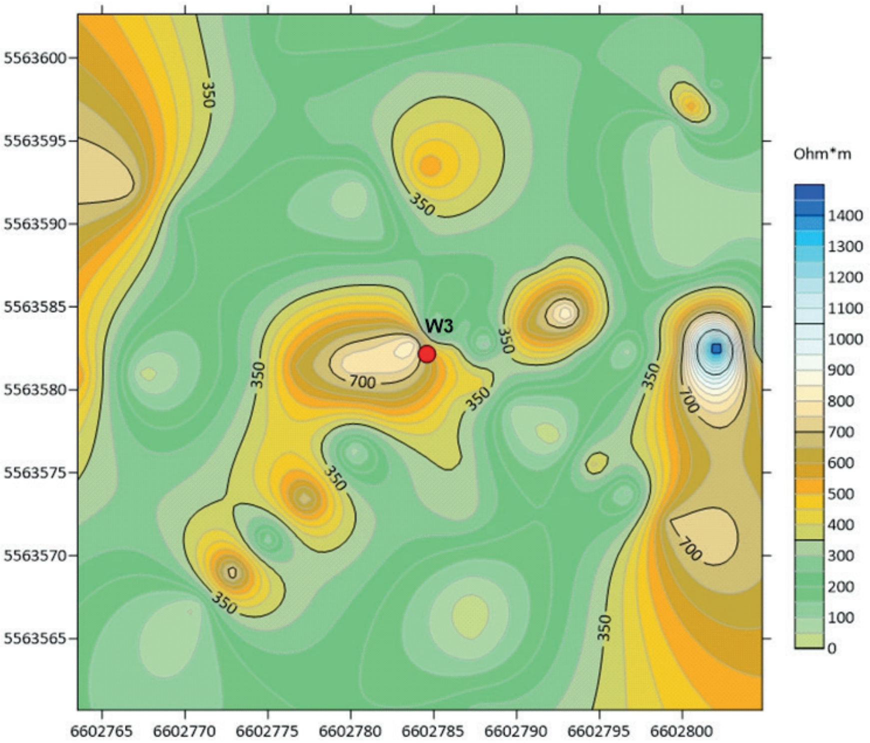

Fig. 12. Resistivity map in the Zone of Well W3, depth – 35 m b.s.l.

4. Discussion

Based on the results of the conducted studies, the investigation at the level of 20 m b.s.l. reveals a rather monotonous distribution of resistivity. High-resistivity anomalies were detected against a background value of around 300 Ohmm. In the case of the map for well W3 (Fig. 12) at the level of 35 m b.s.l., a series of anomalies arranged in a single azimuth is visible. On the same map (Fig. 12), high-resistivity anomalies also appear at the edges of the map's extent. However, the dominant background value is around 200 Ohmm. At the level of 10 m b.s.l. (Figs. 6, 8 and 10), all wells exhibit the most diverse electrical resistivity. Here a series of anomalies occur and the image is strongly differentiated. Anomalies with the highest resistivity values can be considered the most suspicious for the migration of voids toward the surface. It is also possible that the size of the detected anomaly should be taken into account for a more accurate assessment of the risk of layer continuity disruption.

5. Conclusions

This paper presents the results of geophysical studies conducted using seismic and resistivity measurements in several wells. The main objective was to identify structural anomalies such as voids.

The analysis of seismic velocity confirmed a general trend of increasing velocity with depth. However, significant deviations were observed, which may suggest differences in rock quality and the presence of potential anomalies. Resistivity measurements identified anomalous zones, indicating the potential location of voids or changes in the composition of the rock mass.

The results of the studies may have important implications for engineering and environmental projects. Detecting voids and fracture zones is crucial for planning various safe earthworks, soil stabilization, and identifying underground structures. Furthermore, conducting such studies is essential for environmental monitoring, especially in areas prone to land subsidence or water infiltration.

Future studies may focus on the application of advanced geophysical methods to improve the detection of smaller anomalies and to conduct longitudinal studies to monitor changes in the properties of the rock mass over time.

In summary, the combined use of seismic and resistivity measurements can prove effective in identifying critical subsurface structures, serving as a valuable tool for mitigating risks in engineering and environmental projects.

Funding: This research was funded by the AGH University of Krakow subsidy No. 16.16.190.779 (Faculty of Drilling, Oil and Gas. Department of Petroleum Engineering).

Conflicts of Interest: The author of this paper declare no conflicts of interest.

References

[1] Telford W.M., Geldart L.P., Sheriff R.E.: *Applied Geophysics* (2nd ed.). Cambridge University Press, Cambridge, UK 1990. https://doi.org/10.1017/CBO9781139167932.

[2] Dobrin M.B., Savit C.H.: *Introduction to Geophysical Prospecting* (4th ed.). McGraw-Hill, New York 1988.

[3] Kearey P., Brooks M., Hill I.: *An Introduction to Geophysical Exploration* (3rd ed.). Blackwell Publishing, Oxford 2002.

[4] Fajklewicz Z., Wojnar P., Sokolnicki W.: *Elektrooporowe sondowanie gruntu w badaniach geologicznych*, Państwowy Instytut Geologiczny, Warszawa 1972.

[5] Reynolds J.M.: *An Introduction to Applied and Environmental Geophysics* (2nd ed.). John Wiley & Sons, Chichester 2011.

[6] Ward S.H.: *Resistivity and Induced Polarization Methods*. In: *Electromagnetic Methods in Applied Geophysics*, ed. S.H. Ward, vol. 2, 1990, pp. 147–223.

[7] Griffiths D.H., King R.F.: *Applied Geophysics for Geologists and Engineers: The Elements of Geophysical Prospecting*. Pergamon Press, Oxford 1981.

[8] Loke M.H.: *Tutorial: 2-D and 3-D Electrical Imaging Surveys*. Geotomo Software, Penang 2004.

[9] Parasnis D.S.: *Principles of Applied Geophysics* (5th ed.). Chapman & Hall, London 1997.

[10] Kirsch R. (ed.): *Groundwater Geophysics: A Tool for Hydrogeology*. Springer-Verlag, Berlin 2006. https://doi.org/10.1007/3-540-29387-6.

[11] Zohdy A.A.R., Eaton G.P., Mabey D.R.: *Application of Surface Geophysics to Ground-Water Investigations*. U.S. Geological Survey, Washington 1974.

Journal of Geotechnology and Energy | vol. 41 | no. 4 | 2024 | pp. 71–82

https://doi.org/10.7494/jge.2024.41.4.6374

ARTICLE

INVESTIGATION OF SOIL CONDITIONS IN A SELECTED SECTION OF A RAILWAY CUT AS A BASIS FOR DESIGNING GEOENGINEERING WORKS TO IMPROVE THEIR GEOTECHNICAL PARAMETERS

Przemysław Toczek

AGH University of Krakow, Faculty of Drilling, Oil and Gas, Poland
ORCID: 0000-0002-4028-5907
e-mail: toczek@agh.edu.pl

Tomasz Kowalski

AGH University of Krakow, Faculty of Drilling, Oil and Gas, Poland
ORCID: 0000-0002-6767-6342
e-mail: tkowal@agh.edu.pl

Krzysztof Skrzypaszek

AGH University of Krakow, Faculty of Drilling, Oil and Gas, Poland
ORCID: 0000-0003-2358-7361
e-mail: varna@agh.edu.pl

Cezary Cały

PKP PLK S.A, Technology and Laboratory Center in the Silesian Region

Date of submission:
19.06.2024

Date of acceptance:
27.06.2024

Date of publication:
30.12.2024

https://journals.agh.edu.pl/jge

Abstract: One approach to enabling construction, engineering, and mining activities in subsoil with insufficient geo-mechanical properties is to employ innovative methods and technologies. These can effectively modify the physical and mechanical characteristics of the subsoil. The article explores engineering techniques that can enhance the geotechnical properties of soils in locations where they exhibit dysfunctions, such as reduced stability and bearing capacity. Additionally, the paper emphasizes the importance of conducting specific geo-engineering tests to accurately assess the geotechnical conditions. The research directly evaluates the stability of a railway section within the Western Carpathians and presents findings from both field and laboratory tests. Given the instability observed in this section, there is a pressing need for geo-engineering reinforcement measures. These efforts aim to enhance the geotechnical properties and safeguard the railway embankment from potential landslides. Detailed accounts of these remedial works will be the focus of a subsequent study.

Keywords: slopes stabilization methods, geoengineering methods, CPTU probe, rock mass stability analysis, geotechnical tests

1. Introduction

The bearing capacity and stability of subsoil are profoundly influenced by factors such as the degree of consolidation, stress values, and water saturation. To address the challenge of constructing structures in subsoil with subpar geomechanical properties, it's essential to modify the subsoil's physical and mechanical attributes to the desired specifications [1] using innovative techniques.

The design, construction, and subsequent maintenance of engineering structures, transportation infrastructure, hydro-engineering facilities, and the like, invariably present challenges. These challenges necessitate solutions that either enhance the ground's physical and mechanical properties, where necessary, or alter them sufficiently. Such alterations ensure the establishment and sustenance of favorable geo-engineering and geotechnical conditions in susceptible areas.

The issues encountered often stem from intricate geological, hydrogeological, or geomechanical factors, as well as oversights in prior engineering endeavors. A thorough assessment of the geological milieu and the technical constraints specific to the construction site facilitates adjustments to the subsoil's physical and mechanical characteristics beneath engineering structures [1–3].

2. Geoengineering methods

The scope of geoengineering activities feasible in a region is inherently tied to the geological conditions and the physical and mechanical attributes of soils and rocks [1]. These factors significantly influence the design, construction, and utilization of technical infrastructure within the specified area. Figure 1 illustrates the various applications of geoengineering techniques.

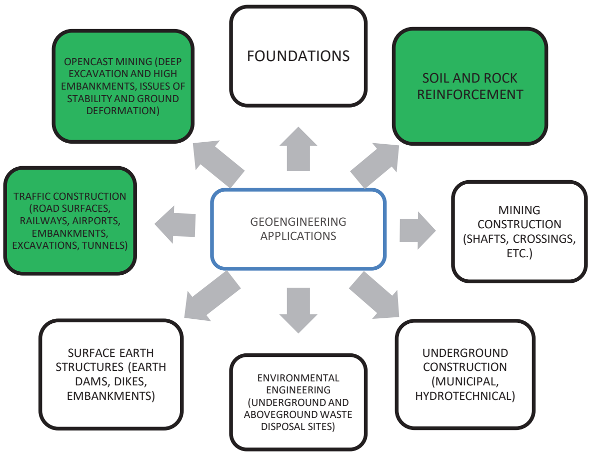

Fig. 1. Own elaboration of geoengineering applications based on [1]

Soil reinforcement plays a crucial role in the construction of various structures, especially when the natural bearing capacity of the soil is insufficient. Approaches to modifying soil properties typically fall into three categories: mechanical, chemical, and physical-chemical methods. Additionally, methods for slope stabilization and protection can be categorized into natural, structural, and synthetic protection, as outlined by Kowacki [4]. Ensuring the stability of slopes, embankments, and excavations remains a paramount concern in the design and execution of civil engineering projects.

Landslides present a significant challenge during the construction, revitalization, and renovation of transport routes. This issue arises not only when attempting to circumvent potential or active landslides but also during the restoration of existing infrastructure facilities [5, 6]. Consequently, accurate forecasting of potential hazards becomes imperative [7]. Addressing the stabilization of escarpments and landslides remains a pressing concern, both in understanding their occurrence and assessing the risks they entail, as well as in advancing scientific methodologies to counteract them [8]. The stabilization of transport-related landslides through structural means has been explored [9], while natural methods and geosynthetics have been discussed [10, 11].

According to the application classification of geoengineering methods, the works were carried out for soil reinforcement to stabilize the landslide along the side of the railway cut surface (Fig. 1 – green color).

Prior to undertaking construction works, it's essential to analyze the existing conditions to determine the most suitable method for modifying the physical and mechanical parameters of the ground. A widely recognized method for such ground investigation is the static CPTU (Cone Penetration Test with Pore Pressure Measurement) sounding [12, 13]. The genesis of this sounding technique can be traced back to the early 1990s [14]. The insights derived from these soundings offer diverse data interpretation avenues, catering to various applications such as landslide investigations [15] or foundational design, including the assessment of pile bearing capacity [13, 16, 17]. Additionally, ground assessment can be enhanced using the SCPTU (static CPTU probe integrated with a seismic module) as discussed by authors [18].

This study offers an analysis conducted using CPTU soundings (Tab. 1) conducted along the railway cut slope (Fig. 2) at designated points Ai, Bi, and Ti. These specific locations were chosen because ground masses exhibited displacement along the slip surface, indicative of the soil medium surpassing its shear strength. The depth and rate of such displacements can vary, resulting in distinct morphological features. The observed landslide formations are attributed to the process of sufosis [19]. This process involves the leaching of soil particles by groundwater in a soil medium characterized by low plasticity, such as silty sands and sandy dust. In the context of this analysis, the formation of these landslides is intrinsically linked to the morphological and geological structures. Their potential occurrence on slopes and inclines is primarily driven by gravitational forces. These formations manifest when the equilibrium between the shear stress components and the soil's resistance is disrupted.

3. Stability analysis as a basis for the design of geoengineering works for slope protection

A comprehensive analysis was conducted to evaluate the stability of the railway cut slopes, particularly in areas where they exhibit instability. To devise an effective solution for ensuring slope stability, it's crucial to pinpoint the factors that contribute to destabilization. A loss of stability typically occurs when shear stresses surpass the shear strength of the soil. Such destabilization can be attributed to various factors, including additional sliding forces, alterations in soil and water conditions, or erosion that diminishes the soil's strength. Often, it's a combination of these factors, making the design of protective measures a multifaceted and intricate process.

In geotechnical endeavors, it is paramount to initially consider the site's morphology and hydrography. A meticulous analysis of the study area lays the groundwork for designing geotechnical interventions, ensuring an accurate assessment of slope stability, embankments, cuts, and other features. Geographically, the area under study is situated in the Western Carpathians. From a geological perspective, it falls within the bounds of the Silesian Plateau, serving as the watershed between the Vistula and Oder river basins. A close examination of the railway line's trajectory on the geological map of Poland, specifically the Cieszyn sheet, reveals that it rests on a bedrock primarily composed of resilient Cretaceous shales interspersed with limestone and thinly-layered marls of the Silesian Mantle. However, certain segments are overlain by Holocene clays, loams, and Pleistocene loess and silts, which offer less-than-ideal support for the railway subgrade's foundation. Despite this fact, an assessment of landslide occurrences sourced from the State Geological Institute's register units (SOPO PIG-PIB 2022) did not indicate any such events in the region under scrutiny. The study commenced with an on-site evaluation, facilitating an in-depth assessment of the geotechnical conditions, encompassing morphology, hydrography, geological structures, and potential site-specific challenges that could influence both design and implementation phases.

In the examined railway cut slopes, a significant issue arises from the presence of a plasticized layer comprised of silty soil. Due to shearing forces, this layer has given rise to a slip plane. The steep gradient of these slopes inherently lacks adequate stabilization, thereby promoting the occurrence of surface soil slides. In alignment with the standards outlined in (PN-EN 1997-1:2008/Ap2, 2010), stability index values were derived from calculated parameters. Notably, these derived parameters were approximately 25% lower than those ascertained through field or laboratory tests, indicating a potential underestimation of the results. The stability analysis was conducted at intervals of 50 m across the evaluated slope section (Fig. 2) in accordance with the following framework:

- Cross-section at km 33+250,
- Cross-section at km 33+300,
- Cross-section at km 33+350,
- Cross-section at km 33+400.

In the article authors were shown cross-section data at km 33+250, km 33+300 and km 33+400 with stability calculations for the slope, both before and after geotechnical works.

In the tables below, the characteristic parameters for mentioned cross-sections are marked (Tabs. 2–4).

Table 1. Depths of CPTU static soundings and boreholes for the case under consideration made from the right – Ai, left – Bi and in the axis of the railway surface Ti of the analyzed slope of the railway cross-section

No.	Measurement point	Probe CPTU [m b.s.l.]	Borehole [m b.s.l.]
1	33+200_T1	4.1	3.5
2	33+200_A	4.1	–
3	33+200_B	6.1	–
4	33+250_T1	4.1	3.5
5	33+250_A	5.2	–
6	33+250_B	7.1	–
7	33+300_T1	4.1	3.5
8	33+300_A	6.6	–
9	33+300_B	6.9	–
10	33+350_T1	4.1	3.5
11	33+350_A	4.8	–
12	33+350_B	6.3	–
13	33+400_T1	4.1	3.5
14	33+400_A	4.1	–
15	33+400_B	4.1	–
16	33+450_T1	3.6	3.5
17	33+450_A	4.1	–
18	33+450_B	4.8	–

During the CPTU examination, various parameters were meticulously recorded at 1 cm depth intervals, including:

- resistance under the probe cone *qc* [MPa]: this parameter was recorded within the range of 0–100 MPa with a resolution of 0.01 MPa,
- friction at the friction sleeve *fs* [kPa]: the values were captured between 0–3000 kPa with a resolution of 0.71 kPa,
- pore pressure at *u*2 [kPa]: this was measured directly behind the cone, beneath the friction sleeve, with values ranging from 0–3000 kPa and a resolution of 0.27 kPa,
- inclination of the cone in both x and y directions [°]: the inclinations were recorded within a ±30° range with a resolution of 0.1°,
- cone penetration velocity *v* [cm/s]: the velocity was gauged with a resolution of 0.08 cm/s.

3.1. Results

The soil type was identified using a Robertson diagram tailored for Polish soils, as specified in (PN-B-04452 2002). To employ this diagram effectively, values for the standardized cone resistance *qt* (accounting for pore pressure *u*2) and the friction coefficient R_f were determined in line with the guidelines (ISO 22476-1 2013). The definitive identification of the soil type is manually executed by the interpreter, who considers data from concurrent investigations, notably geotechnical borings. Parameters reflecting the soil condition were ascertained by following the protocols (PN-B-02480:1998). The compaction degree for non-cohesive soils was deduced using equation:

$$I_D = 0.709 \log q_c - 0.165 \tag{1}$$

The degree of plasticity I_l of cohesive soils (or alternatively the corresponding values of the consistency index I_c), depending on the content of the clay fraction in the layer under consideration *c*:

$$I_l = 0.242 - 0.427 \log q_c, \text{ for } f_i > 30\% \tag{2}$$

$$I_l = 0.518 - 0.653 \log q_c, \text{ for } f_i = 10\text{–}30\% \tag{3}$$

$$I_l = 0.729 - 0.736 \log q_c, \text{ for } f_i < 10\% \tag{4}$$

The assignment of the soils in the investigated soil profile to the appropriate group was made on the basis of a previous interpretation of the soil type and the resulting clay fraction content, according to the classification diagram, the so-called Ferret's triangle (PN-B-02480:1998).

The angle of internal friction φ' of non-cohesive soils was determined based on equation (5) in the standard (DIN 4094:1990-12, 2013), i.e.:

$$\varphi' = 23 + 13.5 \log q_c \tag{5}$$

It is assumed that the above relationship is applicable to non-cohesive soils containing at most a small admixture of fine facies (e.g., silty sands).

For cohesive soils (fine-grained soils) the shear strength under no-drain conditions is determined below:

$$s_u = \frac{q_c - \sigma_{v_0}}{N_k} \tag{6}$$

where are: σ_{v_0} represents the vertical total geostatic stress, N_k is an empirical coefficient, the value of which is contingent upon the soil's plasticity index. This index is estimated based on the recommendation from the Swedish Geotechnical Institute, given by the formula $N_k = 13.4 + 6.65 \times w_l$. Here, w_l denotes the liquid limit value, as determined by the table of properties for typical Polish soils, as referenced in [20].

Edometric moduli of soil compressibility for the study area were determined from the standard PN-EN 1997-1:2008, Eurokod 7.

Following the investigations, horizontal layers were identified. The top 1 m below the ground surface consists of silty clays, which also serve as agricultural topsoil. From there, extending to approximately 3.5 m below the surface, brown and grey silty clays exist in a hard plastic state, frequently interspersed with dust layers. This geotechnical assessment pertains to the evaluation of groundwater conditions along railway line no. 190, specifically from km 33+200 to km 33+500, and from km 34+500 to km 34+650 on the Goleszów-Cieszyn route.

In the investigated subsoil, a stratified structure with a horizontal course can be distinguished. In the floor up to a depth of approx. 0.4–1.0 m, there are brown siltstones, which at the same time form an agriculturally cultivated surface. Below, to a depth of approximately 2.5–3.5 m, there is a layer of brown and grey-brown silty clays and hard-plastic silty clays. The above silty clays often contain interbedding of dust. In the bottom of the silty clay, in the section from km 33+250 to km 33+550 (Figs. 3, 5, 7) there is a layer of silty clay of small thickness of approx. 0.5–1.0 m, with a considerable admixture of fine gravel and sand interbeds in plastic and soft plastic state. Below this, grey silty clays with an admixture of gravel were drilled throughout the section, which are generally in a hard-plastic state, with only plastic and soft-plastic in the ceiling. A high concentration of gravel is noticeable in the roof of the above-mentioned silty clays, which is undoubtedly the result of erosional scour and the formation of a "cobble" layer prior to the development of subsequent sedimentary processes.

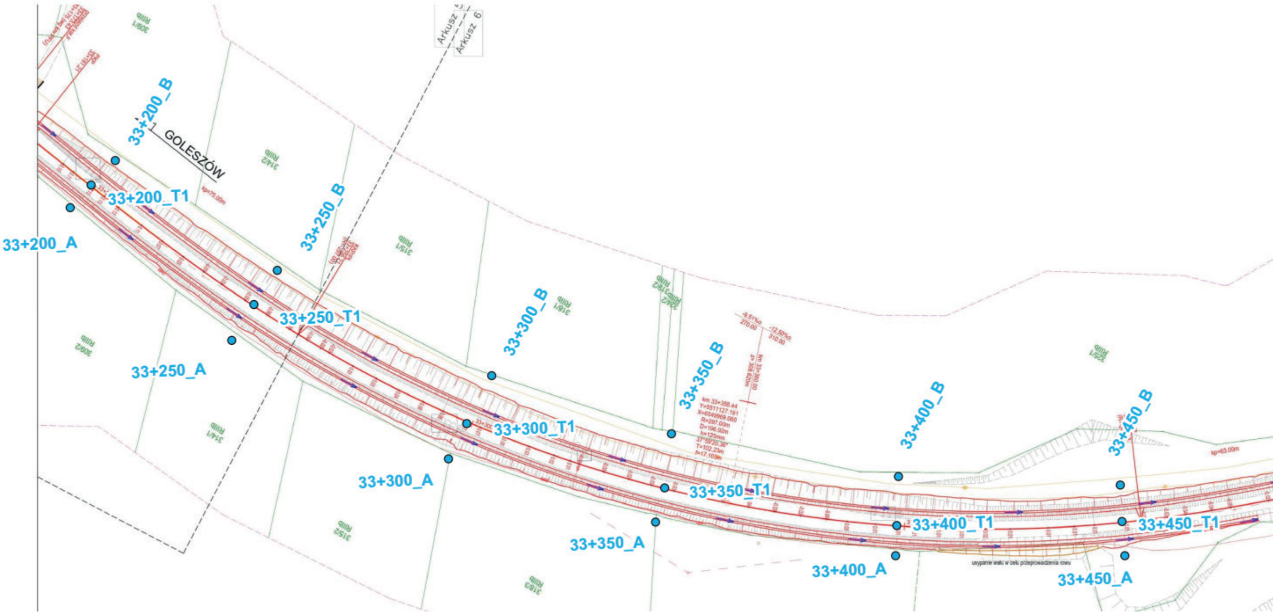

Fig. 2. Characteristic cross-sections across the analyzed slope with an indication of CPTU sounding points

At a depth of approximately 2.5 m from the crown and about 1.5 m from the base of the slope, there is a stratification of degraded, water-softened, soft-plastic dust with a mixture of gravel. This layer is a probable slip plane. The adjacent area to the slope is inclined in its direction. The drainage system directs water to the ditch at the foot of the slope through outlets located at intervals of 30 m at a height of about 1.5 m from the crown of the excavation.

A total of six geotechnical layers were identified within the analyzed cross-section. The layering pattern was established using averaged data from Cone Penetration Test (CPT) with pore pressure measurements (CPTU) and geotechnical boreholes located proximately to the examined cross-section. These geotechnical layers comprised soils of consistent type and origin, displaying analogous values for compaction (in granular soils) or plasticity (in cohesive soils). For these soils, uniform characteristic physical and mechanical parameters were adopted, derived from both CPTU readings and subsequent laboratory tests.

Stability assessments were conducted using design parameters. These parameters were obtained by dividing the characteristic values by a safety factor of 1.25, as raised in standards (PN-EN 1997-1:2008/Ap2:2010, 2010). Mechanical properties (φ', c') of the uppermost slope layers, especially where the outlets of adjacent drainage areas are present, were adjusted using a reduction factor of $\gamma_{red} = 1.4$. Details of the geotechnical layers utilized in the analytical model for selected points are provided in Tables 2–4. It's essential to note that the presented parameters are specific to the examined kilometer of the cross-section and should not be extrapolated universally.

Stability assessments employed the Bishop's method, focusing on a circular slip surface post-optimization, aiming to identify the most plausible path for potential displacements. In the Bishop's method, the interaction forces between the blocks are unknown, and their value is determined by the method of successive trials using general equilibrium equations internal and the stability index is determined from the equilibrium equation of moments of forces relative to the center of the potential slip surface. Figures 4, 6 and 8 illustrates the geological cross-sections with calculations for the designated kilometer at 33+250, 33+300 and 33+400 of the railway line, derived from the comprehensive geotechnical survey.

The presence of these cohesive, plastic soils poses challenges, endangering the stability of slopes and nearby soils along the railway alignment. The inclusion of loose material and sandy layers facilitates water retention across the considered depth, intensifying the plasticization process. Notably, the dust layers are highly vulnerable to plasticization, as even minimal moisture prompts rapid state changes. This vulnerability has led to the formation of a slip edge in this layer (Fig. 5). The geological cross-sections for the designated kilometer at km 33+400 of the railway line, derived from the comprehensive geotechnical survey is shown in Figure 6. Figure 7 presents the cross section with calculations for the mentioned above kilometer point.

Table 2. Characteristic parameters for the selected point 33+250

Geotechnical layer number in 33+400 kilometre range	Type of soil in the layer	Average compaction degree	Degree of plasticity	Reduction coefficient $\varphi'_{red} = \frac{\varphi'}{\gamma_{red}}$ $c'_{red} = \frac{c'}{\gamma_{red}}$	Average parameters		Volume density
	Lithology symbols regarding to PN-EN 1997-1:2008/ Ap2:2010	I_D	I_l	γ_{red}	Angle of internal friction	Cohesion	
					Reduced value	Reduced value	
					φ′	c′	ρ
		[–]	[–]	[–]	[°]	[kPa]	[Mg/m³]
Layer I	$G_{\pi z}$	–	0.28–0.37	1.,4	19	8	21
					14	6	
Layer II	$G_{\pi z}$	–	0.14–0.17	1.4	22	12	20.5
					16	9	
Layer III	$G_{\pi z}$	–	0.23–0.25	1.4	17	12	19.5
					12	9	
Layer IV	$G_{\pi z}$	–	–0.18–0.10	1	32	11	22.0
Layer V	$G_{\pi z}$	0.71–0.81	–	1	41	–	20.0
Layer VI	Degraded drainage ditch interior	–	–0.19–0.08	1	10	10	19.0

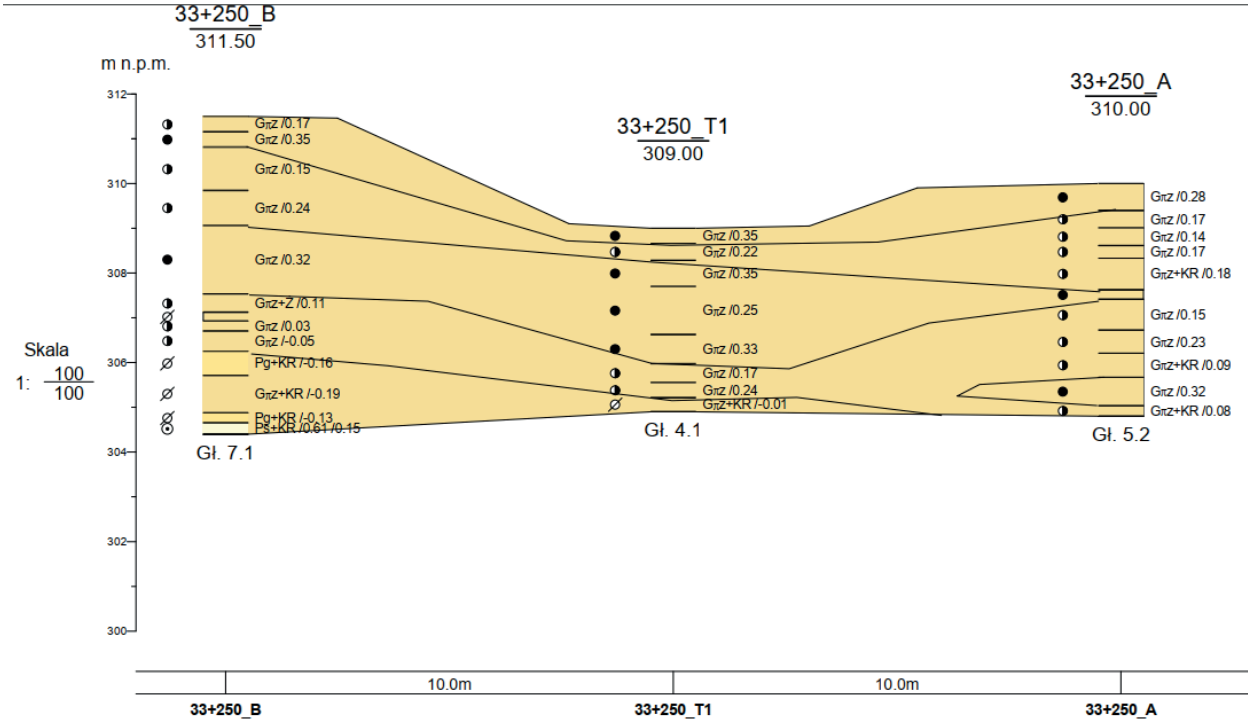

Fig. 3. View of design cross-section with calculations for selected point 33+250 (Geotechnical project BAARS 2020)

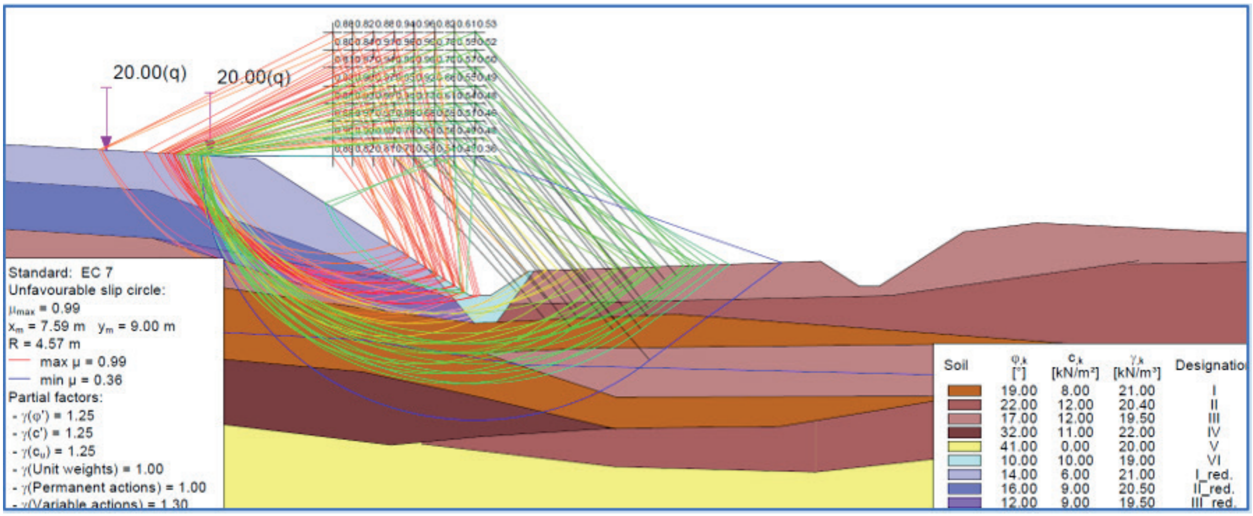

Fig. 4. View of design cross-section with calculations for selected point 33+250 (Geotechnical project BAARS 2020)

Table 3. Characteristic parameters for the selected point 33+300

Geotechnical layer number in 33+400 kilometre range	Type of soil in the layer	Average compaction degree	Degree of plasticity	Reduction coefficient $\varphi'_{red}=\frac{\varphi'}{\gamma_{red}}$ $c'_{red}=\frac{c'}{\gamma_{red}}$	Average parameters		Volume density
	Lithology symbols regarding to PN-EN 1997-1:2008/Ap2:2010	I_D	I_l	γ_{red}	Angle of internal friction	Cohesion	
					Reduced value	Reduced value	
					φ′	c′	ρ
		[–]	[–]	[–]	[°]	[kPa]	[Mg/m³]
Layer I	G_π	–	0.15–0.22	1.4	20	10	21
					14	7	
Layer II	G_π	–	0.27–0.31	1.4	18	21	20.5
					13	15	
Layer III	G_π	–	0.50–0.53	1.4	13	12	19.0
					9	9	
Layer IV	$Pg + KR$	–	–0.02	1	27	7	22.0
Layer V	$Ps + \dot{Z}$	0.90	–	1	40	–	20.0
Layer VI	Degraded drainage ditch interior	–	>0.50	1	10	10	19.0

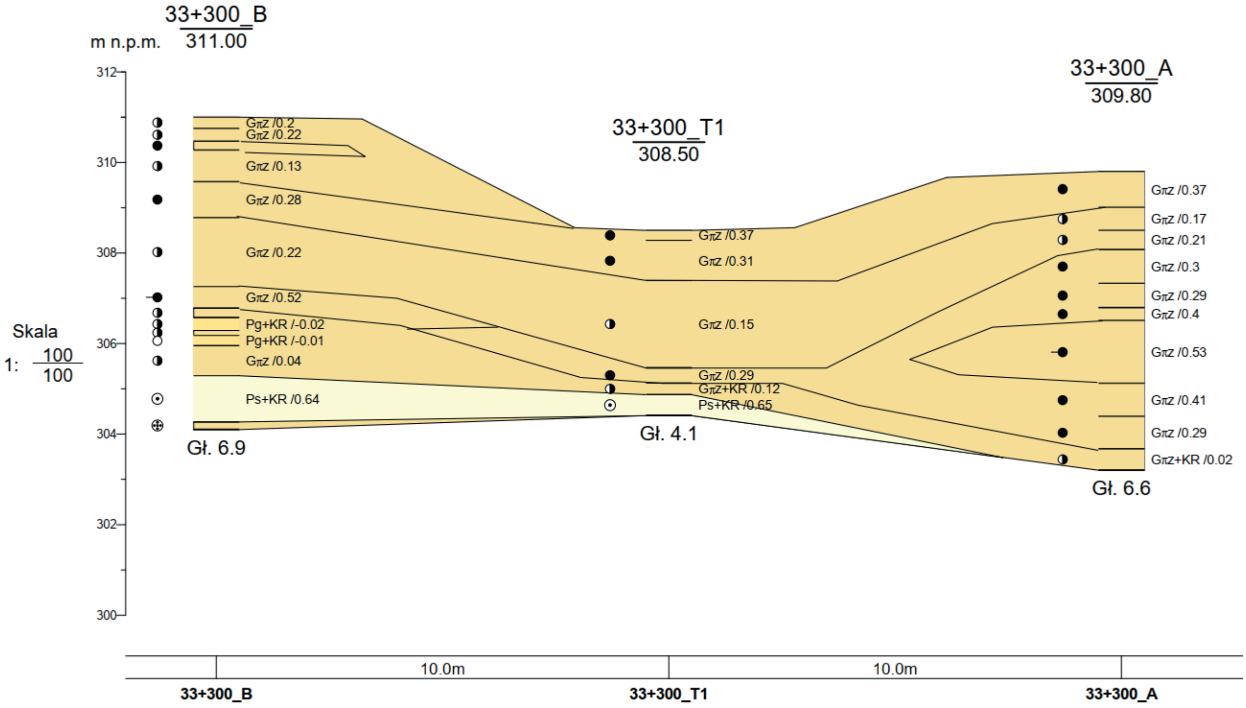

Fig. 5. View of design cross-section with calculations for selected point 33+300 (Geotechnical project BAARS 2020)

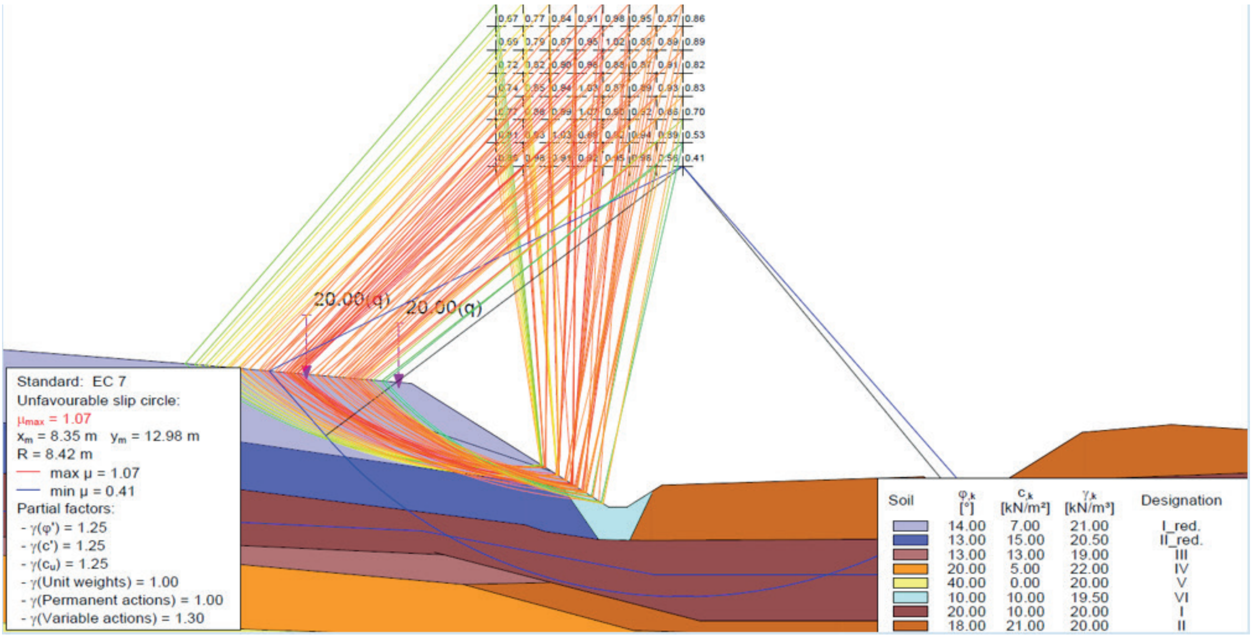

Fig. 6. View of design cross-section with calculations for selected point 33+300 (Geotechnical project BAARS, 2020)

Table 4. Characteristic parameters for the selected point 33+400

Geotechnical layer number in 33+400 kilometre range	Type of soil in the layer	Average compaction degree	Degree of plasticity	Reduction coefficient $\varphi'_{red} = \frac{\varphi'}{\gamma_{red}}$ $c'_{red} = \frac{c'}{\gamma_{red}}$	Average parameters		Volume density
	Lithology symbols regarding to PN-EN 1997-1:2008/ Ap2:2010	ID	Il	γ_{red}	Angle of internal friction	Cohesion	
					Reduced value	Reduced value	
					φ'	c'	ρ
		[–]	[–]	[–]	[°]	[kPa]	[Mg/m³]
Layer I	G_{π}	–	0.27	1.4	21	7	20.5
					15	5	
Layer II	$G_{\pi z}/I$	–	0.14	1.4	14	21	21
					10	15	
Layer III	G_{π}	–	0.3–0.37	1.4	14	14	19.5
					10	10	
Layer IV	$G_{\pi z} + KR$	–	0.02–0.11	1	27	12	22.0
Layer V	*KR/KRg*	0.71	–	1	40	–	20.0
Layer VI	Degraded drainage ditch interior	–	>0.50	1	10	10	19.0

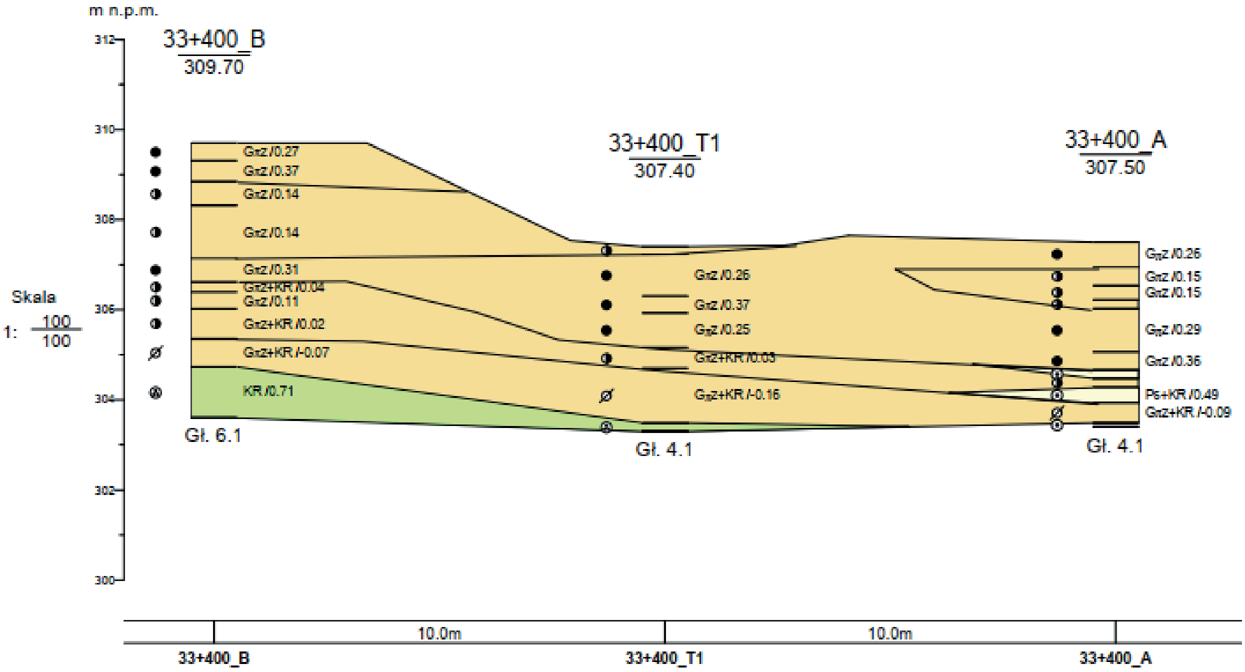

Fig. 7. Geological cross-section for selected point 33+400 (Geological project BAARS, 2020)

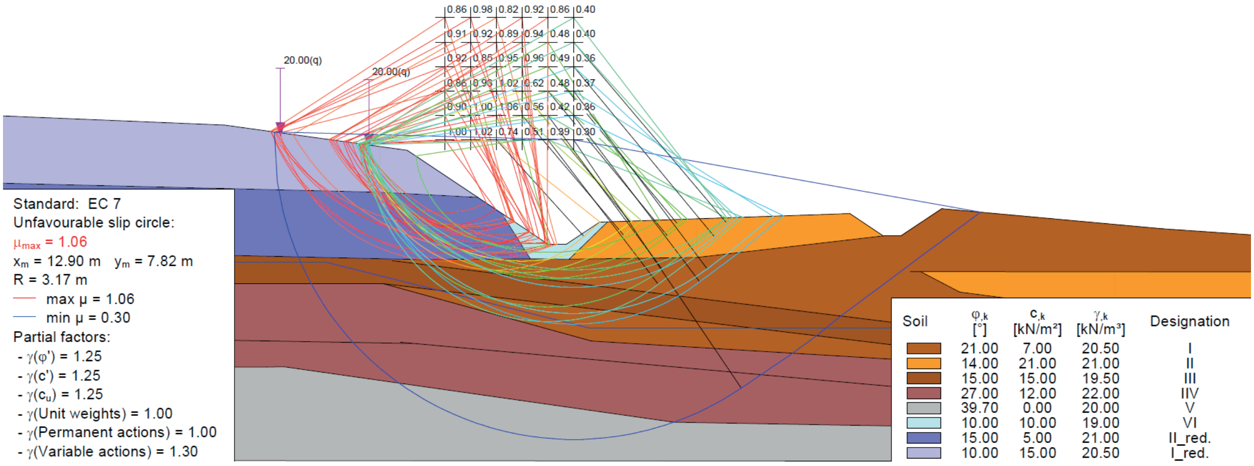

Soil	$\varphi_{,k}$ [°]	$c_{,k}$ [kN/m²]	$\gamma_{,k}$ [kN/m³]	Designation
▨	21.00	7.00	20.50	I
▨	14.00	21.00	21.00	II
▨	15.00	15.00	19.50	III
▨	27.00	12.00	22.00	IIV
▨	39.70	0.00	20.00	V
▨	10.00	10.00	19.00	VI
▨	15.00	5.00	21.00	II_red.
▨	10.00	15.00	20.50	I_red.

Fig. 8. View of design cross-section with calculations for selected point 33+400 (Geotechnical project BAARS, 2020)

The stability analysis conducted for the railway cut slope at kilometres marker 33+250, 33+300 and 33+400 revealed instability, as indicated by a stability coefficient on the properly Figures 4, 6 and 8.

The stability analysis conducted for the railway cut slope at kilometer marker 33+400 revealed instability, as indicated by a stability coefficient of $F_s = 0.94$. Given the characteristics and results of the stability assessment for the underlying subsoil within this section, it is imperative to undertake design interventions to stabilize the slope at this specific segment of the railway cut.

4. Conclusions

The geotechnical assessment conducted to evaluate the ground conditions of the considered railway line segment highlights significant slope instability. Field and laboratory tests indicate that the instability of the railway cut slope is multifaceted. It arises from a horizontally layered arrangement of strata aligned parallel to the railway cut's direction. This layering encompasses variations in geotechnical parameters, with hard clay layers interspersed with softer, more plasticized zones. The natural subsoil, characterized by its heterogeneity, is highly susceptible to plasticization.

A comprehensive understanding of the soil and hydrological conditions within the examined slope is crucial for designing effective interventions. The primary objective during engineering interventions is to prevent water infiltration into vulnerable layers, particularly at the slip edges and areas of dysfunction.

Within the railway cut's slope, a notable concern is the presence of a plasticized layer of silty soil. This layer has developed a slip plane due to shearing forces. The pronounced slope gradient exacerbates the instability, making the area prone to surface landslides. To mitigate these risks and safeguard against the future threats outlined in the study, it is imperative to develop geotechnical protective measures. These measures should address the potential for mass soil movements along the slip plane within the softer, plasticized dust layers. Various methodologies for such protection will be elaborated upon, drawing parallels to similar challenges encountered in railway cut scenarios.

After all the calculations reinforcement solution were made and it included:

- installing a palisade made of interconnected steel sheet piles anchored with ground spikes to cut through the slip plane,
- reinforcing the slope surface with a concrete anchor and an erosion-resistant geotextile anchored in place,
- strengthening the bottom of the drainage ditch with openwork concrete slabs, filled with dry concrete to prevent soil erosion,
- stabilizing the excavation bottom forming the subgrade with a cementitious binder to prevent the infiltration of rainwater,
- topping the palisade with a concrete anchor and installing linear French drainage behind it,
- directing the drainage to a well at the end of the slope and intermittently to the drainage ditch under the anchor,
- maintaining drainage in the gaps between the sheet piles using a concrete board,
- extending drainage outlets from adjacent agricultural lands at a height of approximately 1.5 m below the slope crown, directing the discharged water to an open ditch at the base of the railway track,
- reinforcing the slope in areas where water is drained from the outlets by installing openwork concrete slabs with voids filled with dry concrete.

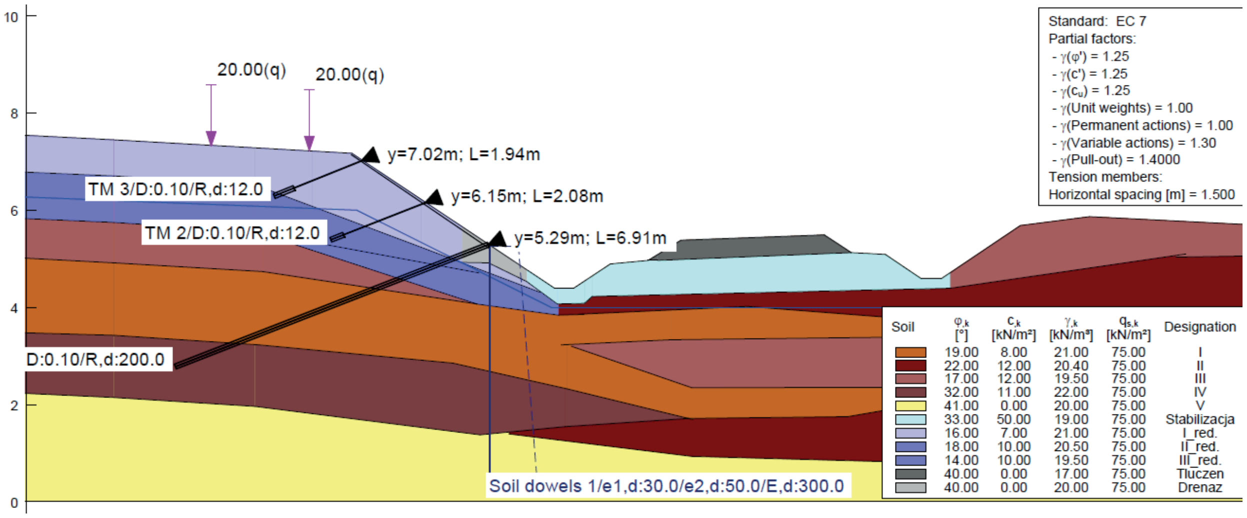

Fig. 9. View of design cross-section with calculations for selected point 33+400 (Geotechnical project BAARS, 2020)

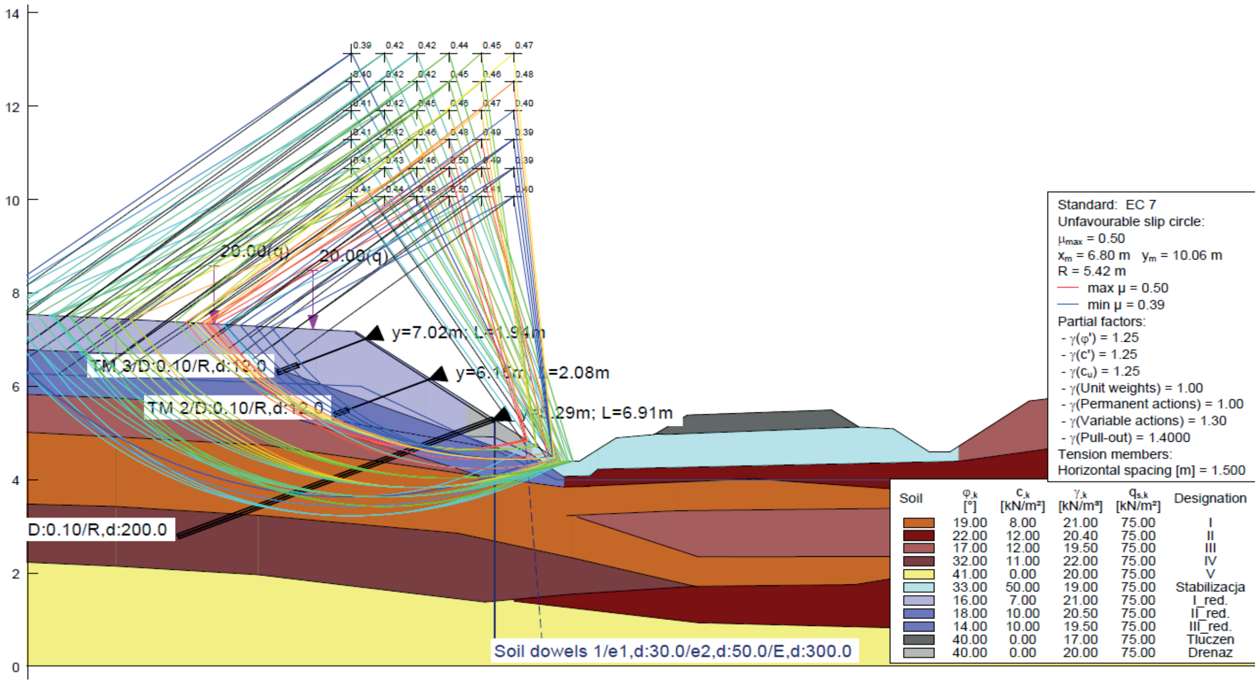

Fig. 10. View of design cross-section with calculations for selected point 33+400 (Geotechnical project BAARS, 2020)

The geotechnical works carried out have improved the stability of slopes within the analyzed section of the railway cutting. In Figures 9 and 10 the cross-section at kilometer 33+250 is shown, along with the applied ground reinforcement and the view of stability calculation results after implementing the proposed solution. The implemented solution has thus achieved a soil stability coefficient above *Fs* = 2.0 for the section at kilometer 33+250, indicating well-executed geotechnical works and slope reinforcement within the analyzed section of the railway cutting.

Author contributions: Conceptualization PT, TK, KS, formal analysis, methodology, writing – review and editing, writing – original draft preparation, and investigation, PT, TK and CC; supervision KS, validation, project administration, PT. All of the authors have read and agreed to the published version of the manuscript

Funding: The project was supported by the AGH University of Krakow, subsidy 16.16.190.779.

Conflicts of Interest: The authors of this paper declare no conflicts of interest.

References

[1] Gonet A., Stryczek S.: *Podstawy geoinżynierii*. Wydawnictwa AGH, Kraków 2020.

[2] Pisarczyk S.: *Geoinżynieria. Metody modyfikacji podłoża gruntowego*. Oficyna Wydawnicza Politechniki Warszawskiej, Warszawa 2005.

[3] Stryczek S.: *Metody geoinżynieryjne modyfikujące właściwości fizyczno-mechaniczne ośrodka gruntowego oraz masywu skalnego*. NTTB Nowoczesne Techniki i Technologie Bezwykopowe, no. 4, Kraków 1999.

[4] Kowacki M.: *Metody stabilizacji i zabezpieczenia terenów osuwiskowych*. Nowoczesne Budownictwo Inżynieryjne, January–February, 2015, pp. 42–47.

[5] Głażewski M., Nowocień E., Piechowicz K.: *Roboty ziemne i rekultywacyjne w budownictwie komunikacyjnym*. Wydawnictwa Komunikacji i Łączności WKŁ, Warszawa 2010.

[6] Kowacki M.: *Stabilizacja skarp i osuwisk*. Nowoczesne Budownictwo Inżynieryjne, May–June, 2019, pp. 88–94.

[7] Wysokiński L.: *Metody prognozowania i zabezpieczania osuwisk (The Methods of Landslides Prediction and Their Protection)*. XXV Konferencja Naukowo-Techniczna „Awarie Budowlane", Międzyzdroje, 24–27.05.2011, pp. 291–320.

[8] Maca N.: *Praktyczne zasady doboru metod stabilizacji osuwisk*. Nowoczesne Budownictwo Inżynieryjne, July–August, 2020, pp. 64–67.

[9] Furtak K., Sala A.: *Stabilizacje osuwisk komunikacyjnych metodami konstrukcyjnymi*. GMDT Geoinżynieria Drogi Mosty Tunele, 3, 2005, pp. 12–22.

[10] Łęcki P., Różański M.: *Wzmacnianie podłoża gruntowego budowli drogowych*. Nowoczesne Budownictwo Inżynieryjne, March–April, 2015, pp. 46–54.

[11] Bzówka J.: *Wybrane techniki wzmacniania słabego podłoża gruntowego w budownictwie komunikacyjnym*. Inżynieria Morska i Geotechnika, 3, 2015, pp. 416–423.

[12] Bagińska I.: *Analiza oceny rodzaju gruntu ustalonego na podstawie badań CPTU (An analysis of the assessment of the type of soil based on the CPTU study)*. Geoinżynieria: Drogi, Mosty, Tunele, 37, 2, 2012, pp. 38–45.

[13] Czado B., Pietras J.S.: *Comparison of the cone penetration resistance obtained in static and dynamic field tests*. AGH Journal of Mining and Geoengineering, 36, 1, 2012, pp. 97–105.

[14] *Engineering Geology Field Manual: Volume II, Chapter 22*, U.S. Department of the Interior Bureau of Reclamation, 2001.

[15] Bednarczyk Z.: *Landslide Investigations by Static Sounding with Pore Pressure Measurements (CPTU), Ground Penetration Radar Techniques (GPR) and Other Chosen Methods*. Conference "Risks Caused by the Geodynamic Phenomena in Europe", Polish Geological Institute Special Papers, 15, 2004, pp. 19–28.

[16] Bagińska I., Sacha M.: *Przygotowanie wyników sondowania statycznego CPTU a proces projektowania nośności pala wciskanego (Preparation of the results of static CPTU probing and the process of designing the load-bearing properties of driven piles)*. GDMT Geoinżynieria Drogi Mosty Tunele, 56, 3, 2016, pp. 14–18.

[17] Eslami A., Moshfeghi S., Mola Abasi H., Eslami M.: *Piezocone and Cone Penetration Test (CPT and CPT), Applications in Foundation Engineering*. Elsevier, Butterworth-Heinemann, 2019.

[18] Jędrysiak N., Bagińska I.: *Rozpoznanie podłoża gruntowego sondą SPCTU (The identification of subsoil with an SCPTU probe)*. Górnictwo i Geoinżynieria, 34, 2, 2010, pp. 341–349.

[19] Stryczek S., Gonet A., Wiśniowski R.: *Geoinżynieryjne metody stabilizacji skarp i zboczy*. Nowoczesne Budownictwo Inżynieryjne, 6, 2008, pp. 78–81.

[20] Wiłun Z.: *Zarys geotechniki*. Wydawnictwa Komunikacji i Łączności WKŁ, Warszawa 2013.

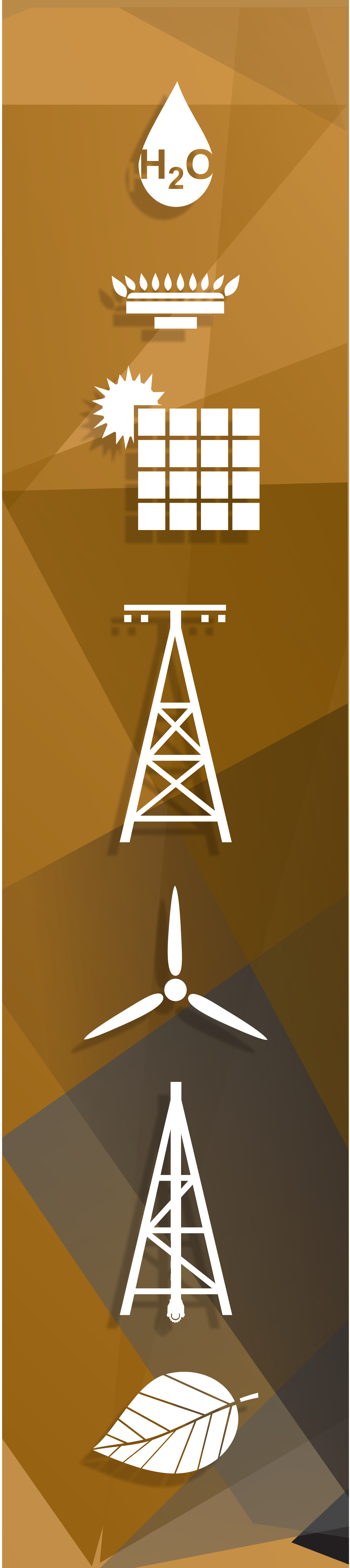
H2O